Role of a bacterial dynamin-like protein DynA in resistance to environmental stress response

by Lijun Guo

Dissertation

Zur Erlangung des Doktorgrades der Naturwissenschaften

(Dr. rer. nat.)

an der Fakultät für Biologie der

Ludwig-Maximilians Universität München

Eidesstattliche Erklärung

Hiermit versichere ich an Eides statt, dass ich die vorliegende Arbeit selbstständig verfasst habe, keine als die angegebenen Quellen und Hilfsmittel benutzt wurden und alle Zitate kenntlich gemacht sind. Des Weiteren versichere ich, nicht anderweitig ohne Erfolg versucht zu haben, eine Dissertation einzureichen oder mich einer Doktorprüfung zu unterziehen. Die vorliegende Dissertation liegt außerdem keiner anderen Prüfungskommission vor.

I hereby confirm that I have written the accompanying thesis by myself, without contributions from any sources other than those cited in the text. This also applies to all graphics, drawings, and images included in this thesis. Moreover, I declare that I have not submitted or defended a dissertation previously without success. This thesis has not been presented to any other examining board.

Lijun Guo

Martinsried, April 05, 2021

Gutachter:

1. Prof. Dr. Marc Bramkamp
2. Prof. Dr. Jörg Nickelsen

Datum der Abgabe: November 30, 2020

Datum der Prüfung: March 04, 2021

Contents

Abstract 4
Zusammenfassung 5
Introduction 7
1 The Dynamin superfamily 7
1.1 Classical dynamins 9
1.2 Dynamin-like proteins in eukaryotes 11
1.3 Bacterial dynamin-like proteins 14
1.4 Bacterial dynamin-like protein DynA 16
2 Membrane fusion process 17
3 Lytic phage Φ29 and prophage SPβ 18
4 Bacteriophage resistance mechanisms 22
4.1 Adsorption inhibition 22
4.2 Injection blocking 23
4.3 Degrading phage nucleic acids 24
4.4 Abortive infection systems 25
4.5 Assembly interference 26
Aims 27
Materials and Methods 29
1 Materials 29
2 Chemicals, enzymes and expendables 29
3 Media and buffers 29
4 Antibiotics 30
5 Oligonucleotides 30
6 Plasmids 32
7 *E. coli* strains 33
8 *B. subtilis* strains and bacteriophage 34
9 Cultivation of bacteria and bacteriophage 35
9.1 Storage and growth conditions 35
9.2 Transformation of *E. coli* 36
9.3 Transformation of *B. subtilis* 36
10 Bacteriophage techniques 36
10.1 Quantitative plaque assay and spot assay 36
10.2 Phage purification 37
10.3 Purifying phage by PEG precipitation 37
10.4 Purifying phage by isopycnic $CsCl_2$ gradient centrifugation 37

10.5 Phage-capsid staining *in vitro* 38
10.6 Phage-DNA staining *in vitro* 38
10.7 Real-time PCR 38
10.8 ϕ29 and SPβ lysis test 39
11 DNA techniques 39
11.1 DNA isolation from *B. subtilis* and *E. coli* 39
11.2 Polymerase Chain Reaction 40
11.3 Agarose gel electrophoresis 40
11.6 DNA digestion and ligation 40
11.7 Site directed mutagenesis 40
11.8 Golden-gate cloning 40
12 Biochemical methods 41
12.1 Protein purification 41
12.2 Protein quantification 41
12.3 Protein concentration 41
12.4 Polyacrylamide gel electrophoresis 42
12.5 Immunoblotting 42
12.6 GTPase activity test by high-performance liquid chromatography (HPLC) 42
12.7 Lipid binding and tethering assays 43
12.8 Lipid mixing assay 43
12.9 Content mixing assay 43
12.10 Nisin staining 44
12.11 Lipoteichoic acid assay 45
13 Microscopy 45
13.1 Fluorescence microscopy 45
13.2 Electron microscopy 45
Results 47
1 Characteristics of DynA-mediated membrane fusion *in vitro* 47
1.1 DynA induces membrane full fusion *in vitro* 48
1.2 The D1 subunit of DynA is crucial for membrane fusion, but cannot stabilize membrane cluster 54
1.3 DynA-induced membrane fusion *in vitro* is a thermo-promoted slow response 58
1.4 DynA exhibits phospholipid preference 62
1.5 DynA-induced membrane remodeling *in vivo* 64
2 DynA mediates resistance to membrane rupture 65
2.1 DynA inhibites bacteriophage-induced host cell lysis 65
2.2 Characteristics of DynA in nisin resistance 76

3 Negative-stain EM of DynA 78
3.1 Sample preparation and image acquisition for electron microscopy 78
3.2 CTF estimation 80
3.3 Manual picking and 2D classificaiton of apo-DynA particles 81
3.4 3D model generation of apo-DynA particles 83
4 Bacteriophage resistance gene candidate screening 89
4.1 Characteristics of DagK in phage resistance 90
4.2 Characteristics of YpmB in phage resistance 93
Discussion 94
1 DynA mediates full membrane fusion 95
2 Characteristics of DynA resistance to membrane rupture 98
3 Towards a DynA structure 101
4 Screening for novel phage resistance genes 102
References 107
Abbreviations 107
Acknowledgements 121

Abstract

Many bacterial species contain dynamin-like proteins (DLPs). DLPs show a high level of functional diversification. DynA in *Bacillus subtilis* is a two-headed DLP, mediating nucleotide-independent membrane tethering *in vitro* and contributing to the innate immunity of bacteria against membrane stress and phage infection. However, so far, the functional mechanisms of the bacterial DLP are poorly understood. Here, the biochemical characteristics of DynA-induced membrane fusion, the mechanisms of DynA-mediated phage resistance and protection effect to antibiotic treatment.

To uncover the biochemical characteristics of DynA-induced membrane fusion, we employed content mixing and lipid mixing assays in reconstituted systems to study if DynA induces membrane full fusion. Further, the individual contribution of its subunits in membrane fusion and the role of GTP hydrolysis of DynA were analysed in detail. Our results based on fluorescence resonance energy transfer (FRET) indicated that DynA could induce aqueous content mixing even in the absence of GTP. Moreover, DynA-induced membrane fusion *in vitro* was a thermo-promoted slow response and showed phospholipid preferences. The D1 subunit of DynA was crucial for membrane fusion, whereas it cannot stabilize the tethered membrane without the help of the D2 subunit. At low temperatures, GTPase activity promoted dissociation of membrane clusters induced by DynA. Surprisingly, the digestion of DynA after hemifusion mediated an instant rise of content exchange, supporting the assumption that disassembly of DynA is the elemental power for fusion-through-hemifusion.

Next, the role of DynA in phage resistance was analyzed. We found that the presence of DynA could delay cell lysis after phage infection, thereby slowing down the release of phage progeny from the host cells. During the process, DynA formed static clusters on the cell membrane. It seems that DynA supports the cell membrane and delays rupture.

Using transmission electron microscopy (TEM), the protein structure of DynA in solution was analyzed. DynA likely formed dimers and trimers, showing a four-corner and hexagonal shape.

In a screening approach, we searched for novel genes that could have a role in phage defence. A *B. subtilis 168* single-gene deletion library was screened. *DagK* and *ypmB* were found to be related to bacteriophage resistance. The presence of DagK can help bacteria resist phage attachment, replication, and host cell lysis. And the role of YpmB against bacteriophages needs to be further verified and characterized.

Zusammenfassung

Viele Bakterienarten enthalten Dynamin-ähnliche Proteine (DLPs). DLPs weisen ein hohes Maß an funktionaler Diversifikation auf. DynA in *Bacillus subtilis* ist ein zweiköpfiges DLP, das *in vitro* die nukleotidunabhängige Membranbindung vermittelt und zur angeborenen Immunität von Bakterien gegen Membranstress und Phageninfektion beiträgt. Bisher sind die Funktionsmechanismen des bakteriellen DLP jedoch kaum bekannt. Hier wurden die biochemischen Eigenschaften der DynA-induzierten Membranfusion, die Mechanismen der DynA-vermittelten Phagenresistenz und die Schutzwirkung gegen Antibiotika in Detail untersucht.

Um die biochemischen Eigenschaften der DynA-induzierten Membranfusion aufzudecken, verwendeten wir Inhaltsmischungs- und Lipidmischungsassays in rekonstituierten Systemen, um zu untersuchen, ob DynA die vollständige Membranfusion induziert. Ferner wurden der individuelle Beitrag seiner Untereinheiten zur Membranfusion und die Rolle der GTP-Hydrolyse von DynA detailliert analysiert. Unsere Ergebnisse basierend auf dem Fluoreszenzresonanzenergietransfer (FRET) zeigten, dass DynA selbst in Abwesenheit von GTP eine Vermischung des Liposomeninhalts induzieren kann. Darüber hinaus war die DynA-induzierte Membranfusion *in vitro* eine thermisch geförderte langsame Reaktion und zeigte Phospholipidpräferenzen. Die D1-Untereinheit von DynA war entscheidend für die Membranfusion, wohingegen sie die angebundene Membran ohne die Hilfe der D2-Untereinheit nicht stabilisieren kann. Bei niedrigen Temperaturen förderte die GTPase-Aktivität die Dissoziation von durch DynA induzierten Membranclustern. Überraschenderweise vermittelte der Verdau von DynA nach der Hemifusion einen sofortigen Anstieg des Inhaltsaustauschs, was die Annahme stützt, dass die Zerlegung von DynA die elementare Kraft für die Fusion durch Hemifusion ist.

Als nächstes wurde die Rolle von DynA bei der Phagenresistenz analysiert. Wir fanden heraus, dass das Vorhandensein von DynA die Zelllyse nach einer Phageninfektion verzögern und dadurch die Freisetzung von Phagennachkommen aus den Wirtszellen verlangsamen kann. Während des Prozesses bildete DynA statische Cluster auf der Zellmembran. Es scheint, dass DynA die Zellmembran unterstützt und den Bruch verzögert.

Unter Verwendung eines Transmissionselektronenmikroskops (TEM) wurde die Proteinstruktur von DynA in Lösung analysiert. DynA bildete wahrscheinlich Dimere und Trimere, die eine viereckige und sechseckige Form zeigten.

In einem Screening-Ansatz suchten wir nach neuen Genen, die eine Rolle bei der Phagenabwehr spielen könnten. Eine *B. subtilis 168*-Einzelgen-Deletionsbibliothek wurde gescreent. Es wurde festgestellt, dass *dagK* und *ypmB* mit der Bakteriophagenresistenz zusammenhängen. Das Vorhandensein von DagK kann Bakterien helfen, die Anhaftung, und die Replikation zu behindern. Zudem wird die Lyse von Wirtszellen vermindert. Und die Rolle von YpmB gegen Bakteriophagen muss weiter verifiziert und charakterisiert werden.

Introduction

1 The Dynamin superfamily

The bacterial dynamin-like protein DynA from *B. subtilis* belongs to the dynamin superfamily that includes classical dynamins in eukaryotes and dynamin-like proteins (DLPs). It is proposed that all dynamin-superfamily members are large mechanochemical GTPases involved in a variety of cellular processes and are major mediators of membrane remodeling. Structurally, dynamin family members are classified by a large GTPase (usually > 60 kDa) domain and a coiled-coil region (Bramkamp, 2012, Sawant *et al.*, 2016). Most of the members share three properties: GTPase activity, oligomerization, and involvement in membrane remodeling. Some of the functions and localizations of classical dynamins and dynamin-like proteins are listed in **Table 1**.

Table 1. Functions of dynamin-superfamily members

Organism	Dynamin homolog	Localization	Function	Source
animals and yeast	Classical dynamins	Cell membrane, *trans*-Golgi network, and endosomes	Vesicle scission	(Praefcke & McMahon, 2004)
	Drp1/Dnm1	Mitochondrial outer membrane	Mitochondrial division	(Mears *et al.*, 2011, Taguchi *et al.*, 2007)
	OPA1/Mgm1	Mitochondrial inner membrane	Mitochondrial fusion and division	(Alavi & Fuhrmann, 2013, Wong *et al.*, 2003)
	Mitofusin/Fzo1	Mitochondrial outer membrane	Mitochondrial fusion and division	(Schrepfer & Scorrano, 2016, Anton *et al.*, 2013)

	Yeast Vps1	*trans*-Golgi network	Vesicle scission	(Chi *et al.*, 2014)
	MxA	Smooth endoplasmic reticulum	viral resistance	(Verhelst *et al.*, 2013, Accola *et al.*, 2002)
	GBPs	Partially membrane associated	Viral resistance and antiproliferative	(Ngo & Man, 2017)
	Atlastin1	endoplasmic reticulum membranes, Golgi	Endoplasmic reticulum tubular network biogenesis	(Orso *et al.*, 2009)
Plants	ADL1A	Cell-plate tubular network	Cytokinesis	(Praefcke & McMahon, 2004)
	ADL1C	Cell-plate: possibly clathrin-coated-vesicle budding	Cytokinesis	
	ADL2A	Plastids	Chloroplast division	
	ADL2B	Mitochondria	Mitochondrial division	
	Phragmoplastin (ADL 4,5)	Cell plate	Cytokinesis	
	ADL6	*trans*-Golgi network	Vesicle scission	
	ARC5	Chloroplasts	Chloroplast division	
Bacteria	*Nostoc punctiforme* BDLP	Cell membrane	Membrane curving	(Low *et al.*, 2009)
	Enterotoxigenic *Escherichia coli* LeoABC	Periplasm (LeoA)	Potentiate virulence through membrane vesicle associated toxin secretion	(Michie *et al.*, 2014)
	Streptomyces DynA and DynB	Sporulation septa	Cytokinesis during sporulation	(Schlimpert *et al.*, 2017)

	Campylobacter jejuni DLP1 and DLP2	membrane	Membrane remodeling	(Liu *et al.*, 2018)
	Mycobacterium smegmatis IniA	Cell membrane	Drug tolerance to the antibiotic isoniazid and ethambutol	(Colangeli *et al.*, 2005)
	Bacillus subtilis DynA	Cell membrane	Antibiotic and phage resistance	(Sawant *et al.*, 2016)

1.1 Classical dynamins

Classical dynamins, including dynamin 1, 2, and 3, are the founding members of the dynamin superfamily (Shpetner & Vallee, 1989, Praefcke & McMahon, 2004), functioning at the heart of endocytic vesicle fission in animal cells. Dynamins contain the following characteristic domains: GTPase domain, a helical stalk domain, pleckstrin homology domain (PH), bundle signaling element (BSE) and C-terminal proline/arginine-rich domain (PRD), a stalk, which connected to the GTPase domain via BSE, a PH domain associated to the other end of the stalk. The PH domain binds to the membrane. A proline-rich domain connects to BSE and extending up to the GTPase domain (Bramkamp, 2012, Antonny *et al.*, 2016). The PH domain mediates membrane binding, and the stalks domain is involved in dynamin oligomerization. Mammalian dynamin 1 is brain-enriched, where it is concentrated in the presynapse; dynamin 2 is ubiquitous (including the brain); dynamin 3 is found in the testis, but is also brain-enriched and is found postsynaptically. Cryo-EM revealed that the dynamin polymer unit is an antiparallel dimer, with the GTPase domains facing outside and the PH domains on the inside, bound to the membrane (Zhang & Hinshaw, 2001, Chen *et al.*, 2004, Mears *et al.*, 2007, Antonny *et al.*, 2016). Crystallographic data also support that non-oligomerizing mutants could be crystallized in an antiparallel dimeric form (Faelber *et al.*, 2011, Ford *et al.*, 2011), shown in **Figure 1**. Dimerization is mediated by the stalks, which form a cross. The two GTPase domains link to one side of the cross whose other side links to the PH domains. Interactions between the stalk dimers drive the assembly into the helical polymer of the expected size, as seen by molecular dynamics of the assembly process (Faelber *et al.*, 2011), identification of the position of mutated residues in non-oligomerizing mutants (Faelber *et al.*, 2011, Ford *et al.*, 2011), and structural insight into the tetrameric form of dynamin 3 (Reubold *et al.*, 2015).

It is reported that dynamins possess the remarkable property of assembling into contractile helical polymers that wrap around membrane tubes, and their GTPase activity promoted the constriction of the polymers and fission of membrane tubes. The most common model is that the GTP hydrolysis cycle translates to a radical conformational change in the protein structure, which forces the polymer to tighten the underlying lipid layers into an energetically unstable

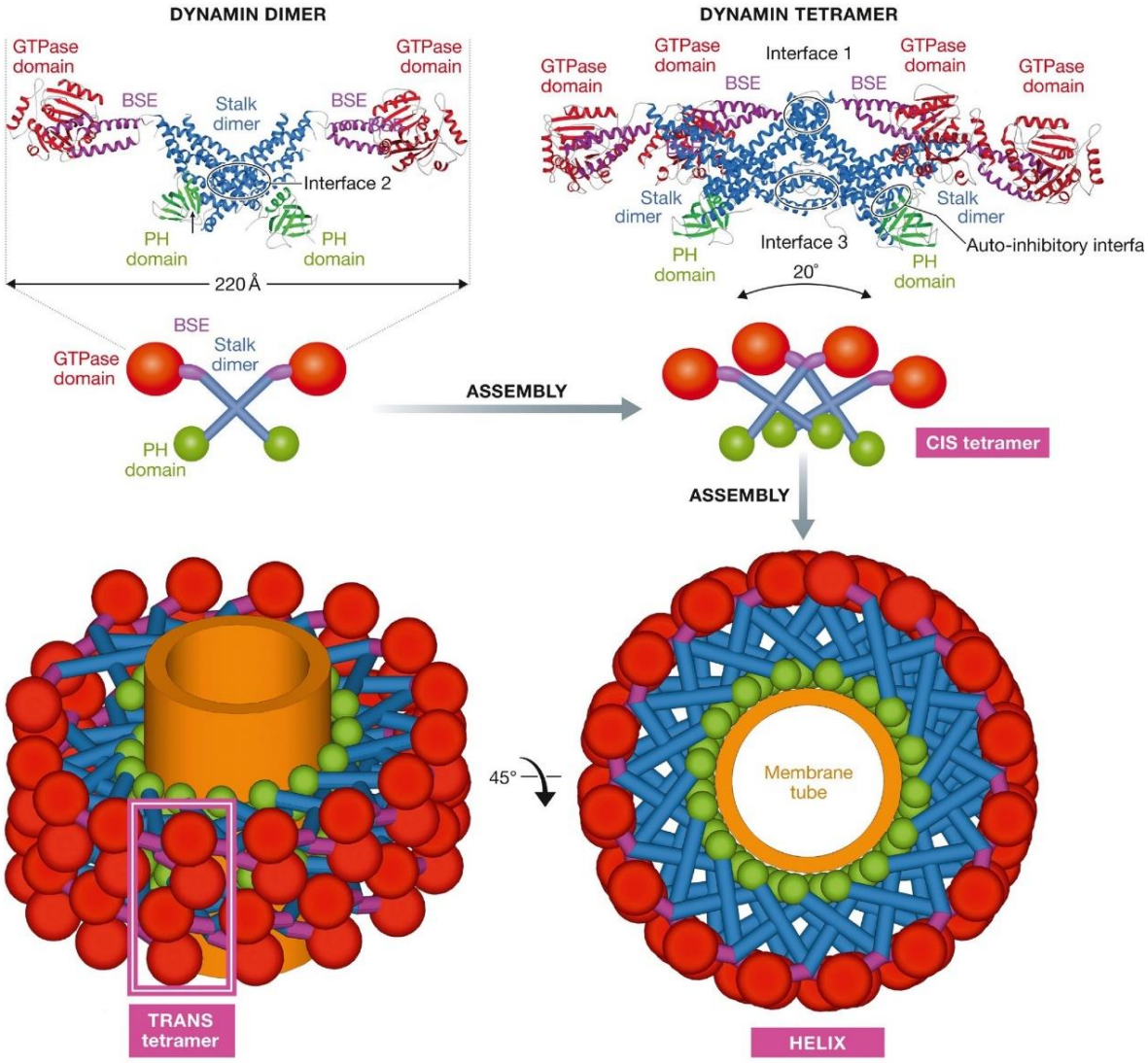

Figure 1. Crystal structure of the dynamin dimer tetramer. The structure showd the interfaces required for assembly. A schematic representation shows how the tetramers further assemble into a helix, showing the basic CIS-and TRANS-tetramers (Antonny *et al.*, 2016).

conformation that further promotes membrane fission. However, there is still a possibility that the final membrane fission is caused by GTP hydrolysis-mediated protein disassembly (Antonny *et al.*, 2016).

1.2 Dynamin-like proteins in eukaryotes

Dynamin-like proteins in eukaryotes include mitochondria-associated OPA1/Mgm1p-like proteins (Ban *et al.*, 2010, Shepard & Yaffe, 1999), Drp1/Dnm1-like proteins (Koirala *et al.*, 2013, Mears *et al.*, 2011), and Mitofusins/Fzo1 (Schrepfer & Scorrano, 2016, Anton *et al.*, 2013), endocytosis-associated Vps1-like proteins (Chi *et al.*, 2014), endoplasmic reticulum Atlastins (Orso *et al.*, 2009), antiviral Mx proteins (Verhelst *et al.*, 2013), anti-parasitic guanylate-binding proteins (GBPs) (Ngo & Man, 2017), and plant ARC5-like proteins (Gao *et al.*, 2003) (**Table 1**). These proteins catalyze a wide variety of membrane fission and fusion events, and some proteins also respond to biotic stress, such as Mx proteins and GBPs.

Through fusion and fission events, mitochondria share membranes, solutes, metabolites, and proteins, as well as electrochemical gradients, coupling them electrically. Mitochondrial fusion is a two-step process requiring three GTPases: Mitofusins for outer mitochondrial membrane fusion and OPA1 (optic atrophy 1) for inner mitochondrial membrane fusion. On the other hand, fission is mediated by the dynamin-related protein Drp 1 (dynamin-related protein 1), another large GTPase, which lacks a bilayer-spanning domain and forms oligomeric spirals to constrict the outer mitochondrial membrane at neck-like junctions where specific adaptors are located. Fusion and fission events permanently counterbalance each other: the inactivation of one activates the other and *vice versa* (Scorrano, 2013, Schrepfer & Scorrano, 2016).

OPA1/Mgm1-like proteins, which are conserved from yeast to humans, lack a PRD domain but have additional amino-terminal mitochondrial import sequences that are followed by a predicted transmembrane and coiled-coil sequence (Praefcke & McMahon, 2004). These proteins are found between the inner and outer mitochondrial membranes and are involved in mitochondrial fusion. Mutations in human OPA1 give rise to dominant optic atrophy (Satoh *et al.*, 2003, Olichon *et al.*, 2002). Mutations of the yeast homolog Mgm1 (mitochondrial genome maintenance 1) lead to mitochondrial fragmentation (Jones & Fangman, 1992, Wong *et al.*, 2003, Praefcke & McMahon, 2004). Various OPA1 short and long isoforms are present in mammals as a result of alternative splicing and proteolysis. Short and long isoforms are required for optimal mitochondrial fusion under normal conditions (Song *et al.*, 2007). However, it has been reported that mitochondrial fusion could occur with only the long OPA1 isoform (Ishihara *et al.*, 2006).

Dynamin-related GTPases Dnm1/Drp1 (yeast/mammals) play conserved roles in mitochondrial fission, which is essential for biological processes including mitochondrial inheritance during

cell division (Gorsich & Shaw, 2004, Taguchi *et al.*, 2007), clearance of defective mitochondria via mitophagy (Parone *et al.*, 2008, Rambold *et al.*, 2011), and mammalian development (Ishihara *et al.*, 2009, Wakabayashi *et al.*, 2009, Koirala *et al.*, 2013). Dnm1 lacks both the PRD and PH domain but contains an uncharacterized B-insert between the middle domain and GTPase effector domain (GED) (Mears *et al.*, 2011, Smirnova *et al.*, 1998). Additional membrane-associated adaptor proteins (Fis1, Mdv1, Mff, and MiDs) are required to recruit these GTPases from the cytoplasm to the mitochondrial surface. The membrane recruitment step is best understood in yeast, where Dnm1 binds to the fungal-specific adaptor mitochondrial division protein 1 (Mdv1) (Cerveny *et al.*, 2001, Tieu & Nunnari, 2000), which in turn binds to the tail-anchored fission protein 1 (Fis1) (Mozdy *et al.*, 2000). Fis1 is conserved in humans, but does not appear to recruit Drp1 to mitochondria. Drp1 recruitment is mediated by mitochondrial fission factor (Mff) or the orthologs mitochondrial dynamics proteins 49 and 51 (MiD49 and MiD51), these are N-terminally anchored in the OMM (Gandre-Babbe & van der Bliek, 2008, Otera *et al.*, 2010, Palmer *et al.*, 2011, Zhao *et al.*, 2011). Neither Mff nor the MiD proteins are related by sequence or predicted secondary structure to Mdv1. Although Fis1 is dispensable for fission, membrane-anchored Mdv1, Mff, or MiDs paired individually with their respective GTPases are sufficient to divide mitochondria. Adaptor protein MiDs alters the architecture of a mitochondrial dynamin GTPase polymer in a manner that could facilitate membrane constriction and severing activity (Koirala *et al.*, 2013).

The mitofusins/fuzzy onions 1 (Fzo1) family of proteins is present from yeast to human and has a predicted transmembrane domain in place of the PH domain (Praefcke & McMahon, 2004, Hales & Fuller, 1997, Hermann *et al.*, 1998, Rapaport *et al.*, 1998, Santel & Fuller, 2001). The proteins are involved in mitochondrial dynamics and localize to the cytoplasmic side of the outer mitochondrial membrane. Mitofusin 1 and Mitofusin 2 (Mfn1 and Mfn2) share approximately 80% similarity (Santel *et al.*, 2003) and the same relevant structural motifs. They also possess two coiled-coil domains (also called heptad-repeat domains, HR1 and HR2). HR2 mediates homotypic or heterotypic (Mfn1-Mfn2) oligomerization by forming a trans, anti-parallel, dimeric coiled-coil that tethers two adjacent mitochondria (Koshiba *et al.*, 2004, Griffin & Chan, 2006). Finally, Mitofusins contain a bipartite carboxy-terminal transmembrane domain, responsible for its anchoring in the outer mitochondrial membrane (Koshiba *et al.*, 2004, Chen *et al.*, 2003, Cipolat *et al.*, 2004). Of note, a proline-rich region, involved in protein-protein interactions, is found only in Mfn2 (Schrepfer & Scorrano, 2016). The tendency of Mfn1-Mfn2 hetero dimerization *in vitro* is even more potent than that of Mfn1 or Mfn2 homo dimerization (Li *et al.*, 2019). Fzo1 is the sole mitofusin homolog in *Saccharomyces*

cerevisiae (Fritz *et al.*, 2001). Fzo1 is embedded in the mitochondrial outer membrane with a transmembrane region that spans the membrane twice, exposing the N- and C-terminal portions to the cytosol and a loop to the intermembrane space (De Vecchis *et al.*, 2017, Griffin & Chan, 2006).

Vps1-like (vacuolar protein sorting 1) proteins lack the PRD, and the region between the middle domain and GED is unlikely to accommodate a PH domain. Yeast has no classical dynamin that works in plasma membrane endocytosis, but Vps1 is involved in vesicle trafficking from the Golgi and probably functions as a classical dynamin homologue without the necessity for multiple targeting sequences because of its limited location (Rothman *et al.*, 1990, Wilsbach & Payne, 1993, Praefcke & McMahon, 2004).

Mx-like proteins are lacking the PRD and the PH domain. At low protein concentrations and physiological salt concentrations, Mx proteins form tetramers in solution. At higher protein concentrations, these tetramers oligomerize further into large filaments and rings (Verhelst *et al.*, 2013, Melen *et al.*, 1992, Kochs *et al.*, 2002, Accola *et al.*, 2002). Expression of the human MxA and MxB proteins is induced by type I interferons, and MxA gives strong protection against viral infection (Staeheli *et al.*, 1986, Janzen *et al.*, 2000). Fish have many interferon-induced Mx homologs, likely an evolutionary adaption to the presence of numerous viruses. All the proteins in the Vps1 and Mx families have a high degree of conservation of the GED and GTPase domains, and therefore these proteins also show oligomerization-dependent GTPase activity (Praefcke & McMahon, 2004).

The crystal structure of guanylate-binding proteins (GBPs) (Prakash *et al.*, 2000b, Prakash *et al.*, 2000a) shows intramolecular interactions that are similar to those that have been predicted for dynamins and therefore, this structure is regarded as a model for the GTPase, middle and GED domains of dynamin (Praefcke & McMahon, 2004). The expression of GBPs is induced by type II interferon, and these proteins have a role in resistance against intracellular pathogens (Anderson *et al.*, 1999, Cheng *et al.*, 1983). GBPs are not found in *Drosophila melanogaster* or *Caenorhabditis elegans*, but there is a weak homolog in *Arabidopsis thaliana*. Unlike dynamin, GBP can hydrolyze GTP not only to GDP but also to GMP (Schwemmle & Staeheli, 1994).

Atlastins are most closely related to the GBP subfamily. They have been identified as crucial proteins in maintaining endoplasmic reticulum morphology and vesicle trafficking in the endoplasmic reticulum/Golgi interface (Zhao *et al.*, 2001, Zhu *et al.*, 2003, Namekawa *et al.*, 2007, Hu *et al.*, 2009). Atlastins lack a GED but instead contain two transmembrane helices

and a C-terminal domain in addition to their large GTPase and middle domains, both of which face the cytoplasm (Rismanchi *et al.*, 2008). The cytoplasmic domain of atlastin acts as a tether, and homotypic interactions are timed by GTP binding and hydrolysis (Byrnes *et al.*, 2013, Byrnes & Sondermann, 2011).

The *A. thaliana* accumulation and replication of chloroplasts mutant 5 (ARC5)-like proteins also lack the PRD and the PH domain. In plants, members of this family are involved in chloroplast division (Gao *et al.*, 2003, Miyagishima *et al.*, 2003). ARC5 localizes to a ring at the chloroplast division site (Gao *et al.*, 2003).

1.3 Bacterial dynamin-like proteins

In more than 1000 bacterial species, DLPs have been identified. Two bacterial DLPs, DynA and DynB in *Streptomyces* stabilize FtsZ rings for completion of septum synthesis during sporulation (Schlimpert *et al.*, 2017). The *Escherichia coli* LeoABC dynamin-like proteins play a role in potentiating virulence through membrane vesicle associated toxin secretion (Michie *et al.*, 2014). The *Mycobacterium tuberculosis* DLP IniA confers drug tolerance to both isoniazid and ethambutol (Colangeli *et al.*, 2005). IniA folds as a bacterial dynamin-like protein with a canonical GTPase domain followed by two helix-bundles, named Neck and Trunk. The distal end of its Trunk domain exists as a lipid-interacting loop, which binds to negatively charged lipids for membrane attachment. IniA mediates nucleotide-independent lipid tethering and exhibits GTP-hydrolyzing dependent membrane fission (Wang *et al.*, 2019). A BDLP from the cyanobacterium *Nostoc punctiforme* (NosDLP) has been characterized as a membrane-binding GTPase, containing a GTPase, stalk domain, and a paddle region identified by its crystal structure. The GTPase domain mediates dimerization, and BDLPs are oligomerized by the parallel association of the BDLP GTPase effector domain (Low & Lowe, 2006, Low *et al.*, 2009), see **Figure 2**. The helical bundle type stem structure closely follows the GTPase domain. The helix in the stem first exits the GTPase domain and then loops back, placing the N and C ends in close proximity. Cyanobacteria BDLP forms dimers both in apolipoprotein and GDP-bound states (Low & Lowe, 2006, Wang *et al.*, 2019). The proximal helical bundle is relative to the GTPase domain (Neck), and the distal helical bundle (Trunk) exhibits a sharp bend. A spiral hairpin called a "paddle" is inserted between the third and fourth helix of the trunk. BDLP binds in the presence of GMPPNP with the paddle domain to the phospholipid membrane. Oligomerization of BDLP leads to tubulation of the liposome (Low & Lowe, 2006, Low *et al.*, 2009, Wang *et al.*, 2019). Polymerization arises through back-to-back longitudinal contacts between GTPase domains, between neck and trunk helices, plus the lateral association of H4

helices (Low *et al.*, 2009). The paddle region of NosDLP has a role in creating the membrane curvature. Upon depolymerization, the outer leaflet is left in a high-energy state, and the two membranes recombine to reduce curvature and to populate the outer leaflet with enough lipid

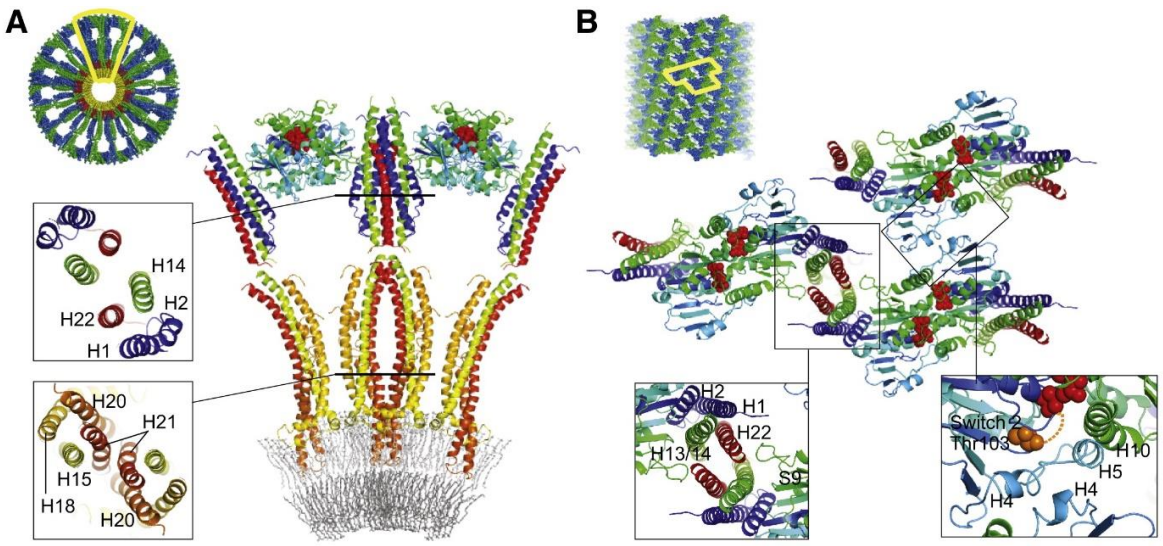

Figure 2. Model of the helical NosDLP filament. (A) Model of the helical NosDLP filament in cross-section to the helix axis showing a fitted lipid bilayer. Shown close up are protein-protein contacts between a pair of asymmetric units. (B) Surface view of the NosDLP filament model. Shown close up is the arrangement of three dimeric asymmetric units within the helix (Low *et al.*, 2009).

molecules to be stable in an aqueous environment (Low *et al.*, 2009).

The pathogen *Campylobacter jejuni* Cj-DLP1 and CjDLP2 form a stable heterotypic tetramer, termed Cj-DLP1/2 tetramer, with 2:2 stoichiometry when mixed. Both Cj-DLP1 and Cj-DLP2 have a core DLP-like fold with GTPase, neck, and trunk domains (Liu *et al.*, 2018). The tetramer is dominated by a 2-fold symmetry where Cj-DLP2 with its symmetry mate form a

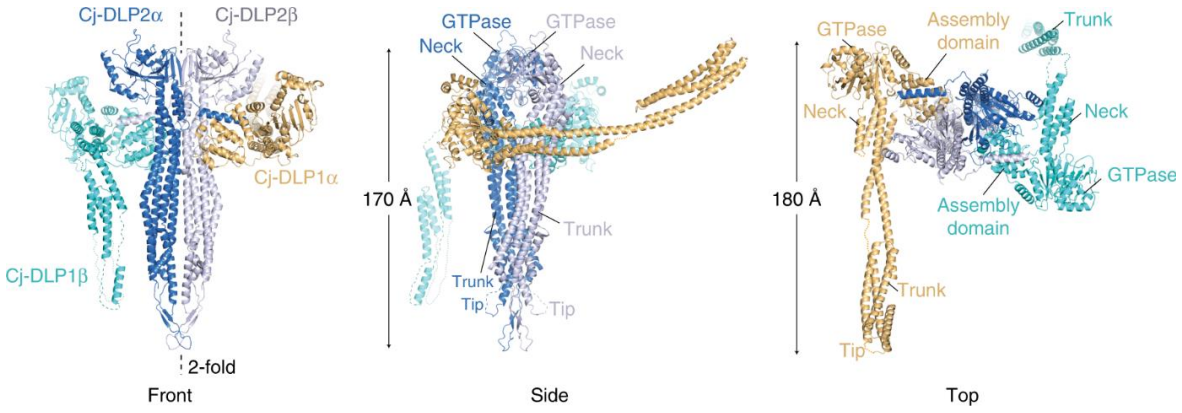

Figure 3. The crystal structure of Cj-DLP1/2 tetramer in the apo state. Cj-DLP1 and Cj-DLP2 exist as a tetrameric oligomer with 2:2 stoichiometry within the asymmetric unit. Cj-DLP2 forms a central back-to-back dimer flanked on each side by Cj-DLP1 subunits (Liu *et al.*, 2018).

central back-to-back cis dimer flanked on each side by Cj-DLP1in the apo state, see **Figure 3**. With respect to Cj-DLP2, the trunk and neck are in an open conformation and together form a linear series of 4-helix bundles. This result, combined with the observation that the NosDLP polymer utilizes a similar back-to-back dimer. Cj-DLP1α forms an open linear conformation (**Figure 2**), whereas the Cj-DLP1β trunk is rotated in-plane ~125° towards the neck C-terminus. Both Cj-DLP1 and Cj-DLP2 mediate lipid binding for although the binding efficiency remains relatively low, while Cj-DLP1/2tetramer shows efficient liposome binding in the absence of nucleotides. The results about Cj-DLP1/2tetramer provide broad mechanistic and structural insights that are relevant to other heterotypic DLP complexes and bridging of opposing membranes by a bacterial DLP pair (Liu *et al.*, 2018).

1.4 Bacterial dynamin-like protein DynA

The *B. subtilis* genome contains a gene *dynA* (*ypbR*), which encodes a large DLP (136 kDa), termed DynA. DynA is a head-to-tail fusion of two dynamin-like subunits (D1 and D2 subunit) and consequently possesses two separate GTPases (Bramkamp, 2012, Burmann *et al.*, 2011). Either two subunits show high structural similarity with NosDLP, except for the lack of the paddle region in the D2 subunit (Bramkamp, 2012). Purified DynA has GTP hydrolytic activity and tethers membranes via the D1 subunit. The role of nucleotide in DynA-induced membrane binding was unclear, given that membrane binding occurs in the absence of nucleotide (Burmann *et al.*, 2011). The membrane-binding process merely requires magnesium as a cofactor. DynA can form dimers in the nucleotide-free state as determined by size exclusion chromatography, and GTPase subunits of DynA show self-interaction symmetry (Burmann *et al.*, 2011). The *B. subtilis* dynamin-like protein DynA helps cells to counteract membrane stress provoked by antibiotics and phages, but the functional mechanisms remained unclear (Sawant *et al.*, 2016). Upon the addition of the lipid II-binding antibiotic nisin, the membrane pores are formed. The formation leads to a rapid assembly of DynA, thereby healing membrane pores and promoting fast recovery of the bacterial population. It is proposed that DynA oligomerizes at the site of membrane damage in static foci, tether the membrane, and catalyze fusion to close the pores. Additionally, it was also observed that DynA knockouts had increased sensitivity (~ 50% higher) to phage infections by the lytic phage Φ29 and the lysogenic phage SPβ compared to the wild-type cells (Sawant *et al.*, 2016).

2 Membrane fusion process

Membrane fusion is an event shared by intracellular trafficking, fertilization, tissue formation, and viral infection (Earp *et al.*, 2005, Jahn *et al.*, 2003, Chernomordik & Kozlov, 2005). On a structural level, fusion results in the unification of the lipid and protein components of the two membranes and the intermixing of the volumes initially bound by them. These hallmarks of fusion are often detected as lipid and content mixing (Chernomordik & Kozlov, 2005). Depending on whether only one leaflet of the bilayer is fused or both leaflets, the fusion process is termed lipid- and content- mixing, respectively.

Because each membrane is composed of two leaflets, the membrane can be merged according to two very different situations (Chernomordik & Kozlov, 2003). The first case assumes that pores are formed in each opposing membrane by transmembrane proteins. The pore rims then join, yielding a fusion pore connecting the membranes, which allows both lipid and aqueous content exchange. We will refer to this pathway as a direct fusion pathway. Alternatively, fusion can proceed via the sequential merger of pairs of membrane leaflets. The first to fuse are the leaflets that face each other through a water gap and are referred to as the proximal or contacting leaflets. Membrane leaflets that are distal with respect to the intermembrane gap remain separate at this stage. This membrane rearrangement called hemifusion allows the exchange of lipids between the proximal leaflets, whereas lipid exchange between the distal leaflets and the exchange of aqueous content remain blocked. The next step is the merger of the distal leaflets, leading to the formation of a nascent fusion pore. Only at this stage would one observe content mixing and the mixing of the lipids of the distal leaflets. This pathway will be referred to as the fusion-through-hemifusion pathway (Chernomordik & Kozlov, 2005). In general, membrane fusion can be separated in various distinct steps in the fusion-through-hemifusion pathway: membrane tethering in trans (termed docking), the formation of hemifusion stalk (hemifusion), and fusion pore expansion to the point at which the vesicle membrane flattens on the membrane interaction surface, leading to the release of the luminal contents (termed full fusion) (Chernomordik & Kozlov, 2005, Zick & Wickner, 2014). Docking of membranes is not sufficient for lipid exchange. Hemifusion is the intermediate stage for membrane full fusion that allows the interaction of lipids between the outer leaflets. In contrast, lipid exchange between inner layers and content mixing is still blocked. Membrane full fusion results in the unification of the lipid bilayer and the intermixing of the volumes.

Membrane fusion in both direct and fusion-through-hemifusion pathways involves drastic structural rearrangements of membrane leaflets, which require special conditions and, in

general, energy input. The pathway that consumes less energy is more probable (Chernomordik & Kozlov, 2005). Because of the high energy cost of pore edges (Chernomordik & Kozlov, 2003, Sandre *et al.*, 1999), direct fusion would be improbable between protein-free bilayers. In contrast, the earliest hemifusion intermediate, called a fusion stalk, has a relatively low energy cost (Kuzmin *et al.*, 2001) and, thus, may form within biologically relevant periods. Indeed, there is reliable evidence for the presence of hemifusion (Chernomordik & Kozlov, 2003, Marrink & Mark, 2004).

For lipid fusion, the soluble N-ethyl maleimide sensitive factor attachment protein receptors (SNAREs) are the universal fusion molecules that are found on many compartments in cells. Similarly, we propose that dynamins are ubiquitous lipid-fission/fusion molecules that have adapted to function at many different compartments in the cell (Praefcke & McMahon, 2004, Weber *et al.*, 1998).

3 Lytic phage Φ29 and prophage SPβ

There is a parasitic relationship between bacteria and bacteriophages (Chaturongakul & Ounjai, 2014). From the perspective of viruses, bacteriophages use host resources to multiply in bacterial cells, and then spread a new generation of viruses into the bacterial population, causing cell lysis and deaths to the host. However, the lysogenic infection cycle of some bacteriophages will also bring some survival or adaptation advantages to the host bacteria (Westra *et al.*, 2012, Menouni *et al.*, 2015). Most bacteriophages have two types of life cycles: the lytic cycle and the lysogenic cycle. The lytic infection cycle begins when viral particles land on the surface of bacterial cells and recognize specific receptors. Landing is followed by complex interactions between cell surface receptors, bacterial membranes, and phages, which ultimately lead to the injection of phage nucleic acids into bacterial cells. The phage then hijacks the host's replication and translation mechanisms to replicate its DNA and synthesize new phage capsids, tails, and tail fibers. After the assembly of newly formed phages reaches a specific number, the phage lyses its host and releases its progeny phage particles, and then continues to infect new host cells. Phages that exhibit this cycle are called lytic phages.

In contrast, the lysogenic cycle causes the phage not actively to propagate and lyse its host but instead inserts its genome into the host's chromosome after the phage enters the cell and replicates along with the host cell's genome (Willey *et al.*, 2008, Raven, 2011). Prophage is a phage that has its genome inserted and integrated into a bacterial DNA chromosome or an extrachromosomal plasmid. A prophage is a latent form of phage in which viral genes are present in bacteria without destroying bacterial cells. At this stage, the prophage and host can coexist for many generations, and this relationship is called lysogenicity. However, upon detection of host cell damage, the prophage is excised from the host chromosome in a process

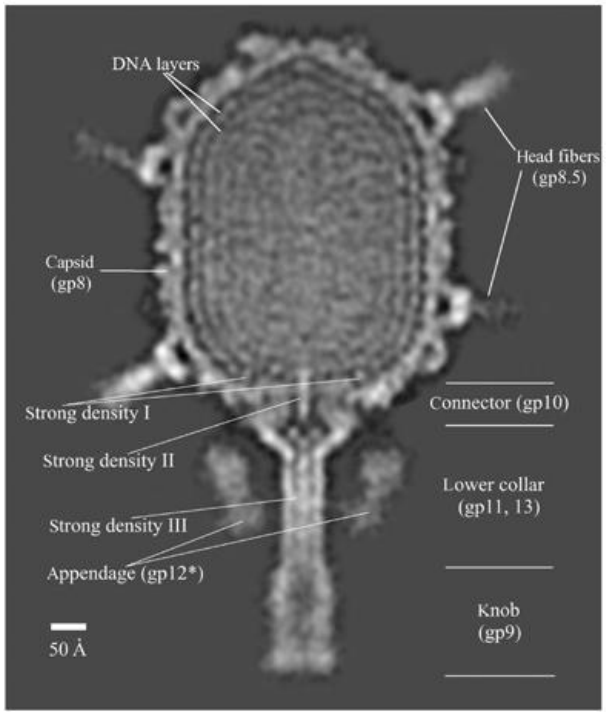

Figure 4. Organization of DNA in mature particles of Φ29. High densities are white, low densities are black. Various structural components of the phage are labeled, including the dominant, well-defined densities I, II, and III. Horizontal lines designate the approximate boundaries of the different tail components (Xiang *et al.*, 2006).

called prophage induction (Canchaya *et al.*, 2003, Willey *et al.*, 2008). After induction, viral replication begins via the lytic cycle. Phages that go through this life cycle are called temperate phages, such as *E. coli* temperate phage λ and P1 (Raven, 2011).

Bacteriophage Φ29 (**Figure 4**) is the smallest *B. subtilis* lytic phage so far, and they have a molecular mass of 18 ± 1×106 daltons. Previous DNA preparations have shown Φ29 DNA to have a molecular weight of about 11×106 daltons. Measurements of the size of the virion

suggest that the head is 41.5×31.5 nm, and the tail is 6.0×32.5 nm. Φ29 forms tiny plaques on lawns of *B. subtilis 168* even though it productively infects this bacterium in the liquid medium. It was reported 40 years ago that the latent period of Φ29 at 37℃ in LB medium is around 45 min and their burst size is 570 (Hemphill & Whiteley, 1975). Φ29 DNA replication and the viral polymerase has been quite extensively studied (Ballesteros-Plaza *et al.*, 2013).

B. subtilis 168 is lysogenic for a temperate bacteriophage called SPβ (**Figure 5**). The virus head is 76 m wide by 82 m long, and the tail measures 12 by 358 m. The DNA molecular weight is 62 million. SPβ is spontaneously released at low levels in cultures of *B. subtilis 168* and can be induced at higher levels by treatment with mitomycin C or N-methyl-N′-nitro-N-nitroso-guanidine (Warner *et al.*, 1977). The attachment site for the prophage of SPβ lies between *ilvA*

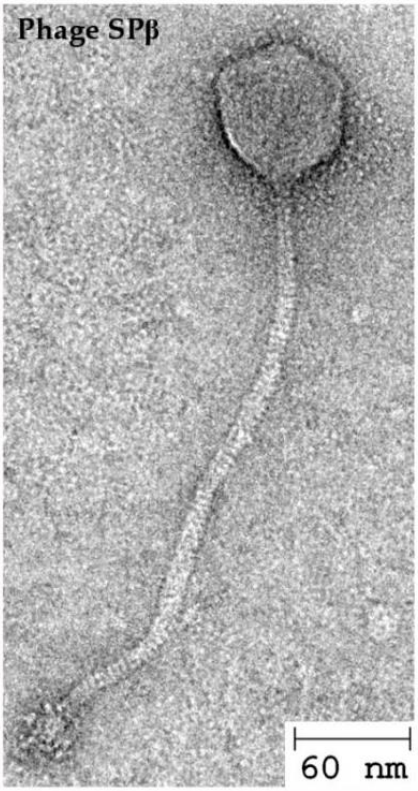

Figure 5. Transmission electron micrograph of a SPβ sample (Sawant, 2015).

and *kauA* on the chromosome of *B. subtilis* strain *168*. Specialized transduction of *citK* and *kauA* can be carried out by certain lysates of SPβ (Zahler *et al.*, 1977).

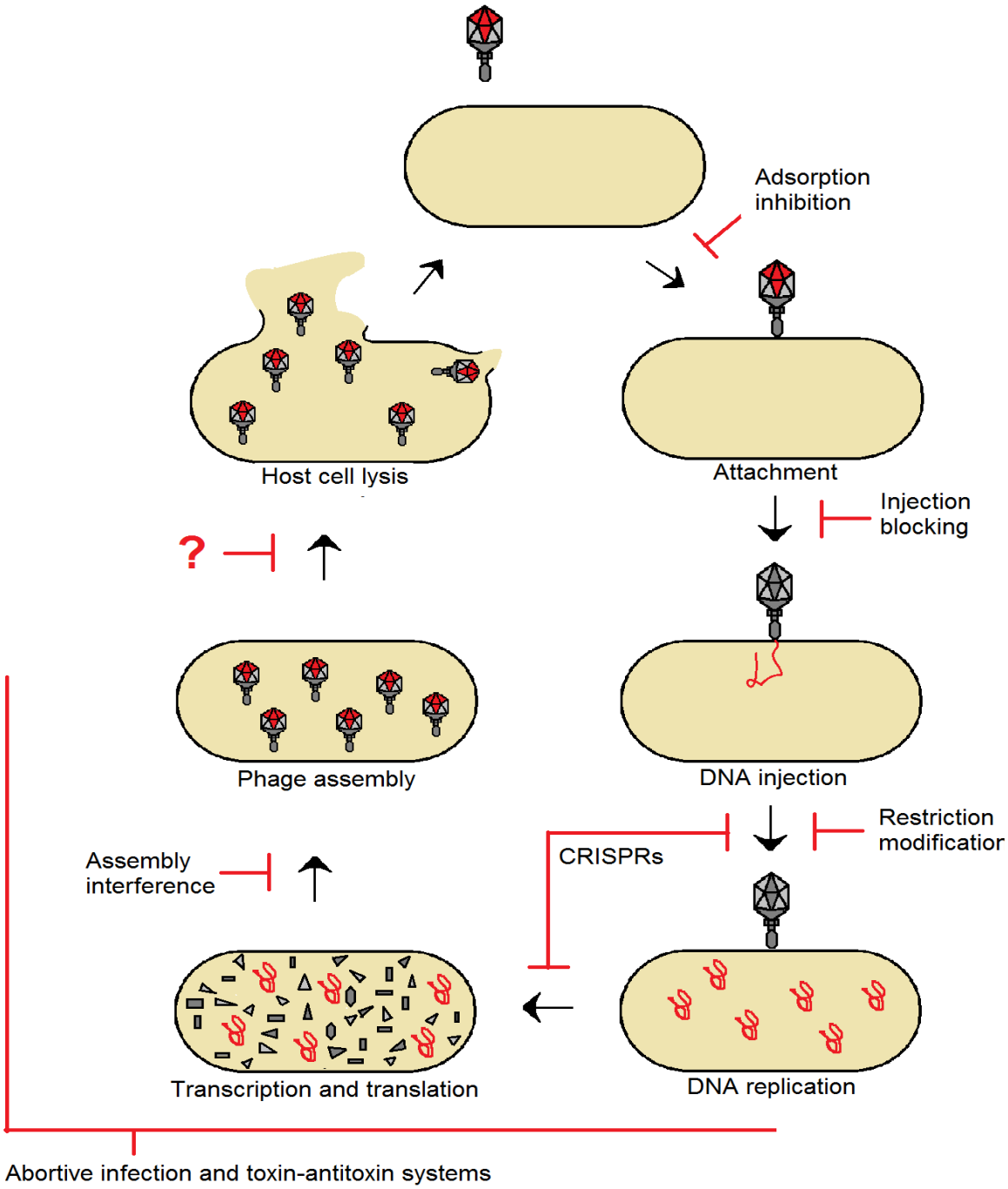

Figure 6. The phage lytic life cycle and the bacterial antiphage systems. Bacteria possess a range of defense strategies that target various phases of the phage life cycle.

4 Bacteriophage resistance mechanisms

Many phages and bacterial resistance mechanisms have been discovered. Phage infection imposes a tremendous pressure on bacteria to develop viral resistance strategies for survival (Seed, 2015, Labrie *et al.*, 2010, Dy *et al.*, 2014), see **Figure 6**. The evolution of bacteria against phage also promotes the anti-resistance evolution of phage. Phages rapidly co-evolve to by-pass bacterial antiviral systems (Samson *et al.*, 2013). Bacteria and bacteriophages are in an endless battle driving constant evolution. Bacteria have evolved mechanistically diverse defense strategies that act almost every stage of the infectious phage cycle. Exactly, bacteria can achieve phage absorption blocking conducted on phage attachment step by blocking phage attachment receptors, production of extracellular matrix to occlude receptors and exploitation of competitive receptor inhibitors (Riede & Eschbach, 1986, Meyer *et al.*, 2012, Nordstrom & Forsgren, 1974, Uhl & Miller, 1996, Liu *et al.*, 2002, Sutherland, 1995, Sutherland *et al.*, 2004, Destoumieux-Garzon *et al.*, 2005); phage DNA injection blocking acted on phage DNA injection step induced by superinfection exclusion proteins that are commonly phage or prophage encoded (Mahony *et al.*, 2008, Folimonova, 2012); phage nucleic acid degradation acted on phage DNA replication to translation step by bacteria restriction modification systems and CRISPR/Cas systems that enable protection from invading DNA (Richter *et al.*, 2012, Barrangou *et al.*, 2007, Sorek *et al.*, 2008, Tock & Dryden, 2005b, Bair & Black, 2007); and abortive infection acted on phage DNA replication to phage assembly step by inhibiting infectious phages formation that enable bacteria suicide before host cell lysis happened (Molineux, 1991, Chopin *et al.*, 2005). Only the last step of the first phage infectious cycle, host cell lysis, no corresponding resistance theory was found.

4.1 Adsorption inhibition

To initiate an infection, phage tails recognize specific cell-surface receptors. Adsorption inhibition is a mechanism in which bacteria alter or block these receptors to avoid phage attachment. There are several known adsorption-blocking strategies in bacteria, such as mutating or masking phage receptors, production of extracellular matrix to occlude receptors, and exploitation of competitive receptor inhibitors (Dy *et al.*, 2014, Labrie *et al.*, 2010).

Some bacteria produce proteins that mask phage receptors. For example, outer-membrane protein A (OmpA) works as an entry receptor for many T-even-like *E. coli* phages (Riede & Eschbach, 1986). As an outer-membrane lipoprotein, TraT encoded by the F plasmid interacts with OmpA and inhibits phage attachment (Achtman *et al.*, 1977). Mutating or deleting genes

encoding phage receptors can lead to decreased susceptibility to phage attack (Koebnik, 1999), but many mutations can be detrimental because many phage receptors play critical cellular roles. In some cases, surface proteins are subject to reversible or temporal expression known as phase variation (Dy *et al.*, 2014). For example, pathogenic *Bordetella* species utilize the two-component regulatory system BvgAS in the control of the infectious cycle (Stibitz *et al.*, 1989). In the virulent Bvg+ phase, characterized by high BvgAS activity, several adhesins, toxins, and Type III secretion systems are expressed, which are important in pathogenesis. In the Bvg− phase, BvgAS is inactive, virulence genes are temporally suppressed, and motility genes are induced. Bacteria can produce small molecules that occupy the active sites of particular receptors, thereby competitively inhibiting phage binding. For example, *E. coli*, FhuA is an iron transporter protein and the receptor of phages T1 and T5. Microcin J25 (MccJ25) is a 21-amino-acid antimicrobial peptide produced under nutrient limitation that binds to FhuA for transport into the cell. MccJ25 was shown to competitively block FhuA, by preventing the interaction between phage T5 and FhuA (Destoumieux-Garzon *et al.*, 2005). However, phages can overcome adsorption-inhibiting defenses by modifying their tail fibers to recognize new or altered receptors (Dy *et al.*, 2014).

Bacteria also produce extracellular polymers, which act as physical barriers against harsh environments while also impeding phage attachment. For example, exopolysaccharides (EPSs) such as alginate and hyaluronan constitute bacterial capsules, and plasmids encoding EPSs can be horizontally acquired and impart an adsorption-blocking phenotype (Forde & Fitzgerald, 2003). However, phages can acquire EPS-hydrolyzing enzymes that enable penetration of the extracellular matrix and allow targeting cellular receptors. These EPS-hydrolyzing enzymes can either are within the tail fibers for direct penetration of the polymeric barrier or be scattered after phage burst to support infection of neighboring bacteria by new viral progeny (Sutherland, 1995).

4.2 Injection blocking

Injection-blocking superinfection exclusion (Sie) systems are commonly phage or prophage encoded and block phage DNA entry, which is a phenomenon that defines the ability of an established viral infection to interfere with secondary infection by the same or a closely related virus, thereby avoiding competition with the secondary virus (Folimonova, 2012). For example, the Sie proteins (Imm and Sp) from T4 are membrane-associated and stop phage DNA translocation of other T-even phage infections (i.e., T2, T4, and T6). Imm directly blocks DNA

injection, whereas Sp inhibits phage-encoded lysozymes, blocking DNA translocation indirectly (Lu & Henning, 1994).

4.3 Degrading phage nucleic acids

Following the passage of phage DNA into the cell, host functions may be redirected. Bacteria possess numerous nucleic acid degrading systems that enable protection from invading DNA. There are two most common strategies described below that can degrade the bacteriophage nucleic acid, the restriction-modification, and CRISPR-Cas systems.

Restriction-Modification (RM) systems exist in bacteria to degrade any invading foreign DNA, including that of viruses. These systems are composed of two enzymes, restriction endonucleases (REases) and cognate methyltransferases (MTases). The former recognizes and cleaves a specific DNA sequence, and the latter modifies it by methylation (Tock & Dryden, 2005a). The activity of both enzymes is mediated by the recognition of specific sequences that are 4-8 bp long. REases recognize the palindromic sequences and rapidly degrade foreign DNA. Since these palindromic recognition sequences can also be present in the host genomic DNA, the host DNA is methylated at specific sites by MTases, to make the host DNA unrecognizable to REases. However, phages also have evolved many strategies to counter the RM systems. Recognition sites within the phage DNA can be substituted through point mutations to prevent or reduce the likelihood of restriction by RM systems (Tock & Dryden, 2005a). For example, in *Lactococcus lactis*, by interchanging the C- and N-terminal variable domains of the parent subunits, recombination of two novel hybrid *hsdS*genes facilitated the formation of chimeric HsdS subunits with altered RM specificities (O'Sullivan *et al.*, 2000). Besides, bacterial Argonaute proteins were shown to act as a barrier for the uptake and propagation of foreign DNA (Olovnikov *et al.*, 2013). Despite the structural similarity to eukaryotic homologs for RNA interference, bacterial Argonaute drives the DNA-directed interference of foreign genetic elements.

Clustered Regularly Interspaced Short Palindromic Repeats (CRISPR)/CRISPR associated proteins (Cas) derived from bacteria and archaea adaptive immune systems that defend against invading DNA (Bhaya *et al.*, 2011, Wiedenheft *et al.*, 2012). Three types (types I, II, and III) of CRISPR-Cas systems have been classified based on the structural organization and functions of nucleoprotein complexes involved in crRNA-mediated silencing of foreign nucleic acids (Xu *et al.*, 2015). All types of CRISPR-Cas systems share a common ability to destroy invading nucleic acids, guided by short CRISPR RNAs (crRNAs). For the type II CRISPR-Cas system, 、

three minimal components, the Cas9 protein, the crRNAs transcribed from the CRISPR locus, and the auxiliary trans-activating crRNA (tracrRNA), are sufficient for DNA recognition and targeting (Sapranauskas *et al.*, 2011, Jinek *et al.*, 2012). The crRNA:tracrRNA duplexes function to direct Cas9 protein for the recognition and targeting, and the duplexes can further be fused with a loop to generate a functional single guiding RNA (gRNA or sgRNA) (Jinek *et al.*, 2012, Guo *et al.*, 2015). However, phages have evolved many mechanisms to evade the CRISPR/Cas machinery in their hosts. For example, anti-CRISPR genes were recently identified in temperate phages that infect *Pseudomonas aeruginosa*. Besides synthesized and packed into the phage capsid, it also could be delivered along with the DNA into the host or encoded immediately after entry into the host (Bondy-Denomy, 2018, Bondy-Denomy *et al.*, 2013).

Bacteriophage exclusion BREX is a novel phage resistance system widespread in microbial genomes against both virulent and temperate phage, which allows phage adsorption but blocks phage DNA replication (Goldfarb *et al.*, 2015). Methylation on non-palindromic TAGGAG motifs in the bacterial genome guides self/non-self discrimination and is essential for the defensive function of the BREX system. Phage DNA does not appear to be cleaved or degraded by BREX, and the exact mechanism of action remains elusive.

4.4 Abortive infection systems

Bacteria carry a wide range of heterologous proteins that provide resistance through the abortion of phage infection. Abortive infection systems (Abi) are ‘altruistic’ cell death systems, which are activated after phage infection, and interrupt different stages of phage development, like transcription, genome replication, and packaging. Abi mediated resistance leads to the death of the cell since the corruption of host functions in that cell is already initiated post phage infection. However, Abi prevents infection of the host population around (Labrie *et al.*, 2010). Currently, there are 23 classified lactococcal Abis (Dy *et al.*, 2014). For example, AbiD1 is one of the most characteristic *Lactococcus* Abi systems, excluding *Lactococcus* bacteriophage 936 and c2 family (Anba *et al.*, 1995). AbiD1 blocked the phage protein ORF3, a RuvC-like endonuclease, which can resolve branched DNA structures during phage DNA replication, failing phage reproduction (Bidnenko *et al.*, 1998). The bacteriophage escapes AbiD1 through spontaneous mutations in its orf1 gene, thereby affecting Orf1's ability to activate translation of abiD1 mRNA (Bidnenko *et al.*, 1995).

Toxin–antitoxin (TA) systems are widespread in many bacteria, and one such system was recently associated with an Abi phenotype (Fineran *et al.*, 2009). TA systems typically encode a toxin gene, which is preceded by an antitoxin gene, and both are transcribed from a joint promoter (Schuster & Bertram, 2013). Some TA systems can be activated in response to invading phages and provide phage resistance through abortive infection. The plasmid-encoded Type III ToxIN system of *Pectobacterium atrosepticum* is an ideal example. The bicistronic *toxIN* locus encodes a cytotoxic endoribonuclease (ToxN), which is neutralized by the repetitive noncoding ToxI RNA through the formation of a heterohexameric RNA-protein complex. Once activated, ToxN cleaves cellular and phage RNA, stopping phage production and inducing bacteriostasis (Fineran *et al.*, 2009, Blower *et al.*, 2011, Blower *et al.*, 2009). However, *P. atrosepticum* ϕTE phage mutants can be isolated that evade ToxIN. The mutants were found to have amplified the pseudo ToxI repeat, thereby producing a structural mimic of the bacterial ToxI RNA, and this mimic was capable of neutralizing ToxN during phage infection (Blower *et al.*, 2012).

4.5 Assembly interference

If the bacteriophages can escape or resist all the above defenses and successfully replicate its genome and complete part of the protein translation, the bacteria still have mechanisms that limit the assembly of phage components or the post-transcription process (Seed, 2015). For example, staphylococcal pathogenicity islands (SaPIs) carry superantigen and resistance genes and are extremely widespread in *Staphylococcus aureus* and other Gram-positive bacteria. SaPIs use several different strategies for phage interference, presumably the result of convergent evolution. One strategy, not described previously in the bacteriophage microcosm, involves a SaPI-encoded protein that directly and interferes explicitly with phage DNA packaging by blocking the phage terminase small subunit. Another strategy involves interference with phage reproduction by the diversion of the vast majority of virion proteins to the formation of SaPI-specific small infectious particles (Ram *et al.*, 2012).

Aims

All BDLPs analyzed so far have a much lower GTP hydrolysis rate, compared to the eukaryotic DLPs, and purified LeoA does not show any GTPase activity, and the role of GTP hydrolysis in these proteins is not known (Colangeli *et al.*, 2005, Low & Lowe, 2006, Burmann *et al.*, 2011, Michie *et al.*, 2014). The *B. subtilis* DynA membrane binding is nucleotide independent. To uncover the mechanism of how DynA works on membrane remodeling and responds to membrane stress, and the role of GTP hydrolysis, three fundamental questions need to be answered: 1) is the BDLP DynA alone sufficient to induce membrane full fusion (content mixing), 2) do both subunits of DynA have distinct functions in the membrane fusion process, and 3) is GTP hydrolysis involved in membrane full fusion? Taking these into consideration, it is necessary to analyze the characteristics of membrane fusion induced by DynA. To test DynA-mediated membrane fusion, we employed assays based on fluorescence resonance energy transfer (FRET). Specifically, we introduced two lipid mixing assays to detect lipid exchange in stages of hemifusion and full fusion, termed lipid FRET and lipid dequenching, as previously described by Zick and Wickner (Zick & Wickner, 2014). One limitation of the lipid mixing assays is that it does not directly discriminate between stages of hemifusion and full fusion. Therefore, a content-mixing assay (termed content FRET here) was used to directly test the exchange of content, addressing whether DynA or DynA plus GTP can lead to complete membrane fusion (Zucchi & Zick, 2011). Generally, we employed content mixing assay and lipid mixing assays in reconstituted systems to study if the dynamin-like protein DynA from *B. subtilis* and its subunits could induce membrane full fusion and further test the possibility that GTP hydrolysis of DynA acts on the fusion-through-hemifusion pathway.

The resistance mechanisms of DynA against phage infection and antibiotic nisin remain unclear. It is first assumed that DynA blocks phage DNA injection by stabilizing membrane integrity, and DynA resists antibiotic pressure by assembling in damaged membrane pores, thereby sealing them. Therefore, we employed fluorescent microscopy, observing the cellular localization of DynA after cells were treated with bacteriophage or nisin. Specifically, we analyzed the infection cycle in wild-type and *dynA*-deletion cells. Phage attachment, phage DNA replication, phage assembly, and host cell lysis will be compared among three strains with different DynA-expression level. Also, we aimed at fluorescently labeling phage DNA and capsid and observed the dynamics of phages in their whole infection cycle. Besides, we used single molecule tracking (SMT) to observe the dynamics of DynA foci on the cell membrane during phage infection.

We employed a transmission electron microscope (TEM) to display the structure of DynA oligomers, thus offering us basic structural information for our understanding of the biological function of DynA. We also started to utilize a knockout gene library of *B. subtilis* to identify novel candidates with phage resistance.

Materials and Methods

1 Materials

2 Chemicals, enzymes and expendables

All materials were obtained from Avanti Polar Lipids, Carl Roth, GE Healthcare, Macherey-Nagel, Merck, Operon, Sigma-Aldrich, Thermo scientific, or Roche. Enzymes were obtained from Invitrogen, Fermentas, or New England Biolabs.

3 Media and buffers

T2 buffer	50 mM Tris, 200 mM NaCl, 10 mM imidazole, 10% glycerol[vol/vol], pH 8.0
T5 buffer	50 mM Tris, 500 mM NaCl, 10% glycerol, pH 8.0
T5 buffer (1 M)	50 mM Tris, 500 mM NaCl, 1M imidazole, 10% glycerol[vol/vol], pH 8.0
T1.5 buffer	50 mM Tris, 150 mM NaCl, pH 8.0
H1.5 buffer	20 mM HEPES, 150 mM NaCl, 5 mM $MgCl_2$, 10% glycerol [vol/vol], pH 7.4
Gelatin-free SM buffer	100 mM NaCl, 25mM Tris, 8 mM $MgCl_2$, pH 7.5
H1.5 buffer (K+)	20 mM HEPES, 150 mM KCl, 5 mM $MgCl_2$, 10% glycerol [vol/vol], pH 7.4
Gelatin-free SM buffer	100 mM NaCl, 25 mM Tris, 8 mM $MgCl_2$, pH 7.5
Gelatin-free SM buffer (1M)	1 M NaCl, 25 mM Tris, 8 mM $MgCl_2$, pH 7.5
10X PC buffer	K_2HPO_4 (dibasic anhydrous) 107 g, KH_2PO_4 (monobasic anhydrous) 60 g, Sodium citrate.5 H_2O 10 g, add dH_2O to 1 L
MD medium	10 X PC 1 ml, 40% [vol/vol] glucose 500 µl, 0.2% [vol/vol] L-tryptophan 250 µl, 2.2 mg/ml ferric ammonium citrate 50 µL, 50 mg/mL L-aspartate 500 µL, 1M $MgSO_4$ 30 µl, add dH_2O to 10 ml, pH 7.0

LB medium	10 g/L tryptone, 5 g/L yeast extract, 10 g/L NaCl, pH 7.0
LB agar medium	10 g/L tryptone, 5 g/L yeast extract, 10 g/L NaCl, 15 g/L Agar, pH 7.0
TFB1 buffer	100 mM RbCl, 50 mM $MnCl_2$, 30 mM KAc, 10 mM $CaCl_2$, 15% glycerol [vol/vol], pH 5.8
TFB2 buffer	10 mM MOPS, 10 mM RbCl, 75 mM $CaCl_2$, 15% glycerol [vol/vol], pH 8.0
4X loading buffer	150 mM Tris/HCl pH 7.0 / 25°C, 12% SDS, 6% mercaptoethanol, 30% glycerol, 0.05% Coomassie G-250
TAE buffer	40 mM Tris, 1.1% acetic acid, 1 mM EDTA, pH 8.0 / 25°C
Immunoblotting washing buffer	0.15 M NaCl, 3 mM KCl, 10 mM Na_2HPO_4, 2 mM KH_2PO_4, 0.1% (w/v) Tween 20, pH 7.4

4 Antibiotics

Nisin	stock: 30 mg/ml, final: 30 μg/ml
Carbenicillin	stock: 100 mg/ml; final: 100 μg/ml
Spectinomycin	Stock:100 mg/ml; final: 100 μg/ml

5 Oligonucleotides

Name	**Description**		
LJ-M01	DynAmut-R512A-f	GGCGATCGGTTTTCTCTGC GGCATTATTCTCTAAACG	48.7% GC, Tm: 78.3°C
LJ-M02	DynAmut-R512A-r	CGTTTAGAGAATAATGCCG CAGAGAAAACCGATCGCC	48.7% GC, Tm: 78.3°C
LJ-M03	DynAmut-R517A-f	CAAATGGCCCACAGGGCA TCGGTTTTCTCTCGG	57.6% GC, Tm: 78.8°C
LJ-M04	DynAmut-R517A-r	CCGAGAGAAAACCGATGC CCTGTGGGCCATTTG	57.6% GC, Tm: 78.8°C
LJ-M05	R512AR517A-DynA-seq-f (before 1783 bp)	ACAACATGCTGCATTCGCC	52% GC, Tm: 61°C

LJ-M06	R512AR517A-DynA-seq-r (after 719 bp)	CGGATCACCCGTTCAATCAG	53% GC, Tm: 62°C
LJ-M07	seq for sequence before GFP	GAAAAGTTCTTCTCCTTTACTCAT	33% GC, Tm: 53.2°C
LJ-M08	seq for sequence after DynA	CGAAGCTGTACGGATG	56% GC , Tm: 49.5°C
LJ-M09	EcoRI-Dendra2-f	CAGGAATTCATGAACACCCCGGGAATTAACC	50% GC, Tm: 63.7°C
LJ-M10	SpeI-Dendra2-r	GAAACTAGTTTACCACACCTGGCTGGGC	63% GC, Tm: 62.8°C
LJ-M11	1-BsaI-pKill-ACTA-f	CGAGGTCTCAACTATTACCC	Tm: 58°C
LJ-M12	1-BsaI-pKill-TCGG-r	CACGGTCTCATCGGG	Tm: 58°C
LJ-M13	2-Bsal-CCGA-partDynA-f	CTAGGTCTCTCCGACCCGGGCTGCAAAAC	67% GC, Tm: 58°C
LJ-M14	2-Bsal-CTCC-partDynA-r	TATGGTCTCCCTCCCATTTTTATTGTATTGTCTGAATTTTTC	21% GC, Tm: 57°C
LJ-M15	3-Bsal-GGAG-GA-Dendra2-f	AATGGTCTCTGGAGGAATGAACACCCCGGGAATTAACC	50% GC, Tm: 63.7°C
LJ-M16	3-Bsal-CGAA-Dendra2-r	TTTGGTCTCGCGAATTACCACACCTGGCTGGGC	63% GC, Tm: 62.8°C
LJ-M17	4-Bsal-TTCG-sspecs-f	GGAGGTCTCTTTCGAACCTCACACCATTCCG	53% GC, Tm: 62°C
LJ-M18	4-Bsal-CATT-sspecs-r	CACGGTCTCCCATTCAGGCTTTGAAGCATGC	53% GC, Tm: 62°C
LJ-M19	5-Bsal-AATG-downDynA-f	ACGGGTCTCAAATGAATTCAGTTGGCTTGTATT	32% GC, Tm: 48.2°C
LJ-M20	5-Bsal-TAGT-downDynA-r	CGGGGTCTCTTAGTGATACAGTCATCCGCTTCA	47% GC, Tm: 52.9°C

LJ-M21	3-BsaI-GGAG-GA-PAmcherry-f	AATGGTCTCTGGAGGAATGGTGAGCAAGGG	57% GC Tm: 57°C
LJ-M22	3-BsaI-CGAA-PAmcherry-r	TTTGGTCTCGCGAATTACTTGTACAGCTCG	44% GC, Tm: 54°C
LJ-M23	KpnI-DynA-f	ACGGGTACCATGACAGATCAAAACAGAAAAG	32% GC, Tm: 52.3°C
LJ-M24	EcoRi-Mcherry2-f	CAGGAATTCATGGTCAGCAAGGGAG	56% GC, Tm: 61°C
LJ-M25	Mcherry2-SpeI-R	GACACTAGTTTATTTGTATAATTCGTCCATTCC	29% GC , Tm: 58°C
LJ-M26	NcoI-YpbS-f	GTCCATGGGATCAGAGGTACATAAAGCAA	37% GC, Tm: 57°C
LJ-M27	XhoI-His6-YpbS-r	GCTCGAGCTAGTGATGGTGATGGTGATGGCTGCTGCCCATGCGGCTTACGTATTC	50% GC, Tm: 61°C
LJ-M28	NcoI-YpbQ-f	GTCCATGGGATTTTGGTTGTTGATCGCC	44% GC, Tm: 61°C
LJ-M29	XhoI-His6-YpbQ -r	GCTCGAGCTAGTGATGGTGATGGTGATGGCTGCTGCCTTTTACGCTGTATTCCTG	39% GC, Tm: 56°C
LJ-M30	NcoI-YpzF-f	GTCCATGGGATTGGGCAGAACAAAGC	50% GC, Tm: 60°C
LJ-M31	XhoI-his6-YpzF-r	GCTCGAGCTAGTGATGGTGATGGTGATGGCTGCTGCCATCGTTGTGTCTTTTG	38% GC, Tm: 53°C
LJ-M32	qPCR-phi29-*gp8*-f	GTCAGGGCGATAACTTCA	Tm: 60°C
LJ-M33	qPCR-phi29-*gp8*-r	TACGATCAACAAGGGACG	Tm: 60°C

6 Plasmids

Name	**Description**		
LJ-P01	carb	*pSG1154-GFP*	Lab collection
LJ-P02	carb	*pKill*	Lab collection

LJ-P03	carb	*pSG1154-DynA-GFP*	Lab collection
LJ-P04	carb	*pSG1154-K56A-K625A-DynA-GFP*	Lab collection
LJ-P05	carb	*pSG1154-D1-YFP*	Lab collection
LJ-P06	carb	*pSG1154-R512A-DynA-GFP*	This work
LJ-P07	carb	*pSG1154-R517A-DynA-GFP*	This work
LJ-P08	carb	*pSG1154-R512A-R517A-DynA-GFP*	This work
LJ-P09	carb	*pSG1154-DynA-Dendra2*	This work
LJ-P10	carb	*pSG1154-K56A-K625A-DynA-Dendra2*	This work
LJ-P11	carb	*pkill-partDynA-dendra2*	This work
LJ-P12	carb	*pkill-partDynA-PAmCherry*	This work
LJ-P13	carb	*pET16b-DynA-his*	Lab collection
LJ-P14	carb	*pET16b-D1-his*	Lab collection
LJ-P15	carb	*pET16b-D2-his*	Lab collection
LJ-P16	carb	*pET16b-K56A-D1-his*	Lab collection
LJ-P17	carb	*pET16b-K625A-D2-his*	Lab collection
LJ-P18	carb	*pET16b-K56A-K625A-DynA-his*	Lab collection
LJ-P19	carb	*pET16b-YpbS -his*	This work
LJ-P20	carb	*pET16b-YpbQ -his*	This work
LJ-P21	carb	*pET16b-YpzF -his*	This work
LJ-P22	carb	*pSG1154-mCherry2*	This work
LJ-P23	carb	*pET16b-R512A-DynA -his*	This work
LJ-P24	carb	*pET16b-R517A-DynA -his*	This work
LJ-P25	carb	*pET16b-R512A-R517A-DynA -his*	This work

7 *E. coli* strains

Name	**Description**	
LJ-E01	*Ecoli NEBTurbo*	Lab collection
LJ-E02	*Ecoli DH5α*	Lab collection
LJ-E03	*Ecoli BL21(DE3)*	Lab collection

8 *B. subtilis* strains and bacteriophage

Name	Description	
LJ-B01	*Bacillus subtilis 168*	Lab collection
LJ-B02	*Bacillus subtilis 168, ⊿dynA*	Lab collection
LJ-B03	*Bacillus subtilis 168, ⊿dynA, amyE::Pxyl-dynA-gfp-spec*	Lab collection
LJ-B04	*Bacillus subtilis 168, ⊿dynA, amyE::Pxyl-K56A-K625A-dynA-gfp-spec*	Lab collection
LJ-B05	*Bacillus subtilis 168, ⊿dynA, amyE::Pxyl-D1-yfp-spec*	Lab collection
LJ-B06	*Bacillus subtilis 168, ⊿dynA, amyE::Pxyl-D2-gfp-spec*	Lab collection
LJ-B07	*Bacillus subtilis 168, ⊿dynA, amyE::Pxyl-R512A-dynA-gfp-spec*	This work
LJ-B08	*Bacillus subtilis 168, ⊿dynA, amyE::Pxyl-R517A-dynA-gfp-spec*	This work
LJ-B09	*Bacillus subtilis 168, ⊿dynA, amyE::Pxyl-R512A-R517A-dynA-gfp-spec*	This work
LJ-B10	*Bacillus subtilis 168, ⊿dynA, amyE::Pxyl-dynA-dendra2-spec*	This work
LJ-B11	*Bacillus subtilis 168, DynA::dynA-dendra2-spec*	This work
LJ-B12	*Bacillus subtilis 168, DynA::dynA-pamcherry-spec*	This work
LJ-B13	*Bacillus subtilis 168, ⊿dynA, amyE::Pxyl-K56A-K625A-dynA-dendra2-spec*	This work
LJ-B14	*Bacillus subtilis 168, ⊿dynA, amyE::mcherry2*	This work
LJ-B15	*Bacillus subtilis 168, amyE::gfp*	This work
LJ-B16	*Bacillus subtilis 25152*	Lab collection
LJ-B17	*Bacillus subtilis 25152, ⊿dynA*	Lab collection
LJ-B18	*Bacillus subtilis 168, ⊿spo0A*	single-gene deletion library (Addgene)

LJ-B19	*Bacillus subtilis 168, ⊿clpC*	single-gene deletion library (Addgene)
LJ-B20	*Bacillus subtilis 168, ⊿ypmB*	single-gene deletion library (Addgene)
LJ-B21	*Bacillus subtilis 168, ⊿dagK*	single-gene deletion library (Addgene)
LJ-B22	*Bacillus subtilis 168, ⊿ugtP*	single-gene deletion library (Addgene)
LJ-B23	*Bacillus subtilis 168, ⊿pssA*	single-gene deletion library (Addgene)
LJ-B24	*Bacillus subtilis 168, ⊿psD*	single-gene deletion library (Addgene)
LJ-B25	*Bacillus subtilis 168, ⊿pgsA*	single-gene deletion library (Addgene)
LJ-B26	*Bacillus subtilis 168, ⊿clsA*	single-gene deletion library (Addgene)
LJ-B27	*Bacillus subtilis 168, ⊿ltaSA*	single-gene deletion library (Addgene)
LJ-B28	*Bacillus subtilis 168, ⊿yqgS*	single-gene deletion library (Addgene)

Bacteriophage Φ29 and prophage SPβ of *B. subtilis* was purchased from the Leibniz Institute DSMZ - German Collection of Microorganisms and Cell Cultures GmbH (Deutsche Sammlung von Mikroorganismen und Zellkulturen GmbH).

9 Cultivation of bacteria and bacteriophage

9.1 Storage and growth conditions

For long term storage, *B. subtilis* and *E. coli* cells were kept in 25% glycerol and stored at -80 °C. For short term storage, *E. coli* were kept at 4°C, whereas *B. subtilis* was kept at 24°C. The optimum growth temperature for both *E. coli* and *B. subtilis* was 37 °C, and both can effectively thrive in the LB medium. *B. subtilis* was cultured in the minimal medium MD for fluorescence microscopy and DNA transformation. The bacteriophage Φ29 and phage SPβ were stored in Gelatin-free SM buffer at 4°C, and their high infectious activity (>1%) could be

maintained for more than six months, or stored in LB medium at 4°C, their high infectious activity could be maintained for about one month.

9.2 Transformation of *E. coli*

Overnight cultures from glycerol stock were inoculated in LB medium (100-fold dilution; in total 100 ml) and grown up to OD600 = 0.5 at 37℃. Cells were harvested by centrifugation about 5 min at 4,500 rpm at 4℃, and then the cells were re-suspended in 30 ml cold TFB 1 buffer. Cells were kept on ice for 90 min. Cells were again centrifuged and re-suspended in 4 ml cold TFB 2 buffer. Competent cells were directly transformed or snapped in liquid nitrogen and stored at -80℃. 50 μl competent cells and 50 ng ligation product or ten ng plasmid were mixed for transformation. The mixture of cells and DNA was left on ice for 30 min before heat-shock. Cells were heat-shocked for 30 ~ 45 s at 42℃ and then placed on ice immediately for 5 ~ 8 min. One ml of pre-warmed LB medium was added and then incubated for 1 hour before plating.

9.3 Transformation of *B. subtilis*

A loop of freshly plated cells was used to inoculate 10 ml MD medium supplemented with 0.1% casamino acids (CAA) and grown up to OD_{600}=1.0 ~ 1.5 at 37℃. Ten ml of pre-warmed MD medium was then added and grown for 1 hour. Cells were competent now. Each transformation tube was added with 800 μl competent cells and 1 μg DNA, then incubated for 20 min. 25 μl 20% CAA was then added to each tube and incubated for 1 hour before plating.

10 Bacteriophage techniques

10.1 Quantitative plaque assay and spot assay

Overnight cultures of *B. subtilis* from glycerol stock were 100-fold diluted in fresh LB medium and grown up to an OD_{600} of 0.5 to 1.0. Bacteriophages were diluted with 10-fold serial (1 to 10^{10}) in the LB medium. For plague assays, each dilution of phage (100 μl) was mixed with 1 ml bacteria solution, and the infection process was allowed to proceed 10 min at room temperature. Then the mixtures were added to 4 ml warm LB with 0.5% agar and poured on LB agar plates. For spot assay, 1 ml bacteria were mixed with 4 ml warm LB with 0.5% agar and poured first, then each dilution of phage (5 μl) was dropped to the plate. Phage plaques could be detected after 6 hours of incubation at 37°C or overnight (< 25 hours) at 24°C.

10.2 Phage purification

Bacteriophages were separated from bacteria by centrifugation at 6000 g for 10 min. The supernatant contained bacteriophage and cell debris. The supernatant was centrifuged again at 13000 g for 2 hours. The supernatant was carefully removed, and the gelatin-free SM buffer was added to the pellet. The phage suspension was again spun down at 13000 g for 10 min to separate cell debris and phages.

10.3 Purifying phage by PEG precipitation

Bacteriophages were separated from bacteria by centrifugation at 6000 g for 10 min. The supernatant contained bacteriophages and cell debris. Solid NaCl was added to the supernatant to a final concentration of 1M and stirred until dissolved. Then solid PEG-8000 was added to a final concentration of 10% (100 mg/ml) and stirred for at least 30 min. The phages were collected by centrifugation at 13000 g for 10 min. The supernatant was carefully removed, and the gelatin-free SM buffer was added (> 1/5 of the original volume) to the pellet. The phage suspension was again spun down at 13000 g for 10 min to separate cell debris.

10.4 Purifying phage by isopycnic $CsCl_2$ gradient centrifugation

1 L of a bacteria-phage mixture with a phage titer above 10^9 PFU/ml was prepared. Bacteriophages were separated from bacteria by centrifugation at 6000 g for 10 min. The supernatant contained bacteriophages and cell debris. Cell debris was removed by the above centrifugation method, and the bacteriophages were concentrated to 10 ml. The solution was transferred to a 10 ml Falcon tube. Solid CsCl was slowly added, and the tube was gently swirled for the solution of solid CsCl. The final density of CsCl should be about 1.40 g/ml. The phage-CsCl solution was transferred to ultracentrifuge tubes and run 24 hours at 45000 rpm using Beckman 70.1 Ti rotor. The phage formed a grey-white band and could be sampled with a syringe. Extracted phage solution (~3 ml) was added to a ten kDa cutoff dialysis cassette. The solution was dialyzed overnight against 500 ml of gelatin-free SM buffer containing 1M NaCl at 4℃. The dialysis cassette was then transferred to 500 ml of gelatin-free SM buffer and dialyzed for 2-3 hours at room temperature. The second dialysis process was repeated once. Finally, the phage preparation was sterile filtered (pore size 0.45 μm) and stored at 4℃.

10.5 Phage-capsid staining *in vitro*

CsCl-purified phage (500 µl) was mixed with 5 µl Alexa Fluor 647 (Succinimidyl ester, 1 mg/ml in DMSO) and incubated for 1 hour in room temperature. The PEG purification method was used to separate stained phage from the free dye. Illustra NAP-5 column was then used to enhance the ratio of properly labeled phages. The column was equilibrated with a 10 ml gelatin-free SM buffer, and then 500 µl of stained phage solution was loaded. Every drop (~ 50 µl) was collected in 200 µl PCR tubes, fluorescence intensity, and bacteria optical density was recorded with an Infinite200 PRO (Tecan, Grödig, Austria) fluorescent plate reader. The sharp drop of bacteria optical density change after phage addition reflects high phage activity. For this, two µl of drops were added to 198 µl gelatin-free SM buffer in a 96-black plate. Fluorescence intensity at 630/670 (Ex/Em) was measured. 2 µl of labeled phage solution respectively added to 198 µl fresh bacterial lipid of *B. subtilis* (OD = 0.5) in a 96-transparent plate and measure the absorbance intensity of 600 in 6 hours with a 30-min interval for phage activity. Fractions with high fluorescence signal and phage activity were added and stored until further use.

10.6 Phage-DNA staining *in vitro*

CsCl-purified phages (500 µl) were mixed with 5 µl hochest (1 mg/ml in H_2O) and rotated for 1 hour at room temperature. 1M NaCl and 10% PEG-8000 were sequentially added to the solution and stirred for at least 30 min. Subsequently, the solution was centrifuged at 13000 g for 10 min. The pellet was re-suspended in gelatin-free SM buffer (> 1/5 of the original volume) and centrifuged again at 13000 g for 10 min to obtain its supernatant. The NaCl/PEG clean-up was repeated once.

10.7 Real-time PCR

Bacteria, grown at 37°C up to an OD 600 of 0.5 in LB medium, were infected with ϕ29 at an MOI of 10. All strains were incubated for 10 min at 24°C for phage attachment, then placed in a 37°C shaker and timed. Cell corresponding to 500 µl aliquots of *B. subtilis* cultures was collected every 15 min. For the determination of intracellular and extracellular phage DNA samples, cells and supernatants were separated by centrifugation at 6000 g for 2 min, and 500 µl buffer was added to the pellets. The samples were added with 50% chloroform to interrupt the phage infection process and centrifuged at 16000 g for 10 min to remove cell debris and protein. Analysis of the DNA samples was performed by real-time PCR with KAPA SYBR FAST Universal Kit in a Light-Cycler (Primers used here were *ϕ29-gp8-F*:

GTCAGGGCGATAACTTCA and *ϕ29-gp8-R*: *TACGATCAACAAGGGACG*). The data obtained for each DNA sample was interpolated to a standard curve constructed with known amounts of purified, full-length ϕ29 DNA. ϕ29 DNA was isolated using the Invitrogen PureLink genomic DNA Kit.

10.8 ϕ29 and SPβ lysis test

In the ϕ29 lysis test, *B. subtilis* strains were freshly cultured to OD600 =0.5 in LB medium, then mixed with phage ϕ29 at an MOI of 1.0 and incubated at 37°C for 1 hour. External phages were obtained by centrifugation at 6000 g for 2 min. For the entire assembled phages, the samples were first added with 1% chloroform, then mixed by ten tube inversions, and finally centrifuged. A spot assay was performed on the lawn of the *dynA*-knockout 168 strain to measure the phage titers. In the SPβ lysis test, 5 μg/ml mitomycin was added to the bacterial liquid of wild-type and *dynA*-, *dagK*- or *ypmB*- knockout 168 strain and shaken at 37°C for 30 min, after which mitomycin was washed away with fresh LB medium. Lysed SPβ was counted with a quantitative spot assay that was performed on the lawn of the SPβ-lysable *dynA*-knock-out *25152* strain (Sawant *et al.*, 2016).

11 DNA techniques

11.1 DNA isolation from *B. subtilis* and *E. coli*

For isolation of *B. subtilis* genomic DNA (gDNA), freshly plated cells were collected with an inoculation loop and suspended in 200 μL sterile water. The cell suspension was mixed with 200 μL phenol (pH 6.5) and incubated for 10 minutes at 65°C in a water bath. The cell-phenol suspension was cooled on ice and vortexed extensively with 200 μl chloroform:isoamylalcohol (24:1) solution. The mixture was centrifuged at 13000 g for 6 minutes at 4°C. The supernatant was transferred into a new tube and mixed with 200 μl chloroform:isoamylalcohol (24:1) solution, which was subjected to centrifugation. 100 μl of the supernatant containing DNA was collected into a new tube and kept at -20°C. Plasmids were isolated from *E. coli* cells by use of the NucleoSpin Plasmid kit (Macherey-Nagel) and kept at -20°C. DNA was quantified photometrically by measuring absorbance at 280 nm.

11.2 Polymerase Chain Reaction

Polymerase chain reaction (PCR) for molecular cloning was performed with Phusion high fidelity DNA polymerase (NEB) according to the supplier's instructions. For the amplification of genomic sequences, either purified chromosomal DNA or cell lysate was used as a template. Lysates were prepared by high-temperature lysis in an 80°C water bath for 5 minutes, or a 95°C lysis procedure for 3 ~ 5 min at the beginning of the PCR cycle. For analytical PCR, *Taq* DNA polymerase (EconoTaq PLUS GREEN 2x Mastermix) was used when appropriate.

11.3 Agarose gel electrophoresis

Electrophoresis was performed with gels of 1% agarose in TAE buffer using a BioRad MiniSUB Cell GT at 110 V. Gels were stained with 5 mg/l ethidium bromide. The sizes of DNA-fragments were quantified by the exponential fit of a size marker. DNA in gels were isolated with a NucleoSpin DNA clean-up Kit (Macherey-Nagel).

11.6 DNA digestion and ligation

Restriction of DNA with endonucleases was performed under conditions recommended by the distributor (NEB). DNA fragments were ligated at 10 ng/µl total DNA (mole ratio of insert to backbone was higher than 3) with T4 DNA ligase either at 24°C for three hours or at 16°C overnight.

11.7 Site directed mutagenesis

Site-directed mutagenesis (SDM) was described before (Zheng *et al.*, 2004). Briefly, a PCR using Phusion DNA polymerase was performed. 50 ng of template plasmid was amplified with complementary mutagenesis primers for 16 cycles with 1 min/kb elongation time in a total volume of 50 ml. Methylated template DNA was hydrolyzed for one hour at 37°C by the addition of 10 U *Dpn*I. Finally, 1 ml of the reaction was transformed into *E. coli*.

11.8 Golden-gate cloning

Golden-gate cloning was used to combine several DNA fragments through designed complementary sticky ends in a defined order (**Figure 7**). Short base overhang (4 bp) and were added to the 5' end of the forward primer used to replicate the DNA fragment 2; the complementary sequences of the short overhang are reversely added to the front of the reverse

primer of the DNA fragment 1 so that the end of the DNA fragment 1 was connected to the DNA fragment 2. It is analogized to subsequent gene fragments. The designed short overhangs (in forwarding primers) were *ACTA* (blue), *CCGA* (red), *GGAG* (green), *TTCG* (purple), and *AATG* (orange). A *BsaI* site was added upstream of each primer for the generation of sticky ends of amplified DNA fragments.

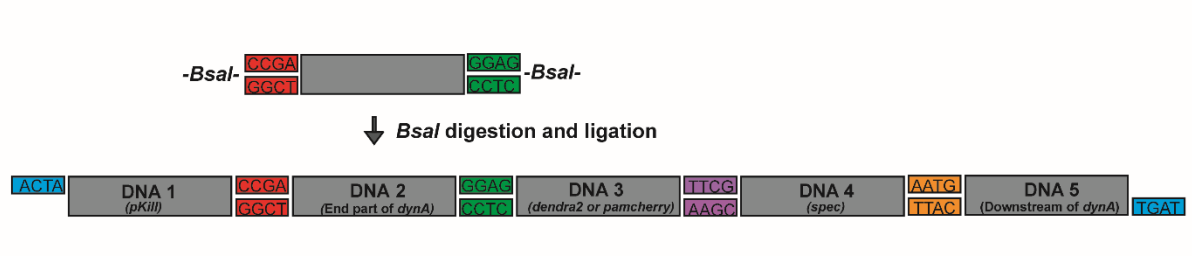

Figure 7. Cartoon illustration of the principle of golden-gate cloning.

12 Biochemical methods

12.1 Protein purification

DynA, $DynA_{K56A/K625A}$, DynA subunit D1 (residues 1-609), and D2 (residues 561-1193) were isolated as previously described (Burmann *et al.*, 2011) with a modification that the lysis buffer of the D1 subunit contained 200 mM NaCl. These proteins were isolated by metal affinity purification (Ni-NTA agarose, Qiagen, Düren, Germany) and a size exclusion chromatography on the increase superose 6 column (GE Healthcare, Uppsala, Sweden) was performed using T5 buffer.

12.2 Protein quantification

Protein concentrations were estimated using the colorimetric bicinchoninic acid (BCA) assay kit purchased from Thermo scientific, according to the manufacturers provided.

12.3 Protein concentration

Protein was concentrated by centrifugation at 4000 g in Amicon concentrator tubes (Millipore). Full-length DynA was concentrated in MWCO 100 KDa filters. For D1 and D2 subunits, MWCO 50 KDa filters were used. The solutions were mixed repeatedly by tube inversions during the concentration process.

12.4 Polyacrylamide gel electrophoresis

Polyacrylamide gel electrophoresis (SDS-PAGE) was performed with resolving gels of 7% acrylamide/bisacrylamide (37.5:1) and stacking gels of 4%. Samples were prepared by the addition of 4X loading buffer and heating for 5 min at 95°C when required. The electrophoresis was carried out in 1X SDS-PAGE running buffer in a BioRad Mini-PROTEAN chamber at 90V for stacking gel and 140V for resolving gel. One gel was stained with Coomassie Brilliant Blue for an hour, followed by de-staining around 2 hours in the destaining buffer until the bands were visible against a transparent background. Protein size was determined with Thermo Scientific PageRuler prestained protein ladder.

12.5 Immunoblotting

Samples were separated on an SDS-PAGE gel and blotted onto a PVDF transfer membrane for 2 hours at 100 mA or overnight at 20 mA. Blots were blocked for at least one hour in blocking buffer (5% Milk powder in immunoblotting washing buffer). The blot was incubated with primary antibody (anti-Dendra2, 1:2.000, anti-His, 1:2000) diluted in blocking buffer at room temperature for at least 1 hour. The blot was then washed four times with immunoblotting washing buffer and incubated with the secondary antibody (anti-rabbit conjugated with alkaline phosphatase, 1:10000, anti-mouse conjugated with alkaline phosphatase, 1:10000) at room temperature for at least 1 hour. The blot was again washed four times with washing buffer. Detection was visualized by incubation with Nitro blue tetrazolium chloride (NBT)/ 5-Bromo-4-chloro-3- indolyl phosphate (BCIP). For this, 10 ml of phosphatase buffer 100 mM NaCl, 100 mM Tris, 5 mM $MgCl_2$, pH 9.5) was mixed with 60 µl NBT and 100 µl BCIP and placed on the gel.

12.6 GTPase activity test by high-performance liquid chromatography (HPLC)

GTP hydrolysis was assessed using HPLC with a hydrophobic C18 column (Chromolith Performance HPLC column 100-4.6 mm) in 10 mM tetrabutylammonium bromide, 0.2 mM sodium azide, 100 mM potassium phosphate pH 6.5, and 2% acetonitrile. Hydrolysis reactions contained 1 mM nucleotide, 50 mM Tris/HCl, 200 mM NaCl, 5 mM $MgSO_4$ and 2.5 µM protein. GDP and GTP amounts were detected at 254 nm and 285 nm wavelengths in a total volume of 100 µl. The sample was incubated at 37°C for 15 min and filtered before injection onto the column. The chromatogram was analyzed with OriginPro 8.0 software.

12.7 Lipid binding and tethering assays

E. coli total lipids were obtained from Avanti Polar Lipids (USA). The *E. coli* total lipids were evaporated under a stream of nitrogen and further dried completely under vacuum. The lipids were then diluted to 1 mg/ml in T5 buffer, vortexed vigorously to get a homogenous solution and then extruded 20 times through a millipore filter with 0.4 μm pore size. Liposomes were used directly after preparation. Premade liposomes were mixed with protein and incubated at 37℃ for 30 min. Then liposomes were concentrated by ultra-centrifugation with 80,000 g, 20 min. SDS-PAGE tested the separated pellet. Liposome tethering was observed at 24℃ by sample turbidity changes at 350 nm measured in an Infinite200 PRO (Tecan, Grödig, Austria) fluorescent plate reader.

12.8 Lipid mixing assay

Before liposome formation, fluorescent lipids were mixed into *E. coli* total lipids or phospholipids to allow assays of lipid FRET and lipid dequenching. Concentrations of fluorescent lipids and proportions of phospholipids are indicated in the figure legends of the respective experiments. The lipids were evaporated under a stream of nitrogen and further dried completely under vacuum. The lipids were then diluted to T5 buffer, vortexed vigorously to get a homogenous solution and subsequently extruded 20 times through a millipore filter of pore size 0.4 μm. Liposomes were used directly after preparation. Liposome fusion was assayed at 37℃ or 24℃. Fusion reactions of 200 μl were assembled from three pre-mixes: one mix of liposomes in H1.5 buffer, one mix containing GTP in H1.5 buffer, and one mix of proteins in T5 buffer or H1.5 buffer. All components were incubated directly in 96-well plates, for up to 24 h and lipid mixing signals were recorded at intervals of 1min or 5min in an Infinite200 PRO (Tecan, Grödig, Austria) fluorescent plate reader (MB:: NBD-FRET Ex: 370 nm; Em: 538 nm; MB dequenching, Ex: 370 nm; Em: 465 nm). For lipid dequenching reactions, maximal values were estimated after the addition of 0.1% (wt/vol) thesit to the samples. FRET efficiency *E* defined as $E = f_{D_{ex}}^{A_{em}} \Big/ \left(f_{D_{ex}}^{D_{em}} + f_{D_{ex}}^{A_{em}} \right)$ where $f_{D_{ex}}^{D_{em}}$ represents the donor emission intensity after donor excitation and $f_{D_{ex}}^{A_{em}}$ the acceptor emission intensity after donor excitation.

12.9 Content mixing assay

The *E. coli* total lipids were evaporated under a stream of nitrogen and further dried completely under vacuum. The dried lipids were diluted to 2 mg/ml in H1.5 buffer with 0.1% NaN_3 (wt/vol).

Additionally, either of two luminal markers, Bo-PhycoE (0.4 µM) or Sa-Cy5 (0.4 µM), was added in lipid solutions before extrusion. Solutions were extruded 30 times through a millipore filter of pore size 0.4 µm and then dialyzed in 1000 kDa tubing (Spectrumlabs, Rancho Dominguez, CA, USA) for the Bo-PhycoE vesicles and in 300 kDa tubing (Spectrumlabs, Rancho Dominguez, CA, USA) for the Sa-Cy5 vesicles three times (6 h, 12 h, 12 h) against 1000-fold volumes of RB150/Mg^{2+}/NaN_3 to remove non-entrapped probes. To improve liposome quality, excess Biotin was removed by using streptavidin magnetic beads (GE Healthcare, Uppsala, Sweden), and the incubation spent 30 min. Similarly, the streptavidin labeled vesicles were further cleaned with magnetic biotin beads from Raybiotech (Norcross, GA, USA) to remove unbound dye. The incubation time with magnetic beads was prolonged until no free label was observable by fluorescence microscopy. Vesicles with labeled content were kept at 4°C during the preparation. Liposome content fusion was assayed at 37℃ or 24℃. Fusion reactions of 200 µl were assembled from three pre-mixes: one mix of liposomes in H1.5 buffer, one mix of GTP in H1.5 buffer, and one mix of proteins in T5 buffer or H1.5 buffer. All components were incubated directly in 96-well plates, incubated for up to 24 h and content and lipid mixing signals were recorded at intervals of 1 min or 5 min in an Infinite200 PRO (Tecan, Grödig, Austria) fluorescent plate reader (PhycoE::Cy5-FRET, Ex: 496 nm; Em: 670 nm). For content mixing, maximal values were estimated after the addition of 0.1% (wt/vol) thesit to the samples. FRET efficiency *E* defined as $E = f_{D_{ex}}^{A_{em}} \Big/ \left(f_{D_{ex}}^{D_{em}} + f_{D_{ex}}^{A_{em}} \right)$ where $f_{D_{ex}}^{D_{em}}$ represents the donor emission intensity after donor excitation and $f_{D_{ex}}^{A_{em}}$ the acceptor emission intensity after donor excitation. For combination analysis of lipid dequenching and content mixing, the excitation wavelength of PhycoE::Cy5-FRET changed to 535 nm.

12.10 Nisin staining

Nisin solution (500 µl, 30 mg/ml in H_2O) was mixed with 5 µl Alexa Fluor 647 (Succinimidyl Ester, 1mg/ml in DMSO) and rotated for 1 hour in room temperature. An illustra NAP-5 column was used to separate stained nisin from the free dye. The column was equilibrated with 10 ml sterilized H_2O, and then the stained nisin solution was loaded. Every drop (~ 50 µl) was collected in 200 µl PCR tubes, and fluorescence intensity was tested in an Infinite200 PRO (Tecan, Grödig, Austria) fluorescent plate reader. To test for nisin activity, 2 µl of labeled nisin were added to 198 µl fresh bacterial liquid (OD = 0.5) in a 96-transparent plate and measured their absorbance intensity changes at 600 nm in 30 min. Labeled nisin was stored in the dark at -20°C.

12.11 Lipoteichoic acid assay

B. subtilis 168 and *dagK*-knockout strains were used for lipoteichoic acid and wall teichoic acid assay. For the wall teichoic acid extraction, peptidoglycan capsules were first isolated and then hydrolyzed with trichloroacetic acid and sodium hydroxide. Lipoteichoic acids were extracted with 1-butanol and pretreated with lipase (Resinase) to deacetylate the diacylglycerol anchor preventing aggregation and improve single-band resolution by PAGE. Alcian blue- silver staining then observed the extracted teichoic acids according to a previous publication (Kho & Meredith, 2018).

13 Microscopy

13.1 Fluorescence microscopy

For visualizing fluorescent-labeled vesicles, bacterial cells, and bacteriophage particles, a Delta Vision Elite (GE Healthcare) equipped with an Insight SSI™ illumination, and a CoolSnap HQ2 CCD camera was used. A loop-ful of freshly plated or 100 µl overnight cultured *B. subtilis* cells were used to inoculate 10 ml MD or LB medium and grown up to OD = 0.5 to 1.0. For xylose-induced strains, cells were induced with 0.1% xylose at OD = 0.5. After 60 minutes of induction, 2 µl of the cell culture was placed on an agarose bed on a glass slide, covered with a glass slip, and observed with light microscopy. For Dendra2 photo-conversion and PAmcherry photo-activation. A 405 nm laser was used at 20% power, and the pulse duration was 0.02 seconds. Images were taken every second for a total of 60 seconds. Fluorescence-labeled ϕ29 were mixed with *B. subtilis* cells at MOI = 1 when required. Microscopy slides with reaction wells and black masks were used for visualizing vesicles. Images were taken with a 100× oil PSF U-Plan S-Apo 1.4 NA objective. A four-color standard set InsightSSI unit with the following excitation wavelengths (blue 390/18 nm, green 475/28, orange 542/27, far-red 632/22 nm); single bandpass emission wavelengths (blue 435/48 nm, green 573/36, orange 594/45, far-red 679/34 nm) and a suitable poly-chromic for Blue/Green/Orange/Far-Red were used. ImageJ was used to layout microscopic graphs and measure vesicles' size in the graphs.

13.2 Electron microscopy

The purification of DynA was as described above, but the UV peak of the protein was between 50 and 500 mAU in the step of gel-filtration chromatography. Freshly purified DynA was placed on the grid covered with carbon and negatively stained with Uranyl acetate (UAc).

Before staining, grids covered with carbon were hydrophilized in the plasma cleaner for 30 sec, and different dilutions of purified protein solution were prepared. 3 - 5 µl of the dilution were pipetted onto the grid fixated with tweezers, and the adsorption spent for 60 sec. A piece of filter paper was used to blot away the fluid, and the sample should not dry out completely. The grid was washed immediately with 3 µl UAc (2%), and the fluid was blotted away from the side with a filter paper without completely dry. 3 µl UAc (2%) was added to the grid again and held for 30 sec, and then the fluid was blotted away from the bottom side until it was scorched. Prepared grids with a stained sample were stored in a grid box until imaging. For visualizing the single particles stained on the grid, a JOEL JEM 2100F (200 kv) microscope was used. The estimated amount of astigmatism was set about 500-1000 Å for this microscope. The micrographs were analyzed in the software of Relion and Cryosparc by a general workflow of a typical negative staining structure data processing. The typical workflow of single particle analysis is manual picking, 2D classification, auto-picking, 2D classification again, initial 3D model, 3D classification, and finally, 3D auto-refine.

Results

1 Characteristics of DynA-mediated membrane fusion *in vitro*

Membrane fusion can be separated in various distinct steps: membrane tethering in trans (docking), the formation of hemifusion stalk (hemifusion), and fusion pore expansion to the point at which the vesicle membrane flattens on the membrane interaction surface, leading to the release of the luminal contents (full fusion) (Südhof & Rothman, 2009, Chernomordik & Kozlov, 2005, Accola *et al.*, 2002). Docking of membranes is not sufficient for lipid exchange. Hemifusion is the intermediate stage for membrane full fusion that allows the interaction of lipids between the outer leaflets. In contrast, lipid exchange between inner layers and content mixing is still blocked. Membrane full fusion results in the unification of the lipid bilayer and the intermixing of the volumes. To test DynA-mediated membrane fusion, we employed assays based on fluorescence resonance energy transfer (FRET) (**Figure 8**). Specifically, we used lipid tethering assay to detect docking of vesicles and two lipid mixing assays to detect lipid exchange in stages of hemifusion and full fusion, termed lipid FRET and lipid dequenching as described before (Zick & Wickner, 2014). In lipid tethering assay, docking of vesicles induced by protein could increase turbidity value measured at 350 nm (Burmann *et al.*, 2011). For lipid FRET assay, liposomes were prepared with fluorescent lipids MB-PE or NBD-PE, respectively. For lipid dequenching assay, one set of vesicles is pre-formed with MB-PE and NBD-PE, while the other vesicles have no fluorescent lipids. One limitation of the lipid mixing assays is that it does not directly discriminate between stages of hemifusion and full fusion. Therefore, a

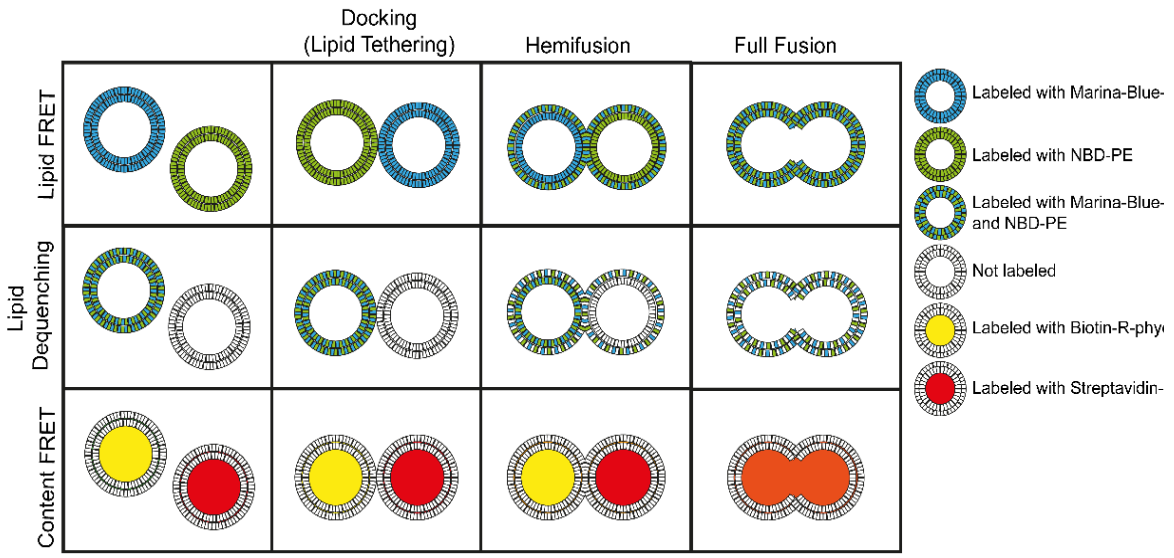

Figure 8. **Cartoon of vesicle fusion assays used here to study DynA-mediated membrane fusion.**

content mixing assay (termed content FRET here) was used to directly test the exchange of content, addressing whether DynA or DynA plus GTP can lead to complete membrane fusion (Zucchi & Zick, 2011). Bo-PhycoE and Sa-Cy5 were used as luminal reporters in content mixing assay.

1.1 DynA induces membrane full fusion *in vitro*

DynA displayed nucleotide-independent membrane binding and tethering (Burmann *et al.*, 2011). Here, we further tested the ability of DynA in membrane fusion using FRET-based lipid and content mixing assay. DynA was purified as described before (**Figure 9A**) and retained GTP hydrolysis activity (**Figure 9B**). HPLC analysis also proved that DynA was purified without GTP contamination (**Figure 9B**). Another prerequisite was that the designed membrane vesicles were properly synthesized and remained stable (**Figure 10Aa**, **b**, **h,** and **i**). Marina Blue-PE (MB-PE), NBD-PE, Biotin-R-phycoerythrin (Bo-PhycoE), and Streptavidin-Cy5 (Sa-Cy5) labeled vesicles were observed with fluorescence microscopy. When the two species of vesicles were mixed, the fluorescence signals were correctly separated both for lipid FRET and content FRET assays (**Figure 10Ac** and **10Aj**), ruling out that spontaneous fusion occurs in the time course of the experiments. After the addition of DynA, membrane vesicles aggregated to form large membrane clusters (**Figure 10Ad** and **10Ak**). These clusters revealed green and blue fluorescence when vesicles for lipid FRET were mixed. Simultaneously, clusters for content FRET assay showed orange and far-red fluorescence, indicating that lipid and content exchange can occur after DynA addition. The addition of 1mM GTP gave essentially the same result (**Figure 10Ae** and **10Al**). In the protein-containing samples, occasionally large, unilamellar vesicles (white arrow, diameter: 8.92 μm) appeared in lipid FRET assays (**Figure 10Af**). Similarly, large vesicles (white arrow, diameter: 2.43 μm) were also observed in content FRET assay (**Figure 10Am**), suggesting that DynA promoted the fusion of multiple liposomes into large vesicles. In other words, DynA catalyzed full fusion of membrane vesicles *in vitro*. Additionally, we added Proteinase K to the protein-containing samples and incubated for ten minutes. Proteinase treatment led to the separation of membrane clusters into individual vesicles (**Figure 10Ag** and **10An**). These vesicles (white arrows, 1.36 μm in **Figure 10Ag,** and 2.26 μm in **Figure 10An**) were more extensive than the newly prepared liposomes (~ 0.4 μm).

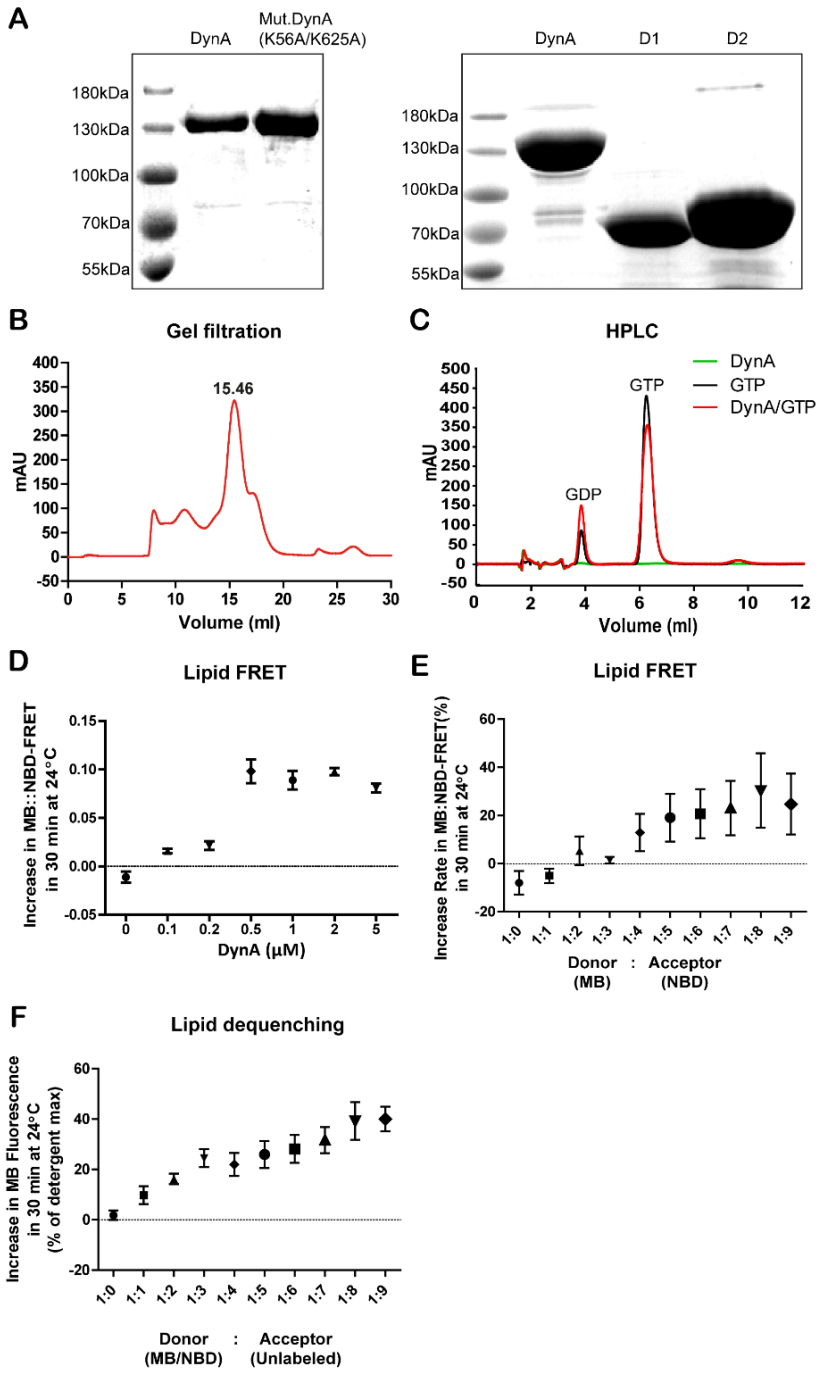

Figure 9. **Purification of DynA and its lipid mixing tests.** (A) Purified wild-type DynA, mutated DynA (K56A and K625A), D1 subunit and D2 subunit showed by SDS-Page. (B) Chromatographic performance of DynA in gel filtration after Ni-NTA agarose purification. The protein used in membrane fusion assays was from the peak at 15 ml. (C) One-micromolar DynA was incubated for 20 min at 37°C in presence of 1mM GTP and 5 mM MgSO4 with controls of only GTP and only protein, then run the samples in a Chromolith Performance RP-C18E column with a flow rate of 4 ml/min. In the HPLC plot, the first peak represented GDP and the second is GTP. (D) Optimization of DynA concentration in lipid FRET assay. DynA concentrations of 0.5 µM were found to be optimal for fusion assays. The mean and SEM of 5 replicates are shown. (E) Lipid-FRET efficiency comparison at ratios of donor and acceptor vesicles. Amount of MB-labeled vesicles is always 10 µl, while NBD is from 0 to 90 µl in a 200 µl system. Mean and SEM of 3 replicates are shown. (F) Lipid dequenching efficiency comparison upon ratios of donor and acceptor vesicles. The amount of MB/NBD-labeled vesicles in 200 µl reaction system is always 10 µl, while unlabeled vesicles are from 0 to 90 µl. Mean

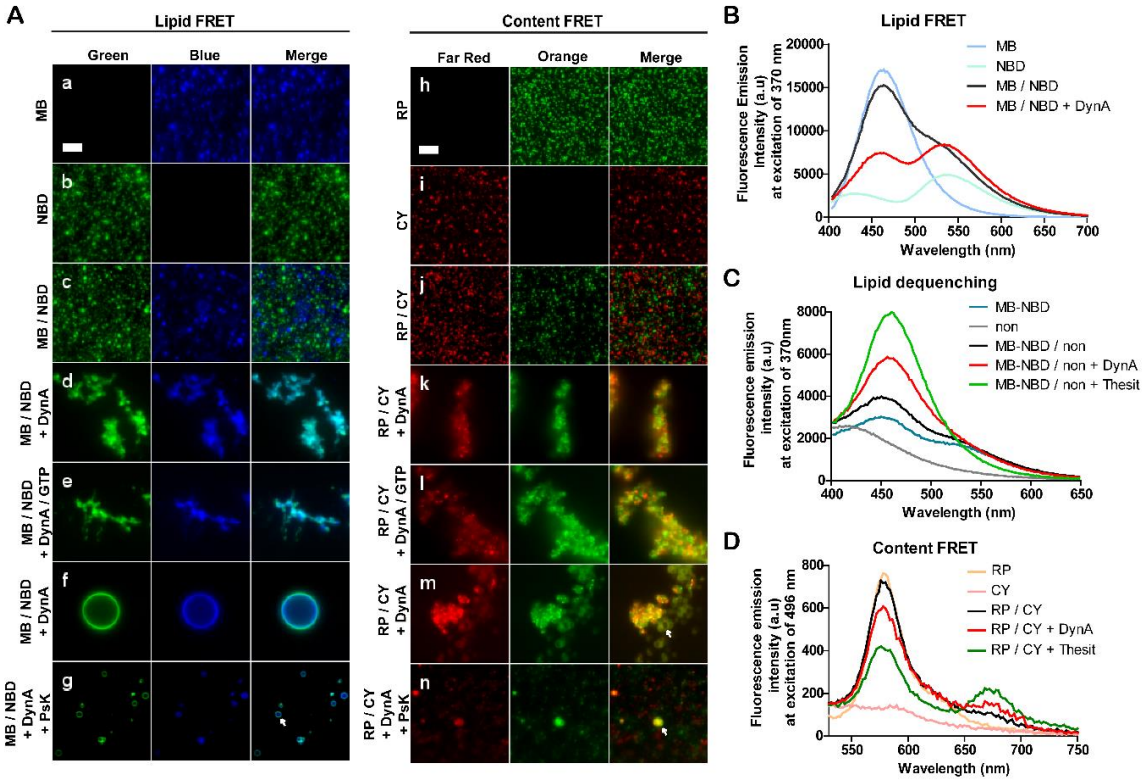

Figure 10. DynA mediates lipid mixing and content mixing in the absence of GTP. (A) Microscopic observation of DynA mediated vesicle fusion in lipid FRET and content FRET assays (37°C; Scale: 5 µm). (a) In lipid FRET assay, donor vesicles were labeled with MB-PE (MB, 1 mol%), exhibiting a blue fluorescence signal, (h) donor vesicles for content FRET assay were labeled with Bo-PhycoE (RP, 0.4 µM) in their lumen, exhibiting an orange fluorescence signal. (b) NBD-PE (NBD, 1 mol%) labeled vesicles, serving as receptors in lipid FRET assay, exhibited a green fluorescent signal and (i) Sa-Cy5 (CY, 0.4 µM) labeled vesicles, serving as receptors in content FRET showed far-red fluorescence. (c, j) After mixing the two species of vesicles (MB/NBD or RP/CY) no fluorescent overlapping was observed. (d, k) Purified protein DynA (0.5 µM) was added and incubated for 1h. (e, l) Vesicle fusion in presence of 1 mM GTP. Note that in experiments with and without nucleotide large membrane clusters were observed. (f, m) Examples of large unilamellar vesicles both in lipid FRET and content FRET assays. (g, n) After proteinase K treatment (10 min) of the protein-containing samples, membrane clusters disengaged and larger sized membrane vesicles appeared compared with non-protein samples. (B) Fluorescence emission intensity in lipid FRET assay at the excitation of 370 nm with a ratio of MB and NBD vesicles of 1:9. Protein amount is 0.5 µM. Incubation temperature is 37°C. (C) Fluorescence emission intensity in lipid dequenching assay at the excitation of 370 nm with a ratio of MB-NBD and non-labeled vesicles (no fluorescent lipids) of 1:9. Protein amount is 0.5 µM. Incubation temperature is 37°C. (D) Fluorescence emission intensity in content FRET assay at the excitation of 496 nm with a ratio of RP and CY vesicles of 1:9. Protein amount is 0.5 µM. Incubation temperature is 37°C.

Fluorescence microscopy indicated that DynA is able to induce lipid and content mixing. However, visual observation does not allow any quantitative measurement. Therefore, we performed lipid FRET, lipid dequenching, and content FRET experiments. We first determined the optimal protein concentrations for lipid mixing to be 0.5 µM (**Figure 9D**). Additionally, optimization of lipid mixing efficiencies revealed that in the lipid FRET assay, a nine-fold excess of FRET receptor vesicles (labeled with NBD) over donor vesicles (labeled with MB) resulted in optimal MB::NBD-FRET efficiencies (**Figure 9E**). This result was the same in lipid dequencing assay, where we found a nine-fold excess of receptor vesicles (non-labeled) over donor vesicles (labeled with MB and NBD) yielded higher lipid dequenching efficiency (**Figure 9F**). Using optimized conditions, we analyzed the influence of DynA on lipid mixing. DynA caused a significant increase in lipid FRET efficiency (**Figure 10B**), similar to the observation we made earlier. Lipid dequencing assays using a mixture of MB-NBD-labeled liposomes and non-labeled liposomes gave essentially the same results (**Figure 10C**). We used the addition of the detergent thesit as a control for theoretical maximal fusion. We next wanted to analyze the ability of DynA to catalyze full membrane fusion. Therefore, we used a content FRET assay with liposomes filled with R-phycoE and Cy5, respectively (for details, see material and methods). Optimized conditions were 0.5 µM protein and a ratio of donor and acceptor vesicles of 1:9. The addition of thesit served again as the control for FRET efficiency. Emission increase at 670 nm indicates FRET when both dyes mix after membrane fusion. DynA was able to promote full fusion and hence content mixing in this setup (**Figure 10D**).

Residues R512 and R517 of DynA are not lipid-binding sites. Previous work from our laboratory tried to identify the lipid-binding sites of DynA. The point mutations of R512A-DynA and R517A-DynA were thought to be part of the membrane-binding site. Here, the two sites were mutated simultaneously, and then the mutant protein (R512A-R517A-DynA) was purified and tested for its membrane binding capacity *in vitro* by membrane binding assay. As shown in **Figure 11**, there is no significant difference in the membrane-binding ability of the double mutant protein and wild protein, and both can bind to membrane vesicles with or without ATP or GTP with no significant difference in the amount of binding in the absence or presence of ATP or GTP. The results of *in vivo* experiments were similar. The double mutant and fluorescent-labeled protein were still attached to the cell membrane as the wild-type (data not shown). These results indicate that R512 and R517 are not membrane binding sites of DynA, and the search for membrane binding sites needs further study.

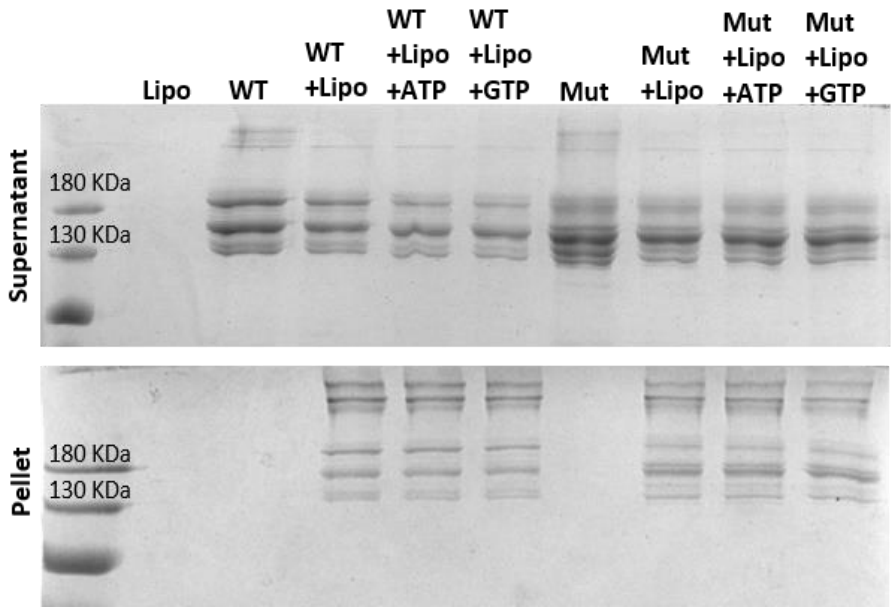

Figure 11. The determination of R512 and R517 of DynA as lipid binding sites. The purified wild type DynA (WT) and R512A-R517A-DynA (Mut) were mixed with extruded membrane vesicles and ultra-centrifuged, and then the proteins adhered to the centrifuged membrane vesicles were showed with SDS-Page.

YpbS has no role in membrane fusion. YpbS locates at the 3' end of *dynA* transcription and hence is a neigbouging gene. The ORF is 258 bp in length, and the molecular mass of the translated ypbS protein is 9.75 kDa. To determine whether YpbS is introduced in DynA mediated membrane fusion, YpbS was purified, then DynA and YpbS were used in lipid fusion assays. YpbS was first purified by Ni-NTA chromatography and then further purified by molecular size exclusion chromatography (**Figure 12**). YpbS monomer was eluted at 19 ml. After gel-filtration, the multimers of YpbS and some small molecular impurities were discharged (**Figure 12A** and **12B**). Lipid mixing assay was applied to explore the role of YpbS in the process of membrane fusion induced by DynA (**Figure 12C**). YpbS alone did not induce membrane fusion. DynA alone, significant membrane fusion occurred regardless of the presence of GTP. When DynA and YpbS were incubated simultaneously, we did not observe any considerable enhancement of membrane fusion than DynA alone (P = 0.7476 for DynA: DynA\YpbS). These results indicated that YpbS expressed by *dynA*'s genomic neighbor *ypbS* does not affect DynA-induced membrane fusion.

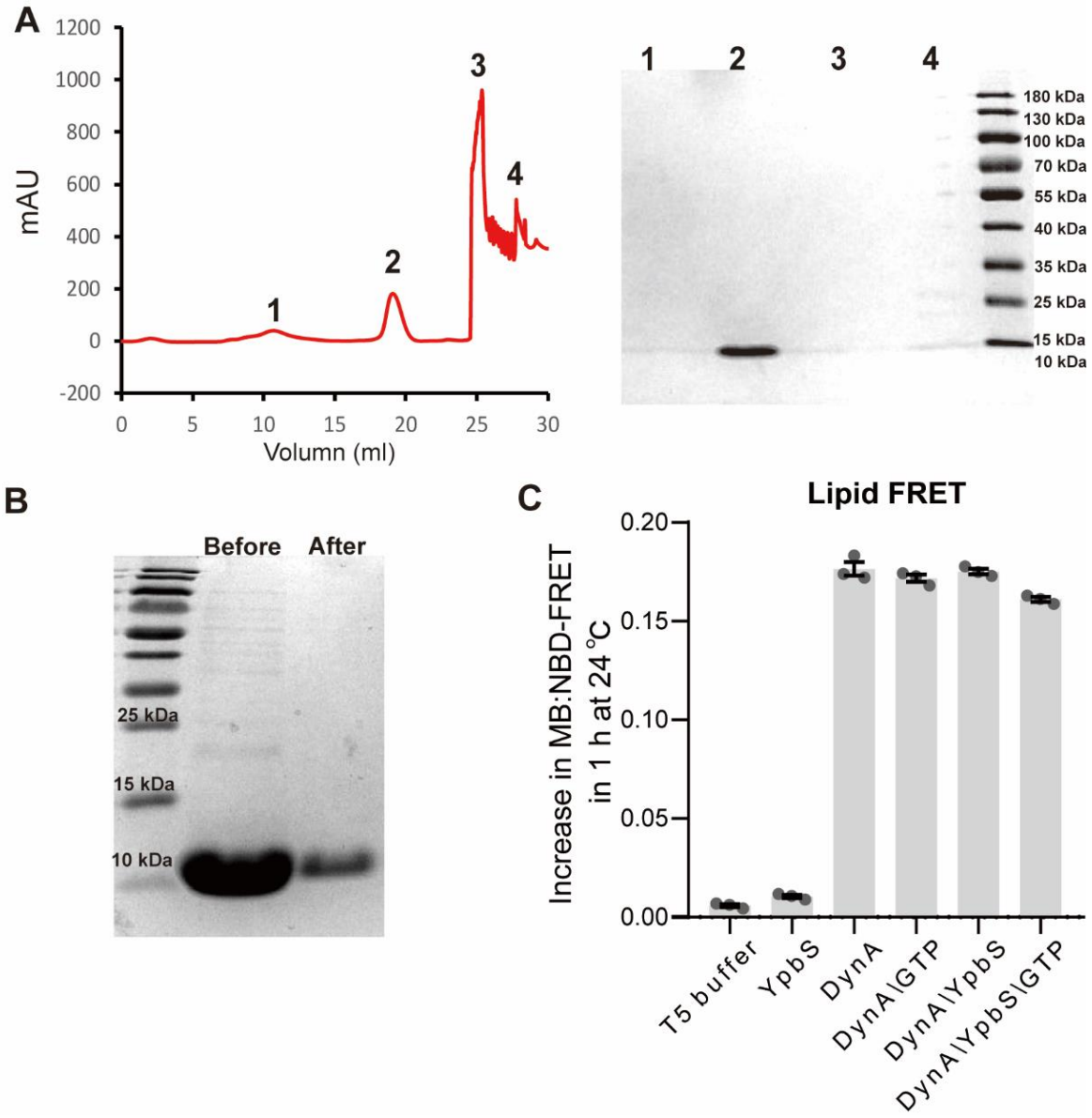

Figure 12. Purification and functional analysis of YpbS. (A) The samples corresponding to the four peaks on the gel-filtration spectrum of YpbS were collected and analysed by SDS-page. Peak 2 corresponds to the monomer of YpbS. (B) Comparison of protein purity before and after gel-filtration. It can be seen from the SDS-page gel that gel filtration has eliminated multimers. (C) YpbS does not induce membrane fusion, nor does it have a positive effect on membrane induced by DynA. GTP concentration was 1 mM. Protein amounts for YpbS and DynA was 0.5 µM. The changes in lipid-FRET efficiency within one hour after protein addition were measured at 24° C. The ratio between MB and NBD vesicles was 1:9. Mean and SEM of 3 replicates are shown.

1.2 The D1 subunit of DynA is crucial for membrane fusion, but cannot stabilize membrane cluster

The bacterial dynamin-like protein NosDLP homo-dimerizes in its GDP-bound state via its GTPase domain. In the presence of GTP and lipids, the protein self assembles around the liposome and forms a lipid tube (Low & Lowe, 2006). However, we have shown before that most bacterial dynamin-like proteins may act as hetero-oligomers since they are usually encoded as two copies in an operon or the two genes are fused in a head-to-tail fashion giving rise to a fusion protein with two dynamin-like subunits (Burmann *et al.*, 2011, Liu *et al.*, 2018, Bohuszewicz *et al.*, 2016). *B. subtilis* DynA is an internal fusion protein containing two BDLP subunits (Jilly *et al.*, 2018). Earlier work showed that membrane binding is achieved via the D1 part of DynA (Burmann *et al.*, 2011). We tested the membrane tethering process and membrane fusion efficiency of these two subunits and the full-length protein (**Figure 13**). The lipid tethering induced by full-length proteins (wild-type DynA and GTPase deficient mutant DynA [K56A and K625A]) reached a plateau after 5 min and was stable at this plateau for at least one hour (**Figure 13A**). Compared to full-length proteins, lipid tethering induced by the D1 subunit dropped rapidly after reaching the apex, indicating that tethering mediated by D1 alone is unstable and highly reversible. The observed decrease cannot be interpreted as sedimentation since glass-bottom plates were used, and measurements were performed with a plate reader vertically into the buffer column. In contrast, D2-mediate fusion steadily increased over time (**Figure 13A**).

We also tested the influence of GTP in the lipid tethering assays. The addition of a nucleotide to full-length DynA lead to a destabilization of tethering, indicating that GTP hydrolysis might lead to a removal of DynA from the membrane. To test this, we removed DynA in a separate experiment by adding proteinase K and saw a similar decrease in tethering judged by the decreased turbidity (**Figure 14**). The addition of GTP did not affect tethering induced by the D1 part, in line with earlier observations that the individual domains (D1 and D2) of DynA do not exhibit GTPase activity (Burmann *et al.*, 2011). Similarly, GTP does not affect the GTPase deficient mutant DynA (K56A and K625A). Somewhat surprising was the slight decrease in tethering activity observed for the D2 subunit. As expected, the isolated D2 domain does not bind to and tether membranes as efficient as the D1 subunit. Still, in comparison to an earlier analysis, we observe some membrane-binding activity of the D2 subunit. The low membrane-binding activity of the D2 subunit is in line with a recent observation described for the *C. jejuni* DLP2 (Liu *et al.*, 2018).

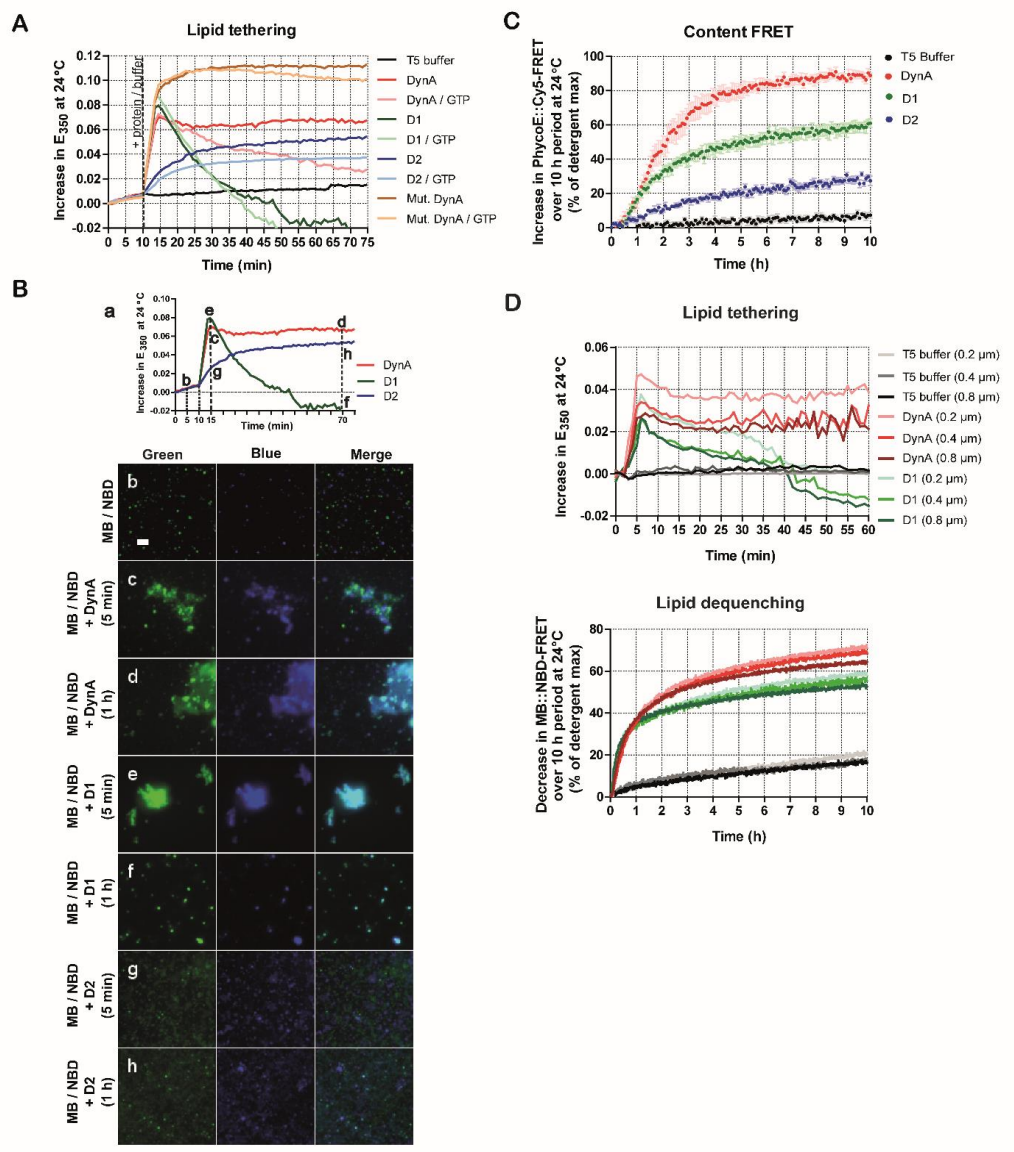

Figure 13. Isolated D1 and D2 subunits of DynA have reduced activity. (A) Lipid tethering in DynA, GTP inactive DynA (K56A and K625A), D1 subunit, and D2 at 24°C. Aggregations of liposomes in the presence of 0.5 µM full-length proteins and subunits are measured by turbidity change at 350 nm. Addition of 0.5 µM proteins was at 10 min. GTP concentration was 1 mM. (B) Microscopic observation of DynA and its subunits mediated lipid tethering at 24°C, corresponding to (A). Scale bar is 5 µm. (a) Samples were taken at these points during the reaction process (5 min before protein addition, 5 min after protein addition and 1h after protein addition) for fluorescent microscopy (b) Mixing of the two differently labeled vesicles did not result in fluorescent overlapping. (c, e, g) After addition of DynA/D1/D2 (0.5 µM) and incubation for 5 min at 24°C, DynA and D1 subunit could mediate the formation of large membrane clusters. (d, f, h) After addition of DynA/D1/D2 (0.5 µM) and incubation for 1 h at 24°C, membrane clusters induced by D1 subunit separated to single and double-colored vesicles. (C) Content mixing efficiencies of DynA, the D1 subunit and the D2 subunit over 10 h at 24°C. Protein amount is 0.5 µM. Error bars are SEM of 5 replicates. Each measurement interval is 5 min. (D) DynA and D1 subunit shows high curvature preference. Lipid dequenching efficiencies of DynA and D1-induced lipid tethering and lipid dequenching efficiencies for vesicles with diameters of 0.2, 0.4 and 0.8 µm at 24°C. Protein amount is 0.2 µM. The mean of the 3 replicates is shown. Each measurement interval is 1 min.

The observation of membrane tethering induced by DynA and its subunits was corroborated by fluorescent microscopy (**Figure 13Ba**). Before the proteins were added, the blue fluorescence of MB vesicles and the green fluorescence of NBD vesicles did not coincide after mixing (**Figure 13Bb**). Five minutes after the addition of full-length protein, mixed vesicles aggregated into large clusters (**Figure 13Bc**), and larger vesicles appeared after one hour (**Figure 13Bd**). For the D1 subunit, only large membrane clusters were observed after 5 min (**Figure 13Be**), and after 1 h, the membrane clusters separated in many double-colored single vesicles (**Figure 13Bf**). The addition of the D2 subunit did not lead to the formation of large membrane clusters. Still, some small flocculent cluster appeared (**Figure 13Bg**), the ratio of the double-colored cluster at 1 h was improved compared to that at 5 min (**Figure 13Bh**). These data indicate that D1 plays a key role in the lipid tethering necessary to induce membrane fusion, while D2 has an auxiliary role in maintaining membrane cluster stability.

In an approach to eliminate any experimental differences that might occur by using different liposome setups for tethering, lipid- and content mixing experiments, we designed an experiment series where we used the same liposomes for all three experiments. In the lipid tethering assay (**Figure 14B**), we measured the increase in turbidity caused by DynA and its subunits after mixing with vesicles for 5 min. DynA and D1 subunit exhibited a higher degree of tethering compared to data obtained with the D2 subunit ($P = 0.00030$ for DynA:D2, < 0.01; $P = 0.0014$ for D1:D2, < 0.01), whereas there was no significant difference between DynA and the D1 subunit ($P = 0.53$ for DynA:D1, > 0.05). The efficiency of DynA and the isolated D1 subunit in lipid mixing was similarly accelerating at the very beginning (**Figure 14B**). However, after 30 min, DynA-induced lipid mixing efficiency exceeded that of the D1 subunit. In the content FRET assay, content mixing efficiency induced by DynA was higher than that of the D1 subunit. The D2 subunit exhibited a slow increase of PhycoE::Cy5-FRET efficiency, but never reached value obtained with DynA or D1 subunit alone (**Figure 13C**). To further test if DynA promotes membrane leakage, we used an alternative assay to measure content mixing in the presence of an excess external competitor, which can rule out the effect of dye leakage (non-fluorescent streptavidin was added as a competitor to Cy5-conjugated streptavidin) (Zick & Wickner, 2014). Membrane vesicle rupture could cause Bo-PhycoE to efflux and bind to excess non-fluorescent streptavidin in liquid, rather than Sa-Cy5, preventing the occurrence of content FRET. In **figure 14C**, DynA significantly improved content mixing without including dye leakage, but this was slightly less efficient than the included case. It was shown that DynA could induce content exchange in vesicles, but it still caused a certain proportion of membrane penetration during DynA-induced membrane fusion. Besides, we tested the curvature

preference of full-length protein and D1 (**Figure 13D**). Both full-length protein and D1 exhibited higher membrane tethering and membrane fusion efficiency when vesicles had

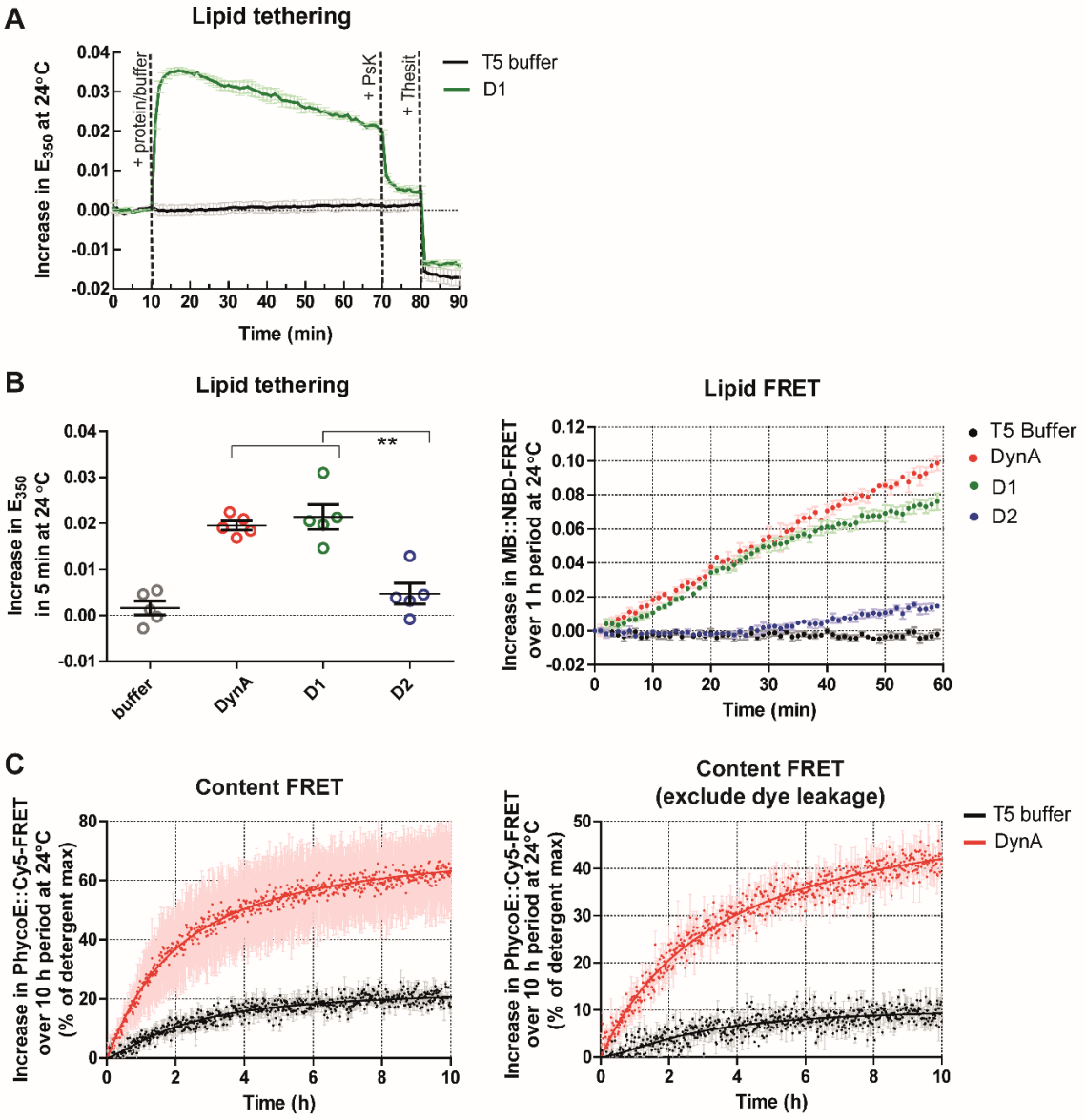

Figure 14. **Lipid analysis of DynA subunits and content leakage test.** (A)Lipid tethering analysis for D1 subunit at 24°C. A reaction system (200 µl) contains 20 µl liposome (1 mg/ml) and 0.5µM protein. Mean and SEM of 3 replicates are shown. Each measurement interval is 1 min. (B) Comparison between DynA and its subunits in lipid tethering and lipid mixing at 24°C. Protein amount is 0.5 µM. Error bars are SEM of 3 to 5 replicates. Two asterisks in lipid tethering assay mean that the *P* value of *t*-test is lower than 0.01. Each measurement interval in lipid mixing assay is 1 min. (C) Content FRET increase induced by DynA is mainly due to content exchange. Content mixing efficiencies of DynA in the presence and absence of non-fluorescent streptavidin over 10 h at 24°C. Protein amount

smaller diameters and higher curvatures, especially in membrane tethering, indicating high curvature preference of full-length protein and D1 subunit. However, no correlation was found between membrane curvature and the instability of D1-induced membrane tethering.

In summary, D1 subunit mediated membrane tethering (**Figure 13A** and **14B**), however tethering turned out to be unstable (**Figure 13A**). Therefore, the large membrane clusters caused by D1-induced tethering became invisible after one-hour incubation (**Figure 13Be** and **13Bf**). In contrast to the slow response of lipid mixing and content mixing induced by DynA and D1 subunit, the lipid tethering was able to reach a maximum within 5 min (**Figure 13A**) measured by turbidity change at 350 nm, suggesting that the docking process of vesicles mediated by DynA and D1 subunit was instantaneous. Still, the transition from docking to hemifusion was slow. The data in **Figure 13C** showed the membrane full fusion induced by full-length protein was significantly higher than that of the D1 subunit when their maximum of lipid tethering and lipid mixing efficiency in a short time were similar, suggesting that the D2 subunit played a role in facilitating membrane fusion. Finally, full-length protein and D1 subunit showed a high curvature preference (**Figure 13D**).

1.3 DynA-induced membrane fusion *in vitro* is a thermo-promoted slow response

To verify whether GTP hydrolysis powers the hemifusion-through-fusion pathway, we simultaneously applied content mixing and lipid dequenching assays, using vesicles labeled simultaneously for lipid and content mixing. The donor vesicles were labeled with MB-PE and NBD-PE and contained Bo-PhycoE within their lumen, while the receptor vesicles did not contain FRET-label in their membrane, but had Sa-Cy5 in the lumen. Using fluorescence microscopy, donor vesicles displayed fluorescent signals in three channels, green, blue, and orange (**Figure 15Aa**) as expected. At the same time, the receptors only had far-red signals (**Figure 15Ab**). After donor and acceptor mixing, content fluorescence signals did not overlap (**Figure 15Ac**), indicating that the prepared membrane vesicles were sufficiently pure and stable to meet the experimental requirements of subsequent lipid dequenching and content mixing in a combined assay. Larger PhycoE-MB-NBD vesicles (**Figure 15Aa** and **15Ac**, white arrows) exhibited stronger lipid fluorescence signals and had weaker content signals. We believe that the bigger the vesicle, the weaker the content fluorescence intensity due to the leakage during the fusion process and the low stability of larger vesicles. When we incubated DynA at 37°C with the prepared vesicles mix, we observed no difference in lipid dequenching and content FRET efficiency within 5-hour in the presence or absence of GTP (**Figure 16A**). Similarly, the addition of GTP to content FRET experiments did not result in different content mixing (**Figure 16A**). The results indicate that GTP hydrolysis neither affected DynA-induced lipid mixing and content mixing at 37°C nor affected the process from hemifusion to full fusion. However, content mixing reached a maximum at about 4 hours, and lipid dequenching reached

a maximum at about one hour, suggesting that DynA-induced content mixing significantly lagged behind lipid mixing (**Figure 16A**). We further tested the possibility that an overall high DynA concentration may mask a GTP effect. We used lower protein concentrations (100 nM,

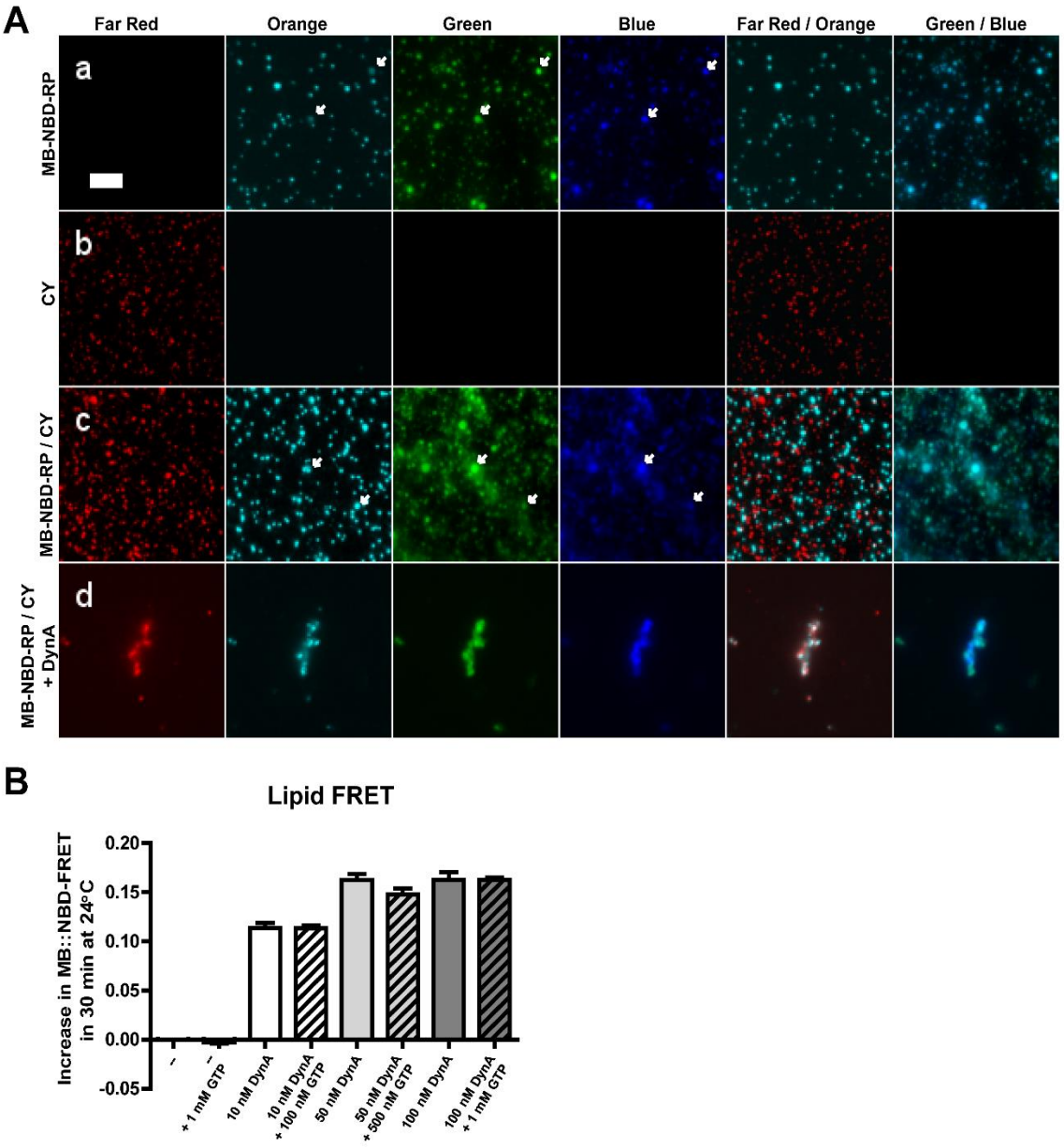

Figure 15. **Microscopic analysis of DynA effects on fluorescently labeled vesicles and lipid mixing analysis of low DynA protein concentrations.** (A) Microscopic analysis of DynA effects on membrane and content labeled vesicles. The donor vesicles were labeled with MB-PE and NBD-PE, and contained Bo-PhycoE within their lumen(a), while the receptor vesicles did not contain FRET-label in the membrane, but contained Sa-Cy5 in the lumen(b). After addition of DynA, vesicles aggregated into clusters with fluorescent signals in all four channels (c,d). (B) GTP had no obvious effect on lipid mixing in 30 min when low DynA protein concentrations (100 nM, 50 nM, and 10 nM) were used. Nucleotide concentration was always 2000-fold excess (200 µM, 100 µM, 20 µM) over protein concentration to minimize inhibitory effects of large nucleotide excess.

50 nM, and 10 nM). We found that adding GTP to mixtures with low protein concentrations did not improve the efficiency of membrane fusion (**Figure 15B**). Interestingly, we found that the short-term treatment with Proteinase K led to an instant increase in content mixing (P = 0.00021, < 0.001) (**Figure 16B**). A simple explanation for this observation is that sudden DynA detachment from the membrane surface is a driving force for the transition from hemifusion to full fusion.

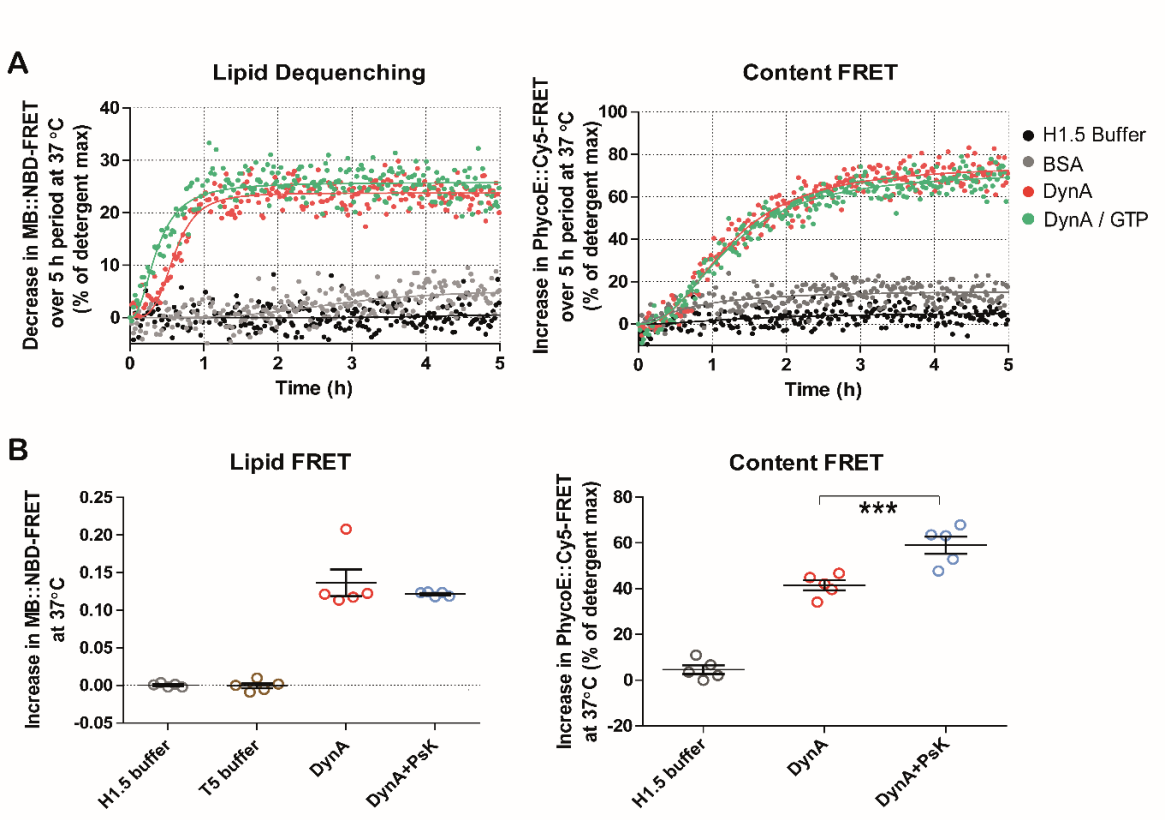

Figure 16. **DynA acts via fusion-through-hemifusion pathway.** (A) Combination analysis of lipid dequenching and content mixing. Changes in lipid dequenching efficiency and content FRET efficiency over a continuous 24 h period at 37°C. The ratio of donor vesicles (MB/NBD/RP) and receptor vesicles (CY) was 1: 9. GTP concentration was 1 mM. Protein amount was 0.5 µM. Each measurement interval was 1 min. Shown is the mean of the 5 replicates. (B) Changes in lipid-FRET and content-FRET efficiency after addition of DynA and proteinase K at 37°C. Columns of DynA are 70 min incubation of protein (0.5 µM), while DynA/PsK columns are 60 min incubation of protein plus 10 min treatment of proteinase K (30 µg/ml). Error bars are SEM of 5 replicates. Three asterisks indicate that the P value of t-test is lower than 0.001.

We next wanted to test the influence of temperature on the lipid mixing activity of DynA. Therefore, we compared lipid and content mixing at 37°C and 24°C (**Figure 17).** Lipid FRET experiments performed at 37°C reveal that the fast and initial lipid mixing, catalyzed by DynA,

is not affected by GTP (**Figure 17A**). However, after 5-hour incubation, the FRET signal in the reaction lacking GTP decreased, compared to the sample with nucleotide (**Figure 17A**). In

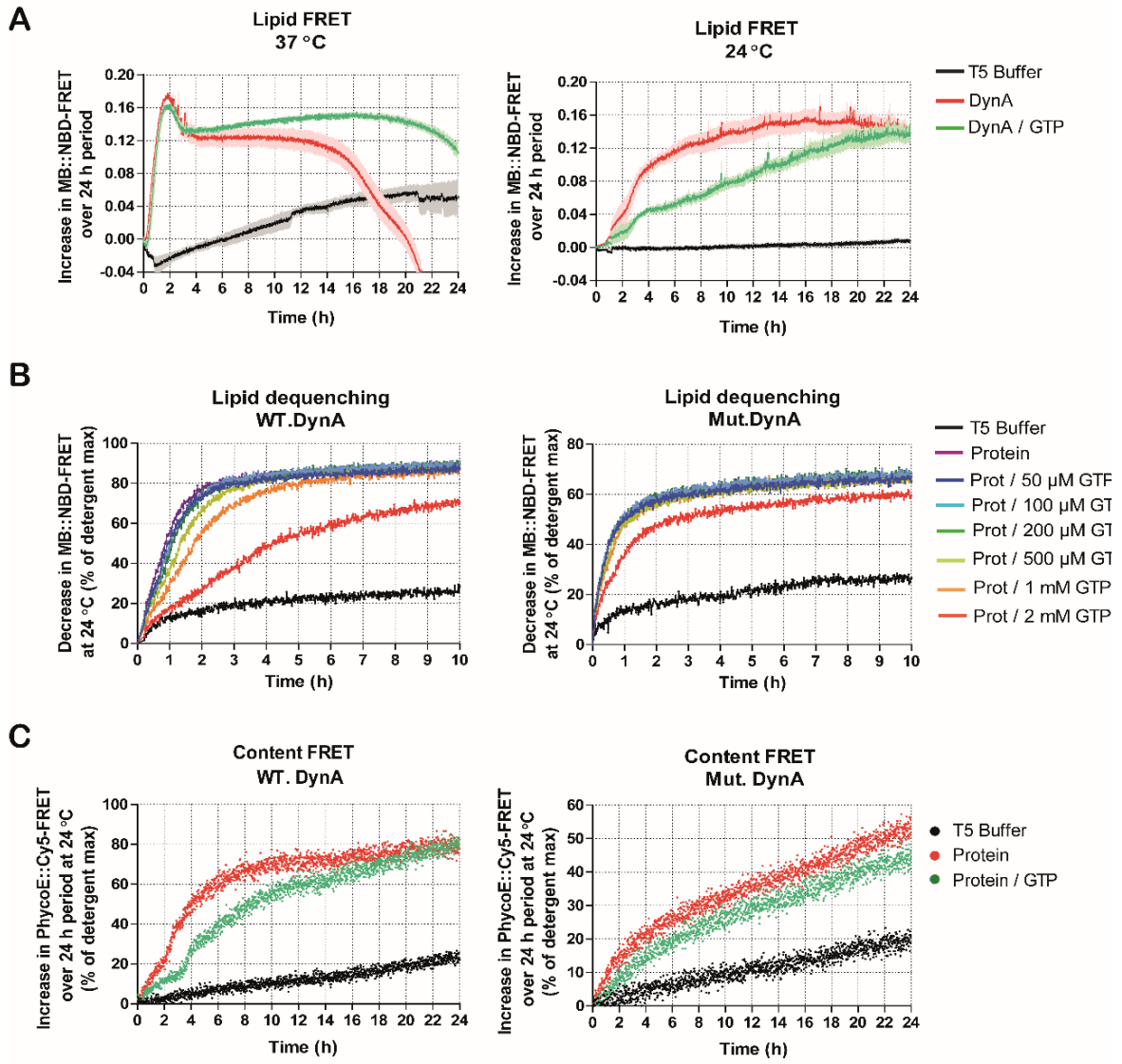

Figure 17. GTP hydrolysis reversibly inhibits membrane fusion under lower ambient temperature. (A) Thermal effects on DynA mediated lipid mixing. Changes in lipid-FRET efficiency were measured over a continuous 24 h period at 24°C and 37°C. GTP concentration was 1 mM. Protein amount was 0.5 µM. Each measurement interval was 1 min. The mean of the 5 replicates is shown. The ratio between MB and NBD vesicles was 1:9. (B) Comparison between wild-type DynA and mutant DynA in lipid mixing with indicated GTP concentrations over 24 h at 24°C. Protein amount was 0.5 µM. Each measurement interval was 1 min. The mean of the 3 replicates is shown. The ratio between MB and NBD vesicles was 1:9. (C) Comparison between wild-type DynA and mutant DynA in content mixing in absence and presence of GTP over 24 h at 24°C. GTP concentration is 1 mM. Protein amount is 0.5 µM. Each measurement interval is 1 min. The mean of the 3 replicates is shown. The ratio between MB and NBD vesicles was 1:9.

contrast, when the fusion reaction was performed at 24°C, maximal FRET was reached only after 12 hours in samples without GTP and only after 20 hours in samples with GTP. We conclude that the fusion process is much faster at elevated temperature, and nucleotide addition may not be required for the fusion process per se but might help to allow DynA dynamics. To sustain ongoing fusion events, DynA needs to be released after liposome fusion to engage new vesicles. At lower temperatures, GTP induced DynA dynamics acts negatively on the stability of the tethering and hence reduces lipid FRET.

We tested the influence of different nucleotide concentrations (50 μM, 100 μM, 200 μM, 500 μM, 1 mM, and 2 mM GTP) on wild type DynA and a GTP hydrolysis deficient mutant (DynA K56A, K625A) protein. We used lipid dequenching at 24°C and observed that wild-type DynA shows a GTP-dependent decrease of lipid mixing, while the GTPase deficient mutant exhibited no differences in lipid mixing up to GTP concentration of 1 mM. Only 2 mM GTP concentration reduced the lipid mixing activity slightly both for mutant and wild-type DynA (**Figure 17B**). We assume that 2 mM GTP might interfere weakly with the stability of the liposomes and therefore reduce lipid mixing. This experiment reveals that GTP has a measurable effect on lipid mixing, but *in vitro* instead promotes a slow-down in membrane tethering and subsequent lipid mixing. This behavior is best explained by the destabilization of the DynA mediated tethering. We also tested the effect of GTP on content mixing. Wild type DynA shows a delayed content mixing again, while the GTPase deficient mutant did not reveal any differences in the presence or absence of nucleotide (**Figure 17C**). Since lipid tethering and mixing are prerequisites for content mixing, this experimental result was expected and further supported the notion that GTP hydrolysis destabilizes DynA mediated membrane clusters.

1.4 DynA exhibits phospholipid preference

Many lipid-binding proteins associate with specific lipids (Lemmon, 2008). To test whether DynA exhibits lipid specificity, we designed synthetic lipid vesicles with varying amounts of phospholipids. The lipid for membrane fusion assays used in previous experiments was extracted from *E. coli* and contained 57.5% (wt/wt) phosphatidylethanolamine (PE), 15.1% phosphatidylglycerol (PG), and 9.8% cardiolipin (CL). *B. subtilis* contains at least five major phospholipids, four of which were isolated and identified as polyglycerol phospholipids, specifically PE, PG, CL, and lysylphosphatidylglycerol, accounting 36%, 30%, 12%, and 22% respectively, when cells are grown in rich medium (Opdenkamp *et al.*, 1969).

To test the binding preference of DynA to phospholipids, we reconstructed membrane vesicles with different ratios of phospholipids *in vitro* and performed a lipid dequeching assay. When vesicles were prepared only with PE membrane fusion was not detectable (**Figure 18A**). However, when PG and PE lipids were mixed, membrane fusion efficiency increased significantly, reaching the maximum at PG = 40% and then gradually decreased. Membrane fusion could also be observed when vesicles contained only PG, indicating that PG is required and sufficient to recruit DynA to the membrane. To test the influence of CL, we constructed vesicles with a radio of PG to PE as 2:3 and added a different amount of CL, and found that CL was around 30% ~ 40% the fusion efficiency was improved (**Figure 18B**). This high concentration of CL exceeds the CL content of the plasma membrane in *B. subtilis*, which is around 12% of the total lipid content. However, CL could locally be enriched in the cell and contribute to efficient DynA membrane fusion.

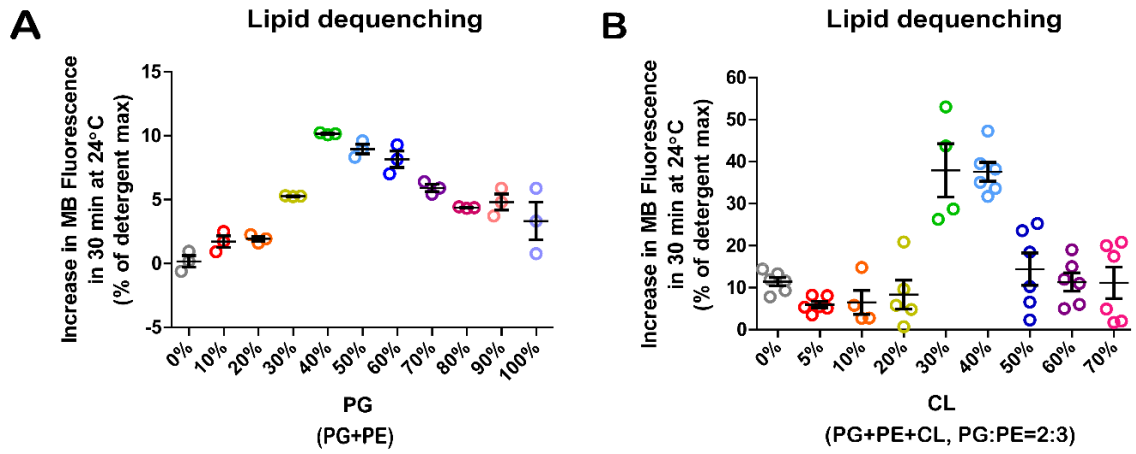

Figure 18. DynA shows phospholipid preferences. Lipid vesicles were extruded from PG, PE, and CL, and labeled for lipid dequenching assays. Vesicles were incubated with DynA at 24°C for 30 min. The detergent thesit was used to determine a putative 100% fusion. (A) DynA mediated lipid mixing is lipid-specific and requires PG. (B) CL promotes lipid mixing. Mean and SEM of 3 to 6 replicates are shown.

1.5 DynA-induced membrane remodeling *in vivo*

A strain expressing DynA-GFP (LJ-B03) was induced with xylose, and DynA-GFP localization was observed by fluorescence microscopy. In most cases, DynA-GFP was evenly distributed on the cell membrane, while there are occasional large DynA clusters in cells overexpressing DynA. A cell membrane with FM4-64 indicated that DynA was recruited by membrane invagination (**Figure 19A**). Magnification of DynA clusters revealing that the cell membrane can protrude into the cytoplasm (**Figure 19B**). We conclude that DynA can bend the cell membrane extremely and induce membrane invaginations.

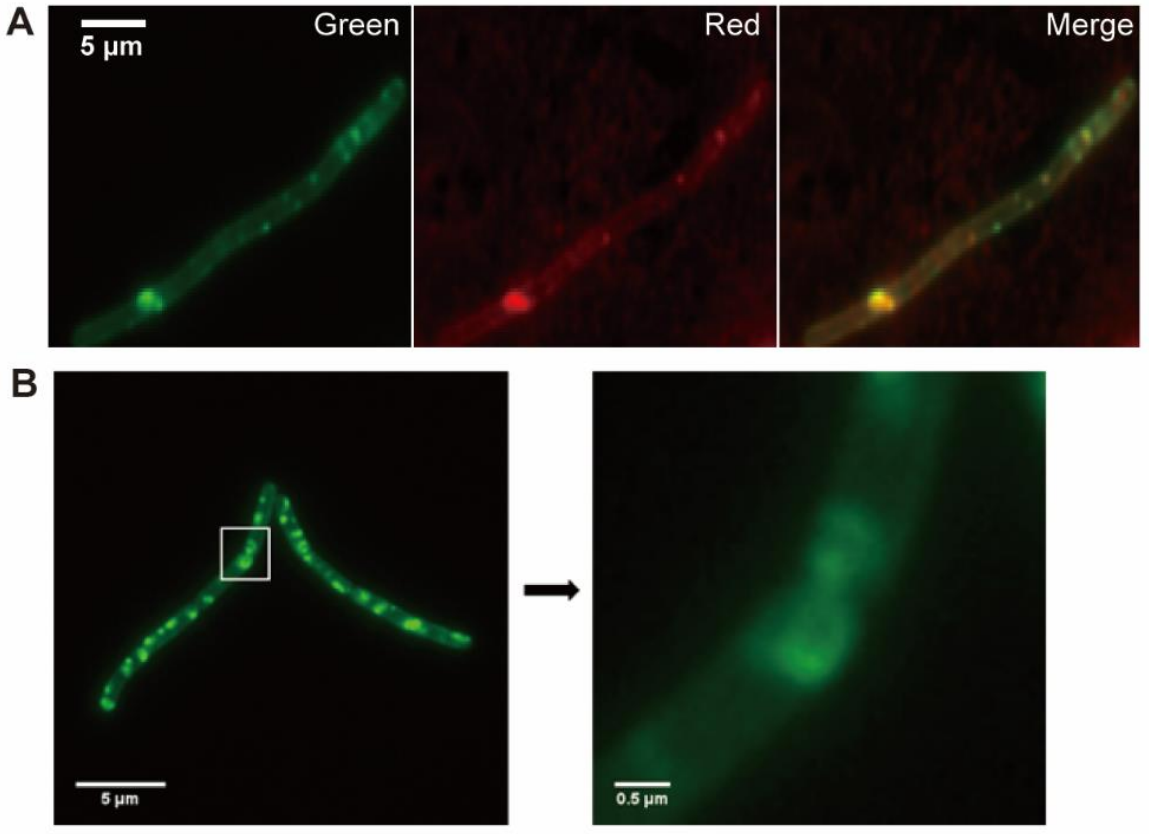

Figure 19. Overexpression of DynA occasionally resulted in large cell membrane deformation *in vivo*. (A) DynA co-localized with the membrane. (B) Magnification of membrane invaginations and DynA clusters.

2 DynA mediates resistance to membrane rupture

2.1 DynA inhibites bacteriophage-induced host cell lysis

The degree of cell lysis is inversely proportional to the expression of DynA. DynA-overexpressed (DynA++), wild-type (WT) and DynA-deficient (△*dynA*) *B. subtilis 168* strains (LJ-B01, LJ-B02, and LJ-B03) were used in the quantitative plaque assay. Similar to previous observations (Sawant *et al.*, 2016) show here that ϕ29 forms larger plaques on the lawn of *dynA*

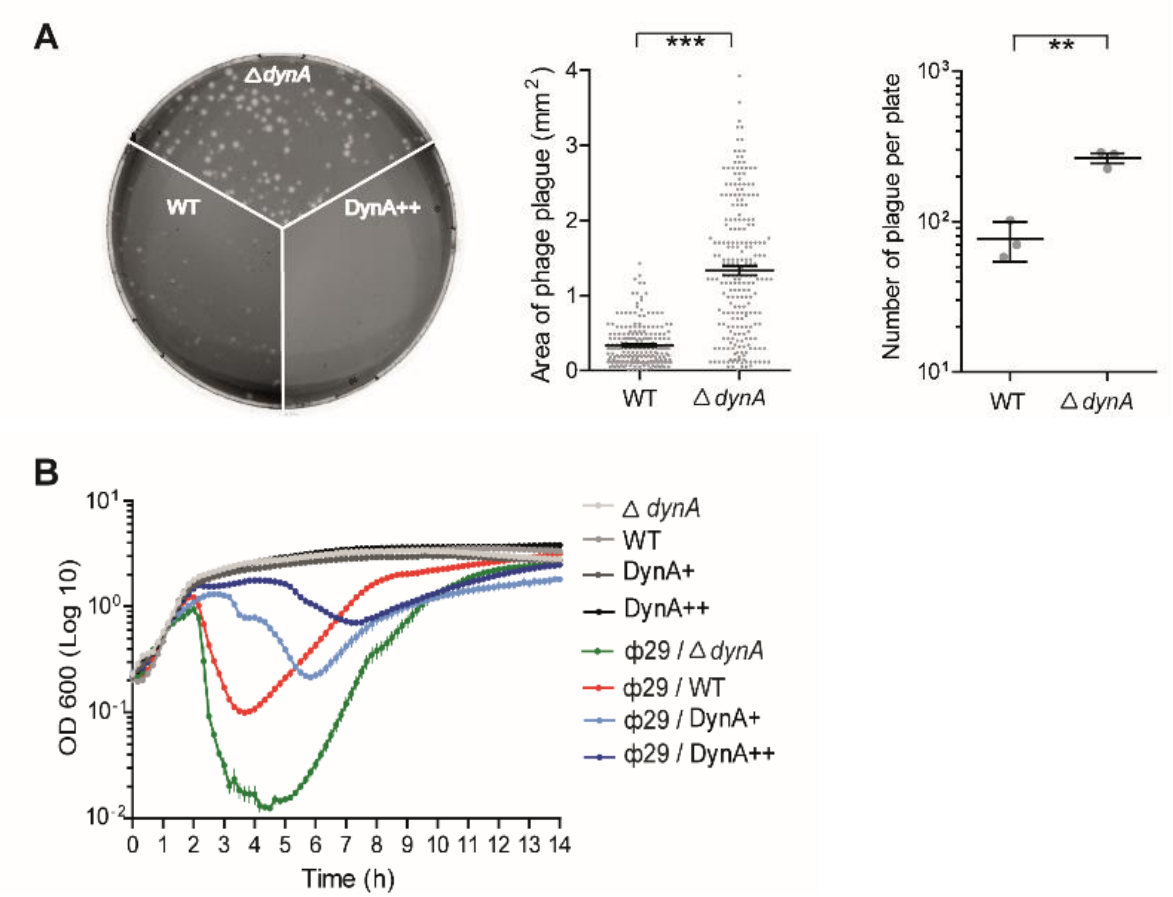

Figure 20. DynA delays phage release. (A) The same amount of phages were mixed with strains and grown on LB agar plate. Phage plagues produced on DynA-overexpressed (DynA++), wild-type (WT) and DynA-deficient (△*dynA*) *B. subtilis 168* strains (Sawant *et al.*, 2016). DynA++ was previously induced by 1% xylose for 30 min and the xylose was retained in the experiment. (B) The effect of DynA expression on the bacterial growth curve. DynA+ was previously induced with 1% xylose for 30 min but the xylose was then washed before measurement. The higher the expression level of DynA, the less of cell lysis after phage addition (MOI = 1), and the faster the re-growth after immunization. The OD 600 values was measured by a plate reader (Tecan Infinite 200 Pro) and normalized with photometer values. One star (*) means *P* value of the student t-test less than 0.05; two (**) means less than 0.01; three (***) means less than 0.001. Mean and standard error of three replicates were shown.

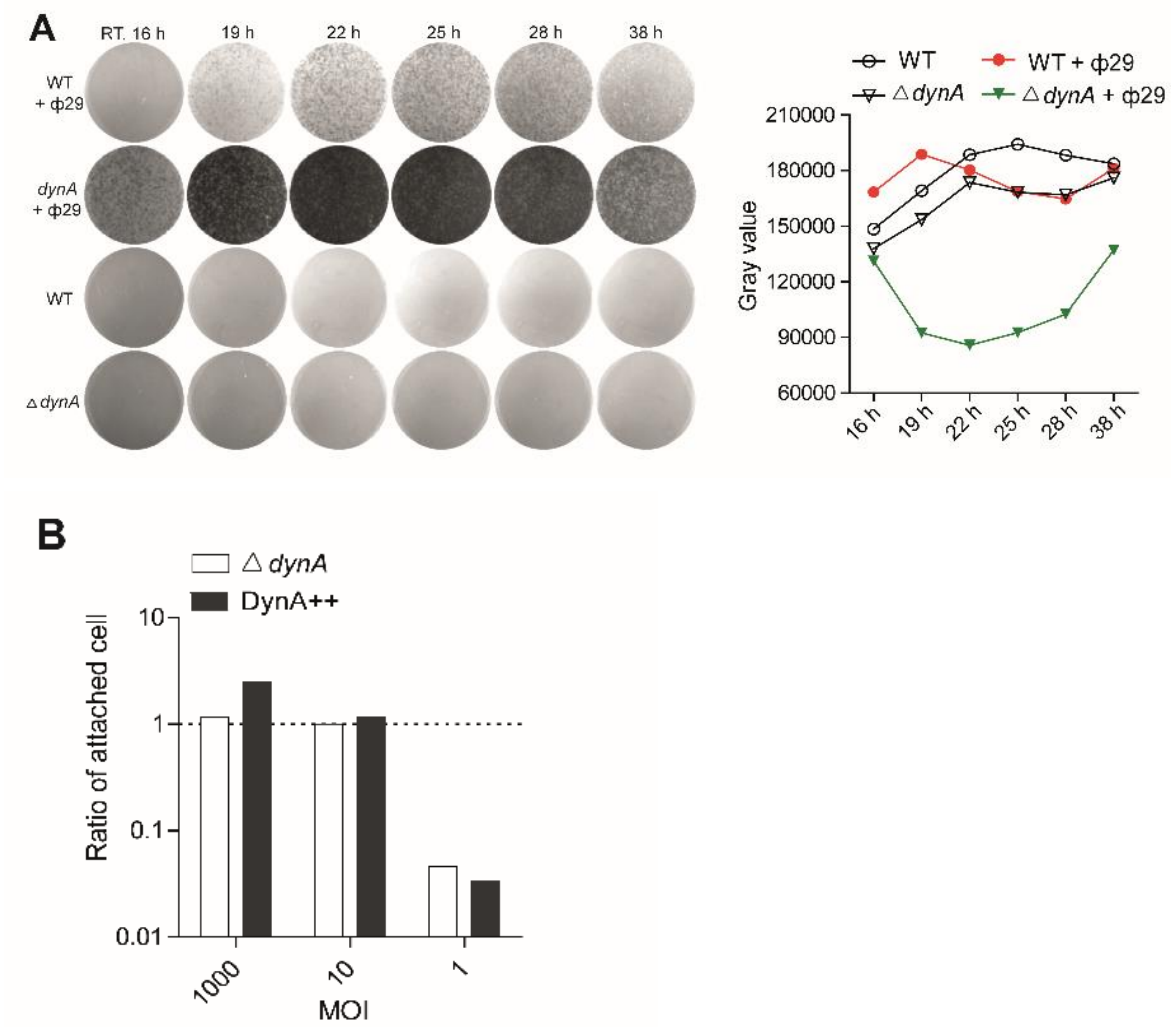

Figure 21. **Plague analysis and phage attachment test of *B. subtilis 168* strains.** (A) Plague analysis of DynA-overexpressed (DynA++), wild-type (WT) and DynA-deficient (△*dynA*) *B. subtilis 168* strains under various culture times. The amounts of bacteria and phage were shown by the gray values. (B) The proportion of bacteria attached by phages after 10 min incubation at 24℃ under varying amounts of phages.

knockout strain (△*dynA*, P = 1.652x10-46, student *t*-test), and the number was four times higher than wild-type *B. subtilis 168* (P = 0.0014) (**Figure 20A**), indicating that the lack of DynA renders cells more susceptible to lysis upon exposure to the same phages. And in the case of increasing cultivation time, the difference in the amount of phage between WT and △*dynA* was increasing until the bacteria acquire immunity and regrow (**Figure 21A**). ϕ29 forms no visible plaque on the lawn of overexpression DynA strain (DynA++). Additionally, when the MOI (multiplicity of infection) was equal to 1, the lysis of DynA-deficient bacteria was faster than that of the DynA normally expressed and overexpressed bacteria from growth curve

analysis (**Figure 20B**), indicating that the rate of lysis was inversely proportional to the protein amount of DynA.

DynA is not recruited to hinder viral DNA injection. We speculated before that DynA could prevent phage infection by repairing membrane damage during DNA injection (Sawant *et al.*, 2016). To test the hypothesis, we employed fluorescent microscopy, observing the cellular localization of DynA after cells were treated with bacteriophage. Therefore, we constructed *B. subtilis* cells (LJ-B10 and LJ-B11 strains) expressing DynA fusions with the photoconvertible fluorescent protein Dendra2 by golden-gate cloning (**Figure 7**). Furthermore, we labeled bacteriophage with photo-switchable dye Alexa Fluor 647. The fluorescently labeled phages can infect *B. Subtilis 168* cells that form plaques in the quantitative plaque assay. The

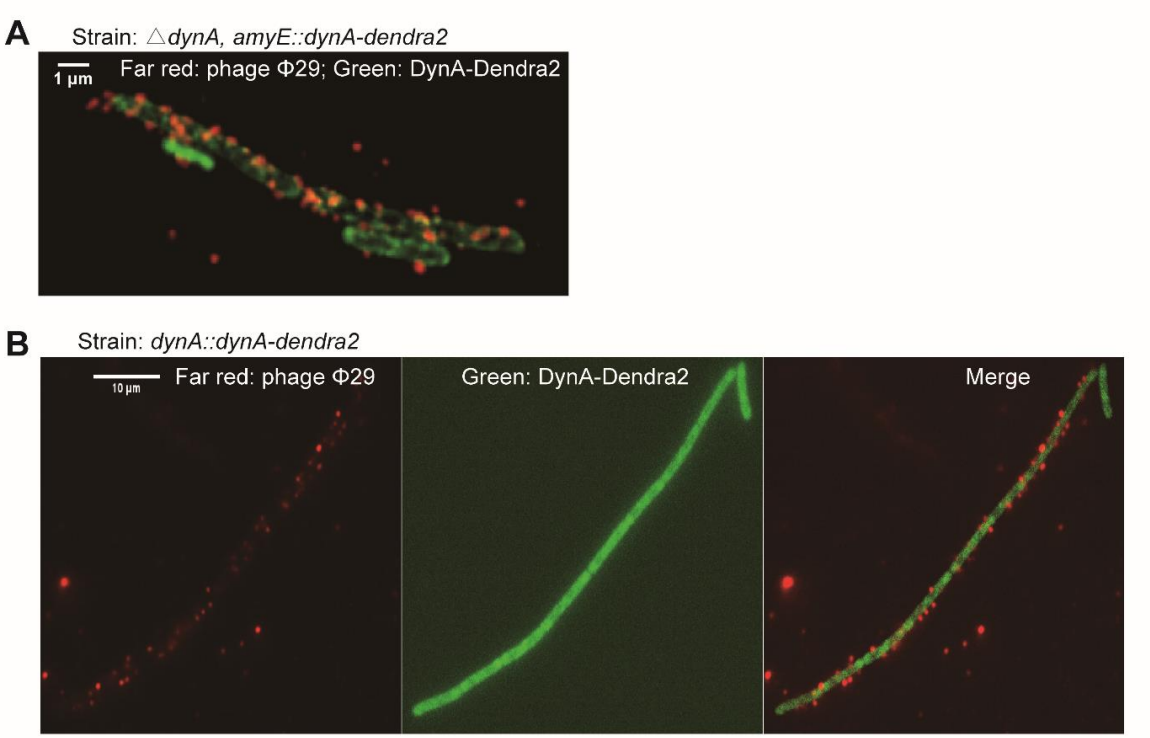

Figure 22. **Colocalization analysis of fluorescent labeled phages and DynA.** DynA-Dendra2 are overexpressed by xylose-induction (LJ-B10 strain is used here). The merge of Far-red and Green channels is corrected in Z-position.

architecture analysis of DynA clusters *in vivo* and co-localization analysis of DynA with phages may answer us if the phage resistance function of DynA is achieved by sealing distantly opposing membranes during phage DNA injection. In our study, the over-expressed DynA-Dendra2 clusters did not strictly colocalize to the fluorescently labeled phages. The fluorescently labeled phages did not strictly colocalize to the DynA-fluorescent protein clusters (**Figure 22A**). There are some independent phages and DynA clusters. Importantly, in these

experiments, DynA expression was under the control of the native promoter (**Figure 22B**). These results indicate that DynA may not function to inhibit viral DNA injection through the plasma membrane.

DynA hinders the release of the assembled phages from the cells. We tested phage attachment and host cell lysis during the first infectious cycle for the three strains (WT, △*dynA* and DynA++, **Figure 23A** and **23B**). First, when MOI was equal to 1, a similar proportion of bacteria ($P = 0.3005$ for △*dynA*: WT; $P = 0.9129$ for △*dynA*: DynA++) were attached by ϕ29 with a mean of around 10% of total cells (**Figure 23A**). When the MOI was higher than 10, all cells were attached by phage (**Figure 21B**). These results indicated that DynA does not significantly influence phage attachment. After that, we tested phage assembly and host cell lysis using a quantitative spot assay (**Figure 23B**). The bacterial membrane is destroyed after the chloroform treatment, but phage particles remain intact. Then the phage progeny that has completed the phage assembly is released, skipping the last step of host cell lysis in the phage infection cycle. Therefore, through chloroform treatment, we can know the number of phages that have been released from the host and the number of packaged phages that are still blocked in the host cell, and their sum that total assembled phages. After 1 hour of infection, the number of released phages and total assembled phages was measured using a spot assay. These always reveal that total assembled phages of △*dynA* were similar in number compared to the overexpression strain ($P = 0.3372$ for △*dynA*: DynA++), indicating that the DynA did not play a role in ϕ29 infection until phage assembly. However, when the released phages of △*dynA* were significantly more than that of the overexpression strain ($P = 0.0453$ for △*dynA*: DynA++), indicating that DynA played a role in ϕ29 infection during the last step of host cell lysis in the phage infection cycle. To address whether DynA is only active against Φ29 or has an intrinsic property against phages capable of lysing *B. subtilis*, a phage lysis test was also performed with phage SPβ by inducing the lytic cycle (**Figure 23C**). SPβ is integrated as prophage into the genome of *B. subtilis 168* strain. SPβ induction was induced by mitomycin C that caused bacterial DNA damage, which induced the lytic cycle of SPβ. Here, SPβ-lysable and *dynA*-knockout 25152 strain (Sawant *et al.*, 2016) was used for phage titer determination. The induction method was found to be feasible ($P = 0{,}0408$ for WT:WT with mitomycin), and it was found that the absence of DynA would result in fewer SPβ completing the lytic cycle ($P = 0{,}0005$ for △*dynA*+mitomycin : WT+mitomycin). All these results suggest that DynA inhibits phage infection by blocking the lysis process of host cells.

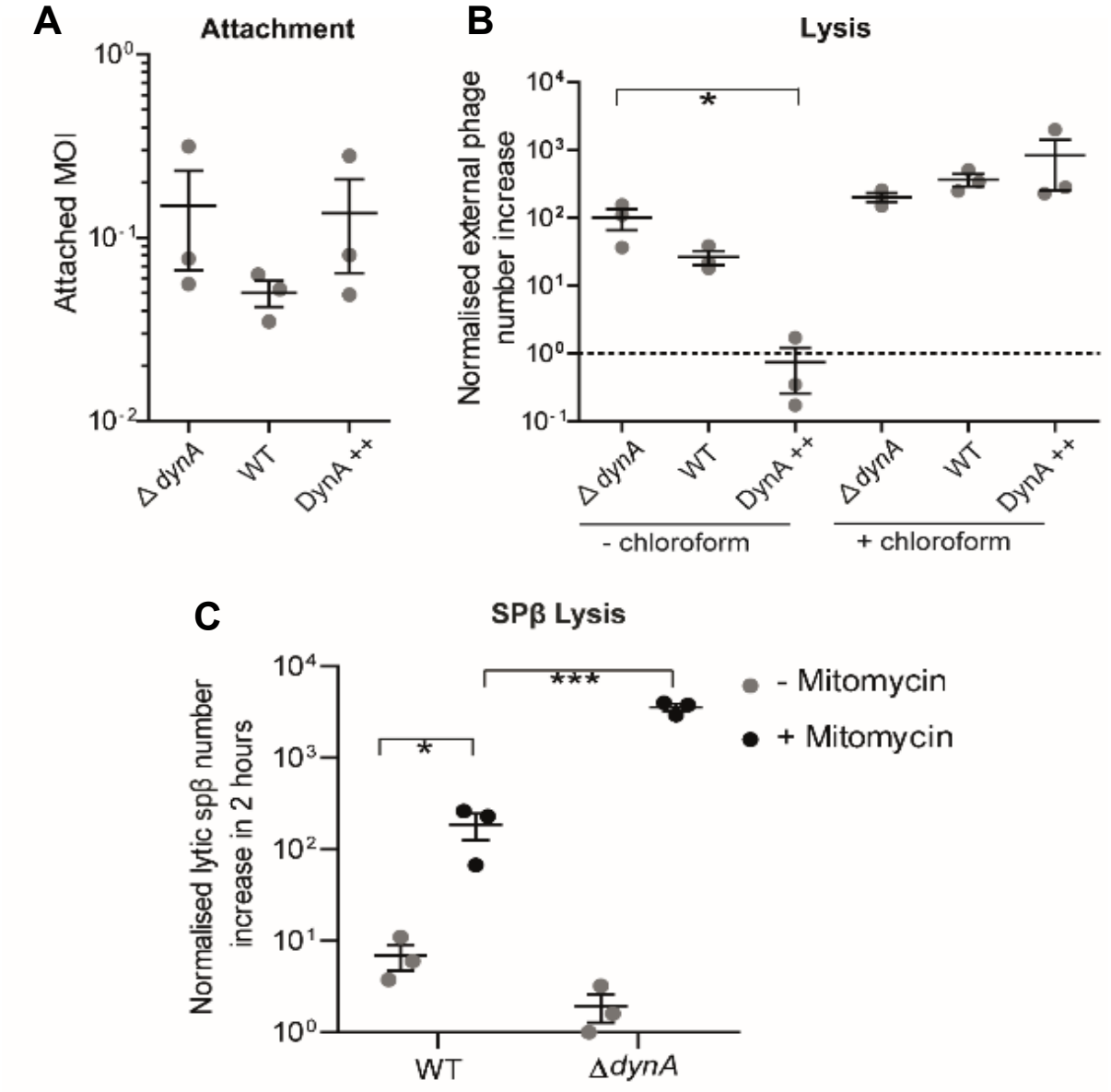

Figure 23. Plague attachment and phage lysis of *B. subtilis 168* strains. (A) There was no significant correlation between the expression level of DynA and the amount of phage attachment. The mixture of bacteria and ϕ29 (MOI = 1) was placed at 24°C for 10 min to allow phage attachment and then separate cells from extracellular phages and test attached cell ratio by quantitative spot assay. (B) DynA interferences host cell lysis after progeny phage assembly. Extracellular phages were tested by quantitative spot assay. (C) Lytic induction of the lysogenic phage SPβ on *B. subtilis* 168 and △ *dynA* strains. After mitomycin treatment and 2-h waiting, △ *dynA* showed more lysogenic phages induced to lytic cycle than the wild type strain. One star (*) means *P* value of the student t-test less than 0.05; two (**) means less than 0.01; three (***) means less than 0.001. Mean and standard error of three replicates were shown.

DynA traps phage DNA inside the cells. We also compared phage DNA replication of DynA-deficient, wild-type and DynA over-expression strains by quantifying internal, external and total phage DNA (**Figure 24**). When the MOI was equal to 10, the bacteria internal phage DNA of △*dynA* showed a more significant decrease after 45 min infection. Before that, there was no significant difference in the growth of internal phage DNA between the three strains ($P = 0.5189$ for △*dynA*: DynA++; $P = 0.9382$ for △*dynA*: WT), indicating that DynA did not affect the replication of phage DNA inside the bacteria. The total phage DNA of three species remained indistinguishable within 90 min ($P = 0.9821$ for △*dynA* : DynA++; $P = 0.6218$ for △*dynA* : WT). However, the amount of internal phage DNA in △*dynA* cells was significantly lower

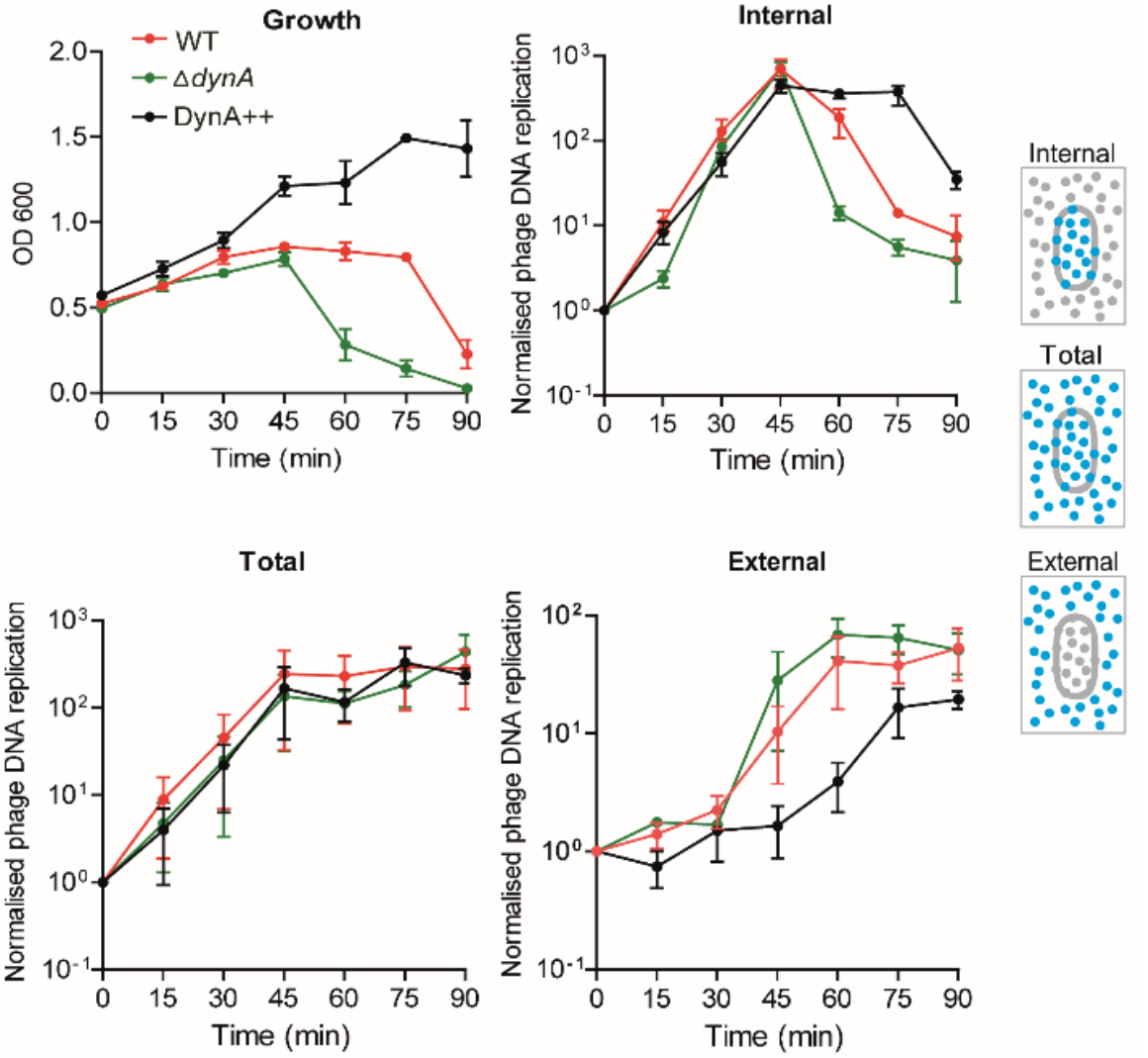

Figure 24. Phage DNA replication analyzed by qPCR. Strains ΔdynA, DynA++ and wild type were analyzed. The mixture of bacteria and ϕ29 (MOI = 10) was pre-placed at 24°C for 10 min to allow phage attachment and then transferred to shaker of 37°C for measurement. Phage DNA of inside or on the cell, in total, and outside the cell were quantified every 15 min and normalized by dividing the start value.

after 45 min. This indicates that △*dynA* released the phage DNA earlier than wild-type and overexpression strains, which was also verified in the growth curve of the external phage DNA. In general, the presence of DynA did not influence phage attachment to DNA replication and phage assembly. Still, it hindered the process by which assembled phages were released by host cell lysis.

DynA assemblies *in vivo* interfere with phage-induced cell lysis. We fluorescently labeled phage in capsid/DNA and DynA *in vivo* to study the interaction between them at the single-cell level. In the cells of DynA++, DynA was coupled to fluorescent protein GFP and over-expressed with xylose induction. First, phage infection induced the change of DynA dynamics, from uniformly distributed on the cell membrane to large protein clusters. It did not occur in

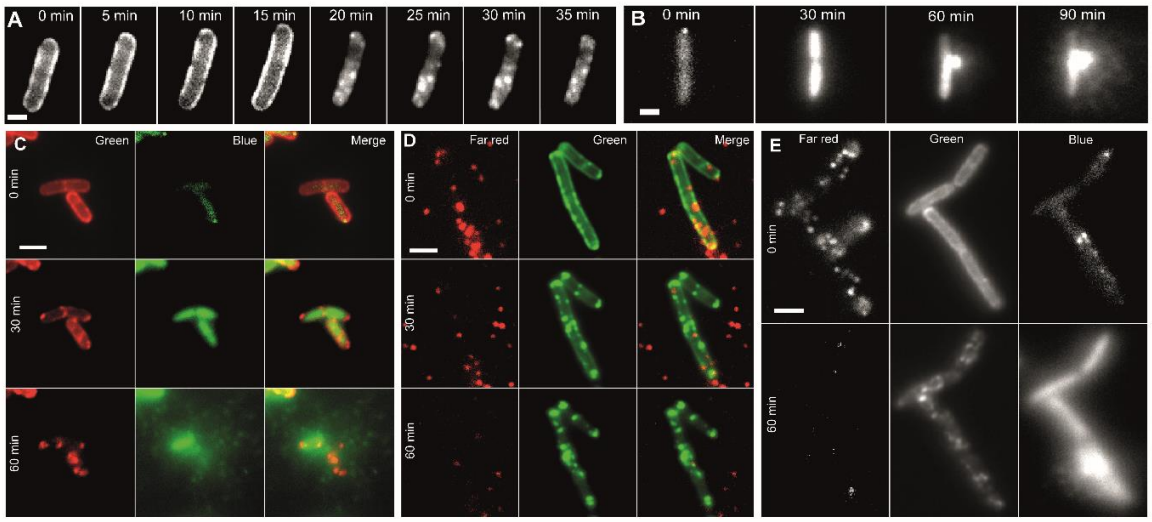

Figure 25. The *in vivo* interaction between DynA and ϕ29 observed by fluorescent labeling. (A) ϕ29 induces DynA oligomerization *in vivo*. When the bacteria were exposed to phages (MOI = 1), DynA could assembly into large clusters approximately 30 min after phage attachment at 37°C. (B) Phage-induced bacterial lysis by labeling phage DNA. (C) The movement of DynA-GFP and phage DNA (phage DNA were labeled with hoechst dye, shown in blue channel). (D) The movement of DynA-GFP and paternal phages in phage infection (paternal phage capsids were labeled with Alex 647 dye, shown in far-red channel). (E) Simultaneous phage movement and bacterial lysis process by double-labeling phages in capsid and DNA.

the early stage of phage infection (**Figure 25A**) because the clustering of DynA occurred after ten minutes of phage attachment and 20 minutes of microscopic monitoring. The 29 infection cycle is about 45 minutes (Hemphill & Whiteley, 1975). Also, we labeled the phage DNA with the DNA dye Hoechst. Attached phages were observed as bright blue fluorescence foci on the cell, and after 30 min of infection, the spots disappeared. Instead, Hoechst fluorescence became

visible inside the cell, possibly due to the injection of phage DNA from outside the cell into the cell (**Figure 25B**). Between 30 and 90 min, the internal fluorescence of the bacteria bulged until cell lysis, and the blue fluorescence bursting out was fragmented, indicating progeny phage particles. When DynA in the overexpressing strain was labeled with green-fluorescent protein GFP, and the cells were mixed with the DNA-labeled phage, we observed that DynA aggregation happened before phage DNA burst (**Figure 25C**). When the phages were labeled in the capsid, the gradual phage detachment from the cells over time was observed, and the process was accompanied by DynA aggregation (**Figure 25D**). In general, the parent phages were able to detach from the bacteria, and the progeny phage was able to erupt from the bacteria after phage attachment and a one-hour infection, which also was observed with double-labeled phage (**Figure 25E** and **Figure 26**).

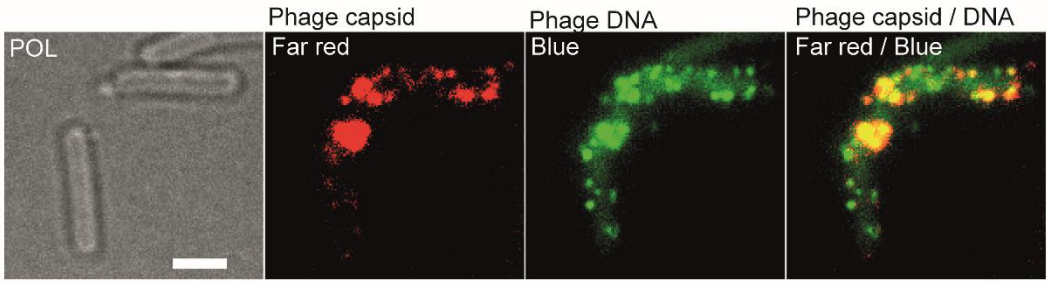

Figure 26. Observation of capsid and DNA double-labeled phages. Phage capsid was shown in far-red channel and phage DNA was shown in bule channel.

Finally, we compared the cell lysis ratio of △*dynA* and overexpression strains (**Figure 27**). They found that the ratio of △*dynA* was significantly higher than DynA++ after phage attachment and 90 min infection (**Figure 27A and 27C**, $P = 0.0014$ for △*dynA*: DynA++). Additionally, we observed the intermediate state of phage DNA injection in **Figure 27B** that was the enlargement of the white box in **Figure 27A**.

DynA is a dynamic protein that forms static foci during phage infection. We also wished to bolster the findings of an increased formation of DynA foci at the cell membrane using single-molecule tracking (SMT). In addition to statically positioned molecules visible by epifluorescence, SMT also visualizes and quantifies freely diffusing molecules. We used SMTracker software to analyze tracking data (Rosch *et al.*, 2018). If DynA were to diffuse throughout the cells and become more engaged in repairing membrane irregularities in response to phage infection, we would expect a decrease of freely diffusing molecules and an increase in statically positioned molecules. We used 20 ms stream acquisition to track DynA-YFP

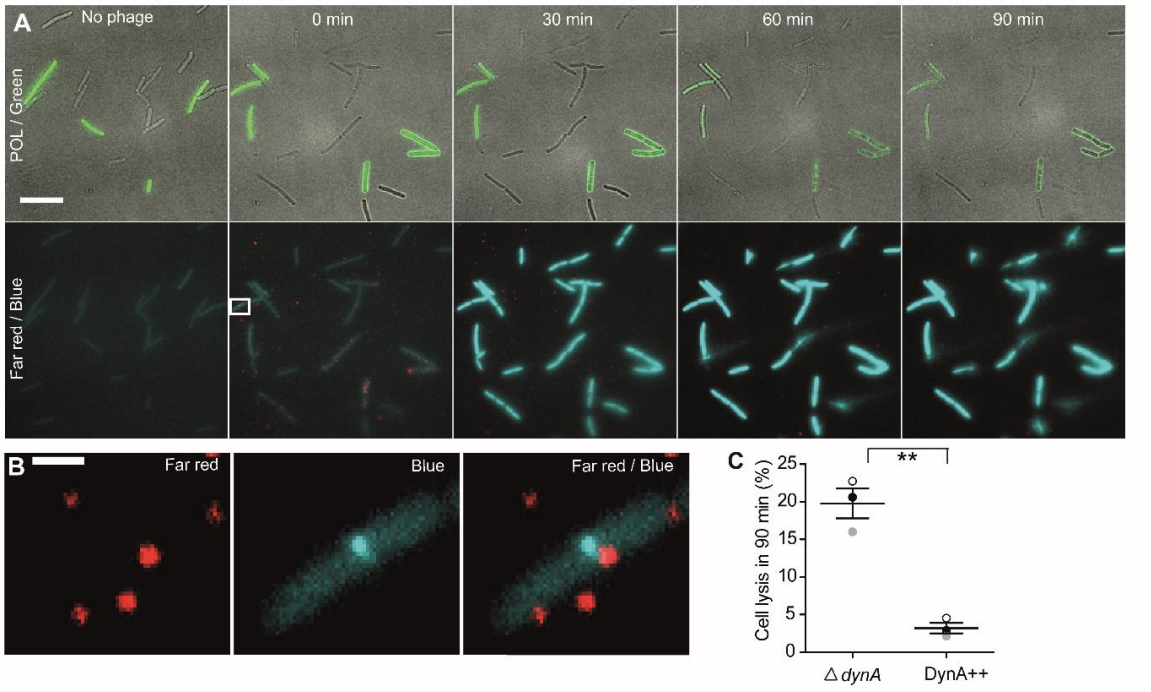

Figure 27. DynA assemblies *in vivo* interfere against cell lysis. (A) Fluorescent microscopy analysis of DynA-overexpressed (DynA++, DynA-GFP was shown in the green channel) and DynA-deficient (△*dynA*) *B. subtilis 168* strains under various infection times with ϕ29 (phage DNA was shown in the blue channel). (B) The intermediate state of phage DNA injection (phage capsid was shown in the far-red channel, and phage DNA was shown in the blue channel. (C) Quantification of bacterial lysis of DynA overexpressed and deficient strains.

expressed from the original gene locus, under the control of the original promoter. **Figure 28A** shows all tracks (minimum length of four steps) into a standardized Bacillus cell of 3 x 1 µm size. While blue tracks indicate all freely diffusive molecules, red tracks show the confined movement of molecules and green tracks transitions between diffusive and confined movement. DynA arrests at the cell membrane in some cases, while predominantly, it is freely diffusive. 60 minutes after infection with phages (MOI = 1), the number of confined, membrane-localized tracks strongly increased, as expected (**Figure 28B**). To characterize further the mode of diffusion of DynA, we employed Gaussian Mixture Modelling (GMM), in which displacements of molecules in x and y direction are evaluated as a probability density function. Tracks with little movement center around "0", and fast tracks are away from the central axis. The shape of the function shown in **Figure 28C** is not Gaussian, which indicates the existence of at least two populations with different diffusion constants. In fact, data could be best described by assuming three distinct populations. These have diffusion constants of 0.023 $\mu m^2/s$, 0.25 $\mu m^2/s$, and 1.2 $\mu m^2/s$, and sizes of 28, 45 and 26%, respectively (**Figure 28E** and **28F**). The populations are most easily explained by assuming a freely diffusive population, most likely consisting of monomers, a membrane-associated fraction diffusing in a constrained manner, and a slow-

moving/immobile fraction engaged in membrane repair. Upon phage infection, the static

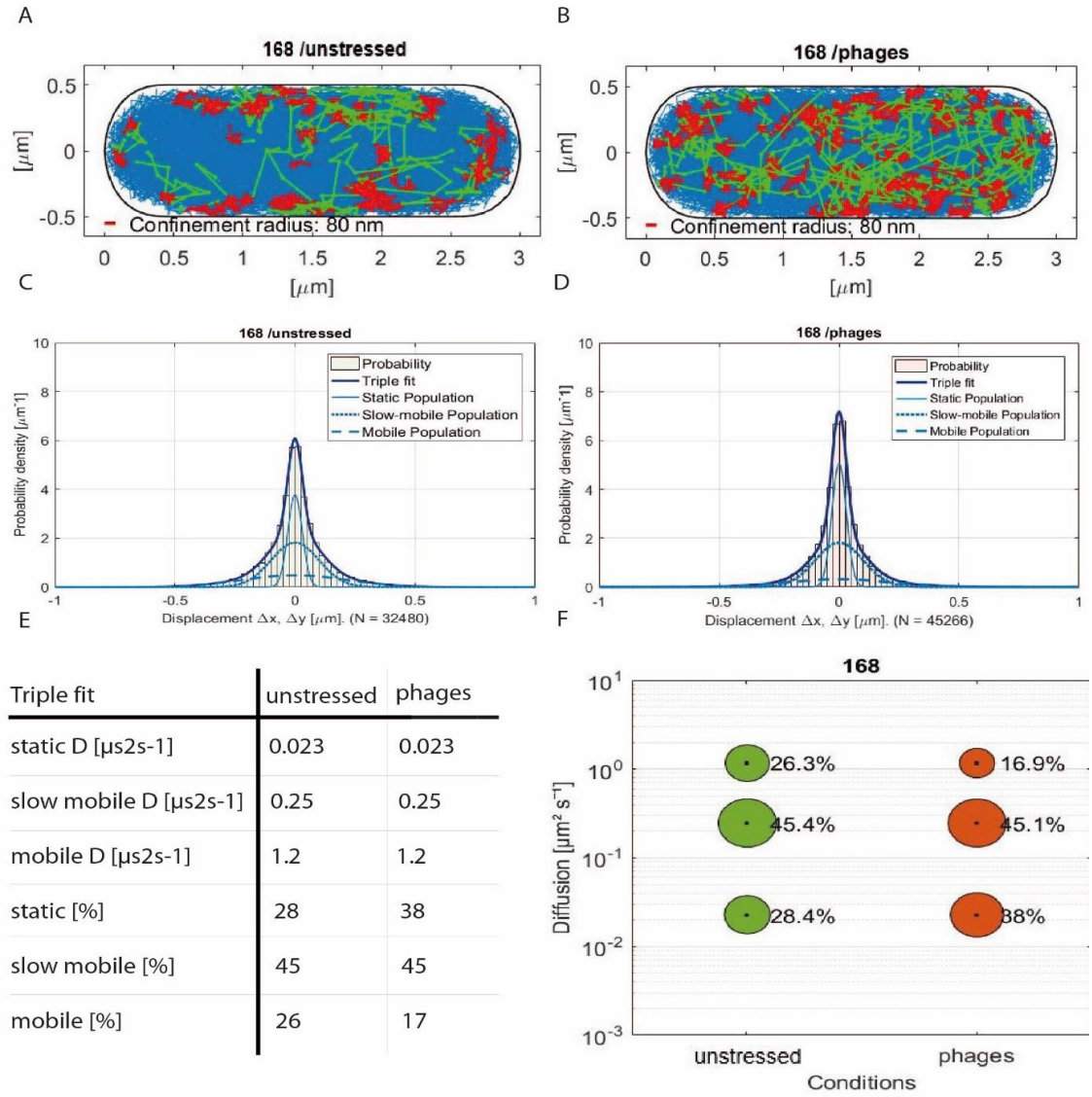

Triple fit	unstressed	phages
static D [μs2s-1]	0.023	0.023
slow mobile D [μs2s-1]	0.25	0.25
mobile D [μs2s-1]	1.2	1.2
static [%]	28	38
slow mobile [%]	45	45
mobile [%]	26	17

Figure 28. Changes of DynA dynamics in response to phage infection analyzed by single molecule tracking. Tracks of DynA-mV displayed in a standardized cell of 1 x 3 µm in (A) unstressed exponential growing cells or in (B) cells infected with ϕ29 bacteriophages after 60 minutes. Freely diffusive tracks are shown in blue, confined tracks within a radius of 80 nm and a step length of 9 are depicted in red, and transient tracks showing mixed behavior are shown in green. (C-F) Diffusive behavior of DynA-mV in Gaussian-Mixture-Model (GMM) analyses of frame to frame displacements in x-and y-directions in exponential growth phase (C) unstressed or (D) stressed with ϕ29 bacteriophages. The dark blue line indicates the overall fit of the three Gaussians distributions. Dashed, dotted and solid lines in brighter blue are the Gaussian distributions corresponding to mobile, slow mobile and static fractions, respectively. The diffusion constants ([µs2s-1] in (E) or y-axis in (F) and fraction sizes ([%] and bubble size) are shown in comparison to the two conditions of DynA-mV with a step size distribution of three populations, a static (lower bubbles), an intermediate mobile (middle bubbles) and a fast mobile (upper bubbles) fraction. (Data from Prof. Dr. Peter Graumann and Laura Sattler)

fraction increases to 38% of DynA molecules, to the expense of the freely diffusive molecules, while the intermediate fraction remained constant (**Figure 28D** and **28F**). This observation suggests that while more DynA molecules become actively involved in membrane repair, most molecules continue to scan the membrane for lesions. As a second measure for activity, we determined average dwell times of molecules, assuming that catalytically active molecules will remain in a confined motion, and thus statically positioned for many steps. Keeping in mind that dwell times are underestimated in our assays because of molecule bleaching during the acquisition, we can nevertheless conclude that following phage infection, dwell times of DynA strongly increase. While during exponential growth, 87.7% molecules arrested for 73 ms (even freely diffusing molecules may stop for a short period), and 12.3% of the molecules arrested for 200 ms (**Table 2**); the latter corresponds to the molecules engaged in confined motion at the cell membrane (**Figure 28A**). 60 minutes after infection, 71.3% of DynA molecules changed to longer dwell times of 290 ms, at the expense of molecules stopping for only 62 ms on average (**Figure 28**). Thus, there is a strong shift towards extended dwell times 60 min after phage induction, supporting the idea that DynA molecules react to a strongly increased number of targets within the membrane.

Table 2. Average dwell times of DynA-mV

	exponential	**phages**
average lifetime (frame/s)	7.4 / 0.15	8.6 / 0.17
average residence time [s]	0.100 ± 0.002 s	0.283 ± 0.011 s
τ_1 [s]	0.073 ± 0.00062 s	0.19 ± 0.0062 s
τ_1 [%]	87.7 ± 1.32 %	28.7 ± 5.23 %
τ_2 [s]	0.2 ± 0.012 s	0.29 ± 0.0062 s
τ_2 [%]	12.3 ± 1.32 %	71.3 ± 5.23 %

τ: dwell time

2.2 Characteristics of DynA in nisin resistance

We labeled nisin with photo-switchable dye Alexa Fluor 647. When antibiotic nisin was fluorescently labeled, and DynA-GFP was overexpressed with xylose induction (LJ-B03 strain), we were able to observe that the cells with high concentrations of nisin (shown in the far-red channel) were accompanied with clusters of DynA-GFP (shown in the green channel). In contrast, the cells without high concentrations of nisin, DynA-GFP could be more uniformly distributed (**Figure 29A**). Besides, the correlation between the concentration of nisin and the number of DynA clusters in a single cell was tested (**Figure 29B**). Specifically, different concentrations of nisin (0 to 100 μg/ml) were added to the bacterial cultures (LJ-B03 strain, with xylose induction) and incubated for 30 minutes before imaging. The number of DynA-GFP clusters in each cell was recorded by fluorescent microscopy, and more than one hundred cells were recorded at each concentration. It showed that the higher the concentration of nisin, the higher the proportion of the number of DynA clusters greater than 5 in a single cell.

We employed fluorescent microscopy observing the cellular localization of DynA after cells were treated with antibiotic nisin. *B. subtilis* strains expressing DynA fusions with the photoconvertible fluorescent protein Dendra2 (LJ-B10 and LJ-B11 strains) were constructed. We also performed an adequate co-localization analysis of nisin and DynA clusters (**Figure 29C**). The over-expressed DynA-Dendra2 clusters did not strictly correspond to the fluorescently labeled nisin, and the fluorescently labeled nisin did not precisely correspond to the DynA-Dendra2 clusters. There are some independent nisin particles and DynA clusters. Similarly, when DynA-Dendra2 was expressed under the control of the original promoter (LJ-B11 strain), DynA-Dendra2 was not strictly co-localized with nisin (**Figure 29D**).

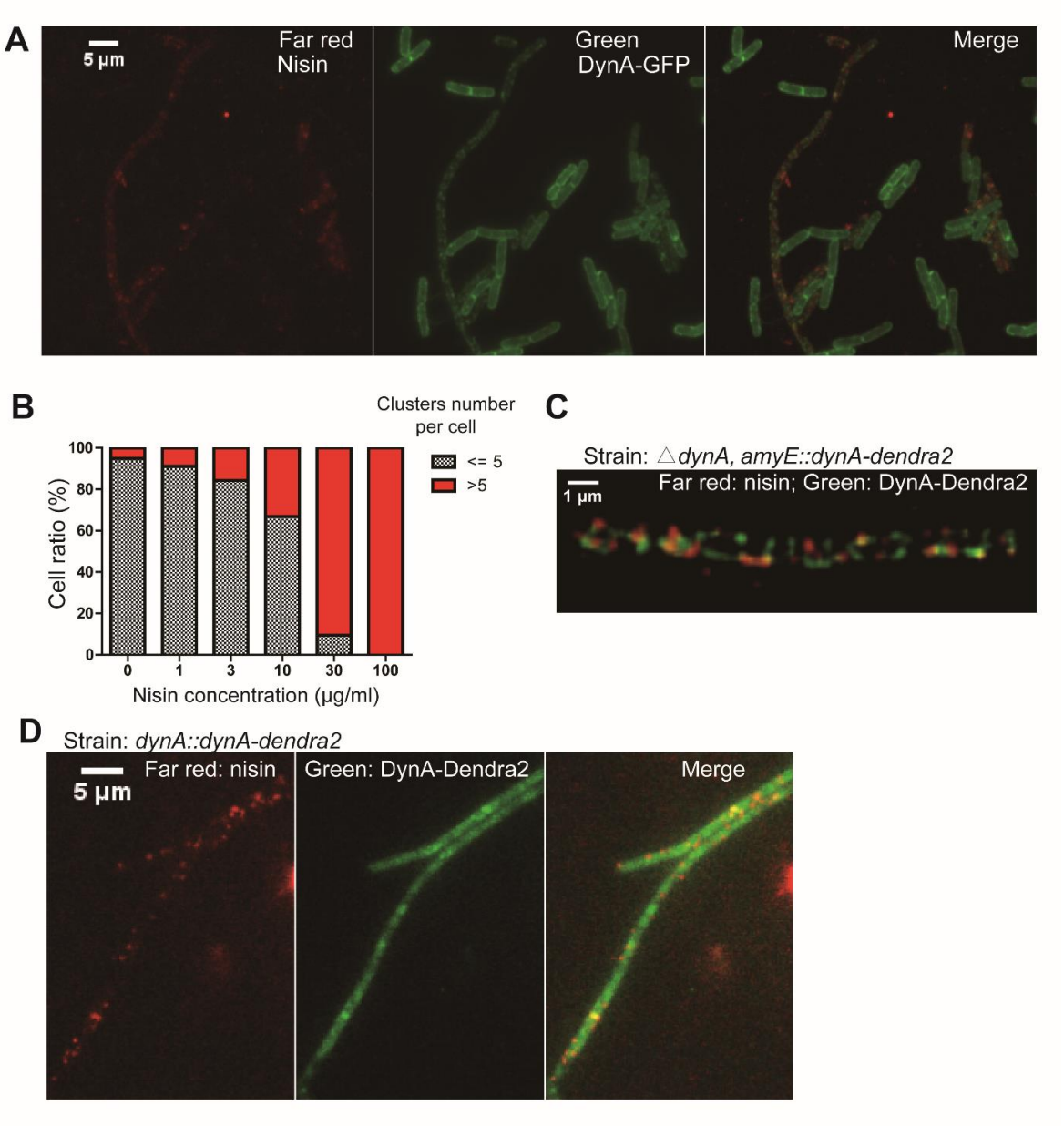

Figure 29. The *in vivo* interaction between DynA and antibiotic nisin observed by fluorescent microscopy. (A) Microscopy analysis of fluorescently labeled nisin (shown in far red channel) and DynA-GFP (strain LJ-B03, shown in green channel). Three µl fluorescently labeled nisin was mixed with 1 ml bacterial culture and the mixture was incubated for 30 min at 37℃ before imaging. (B) DynA clusters formation is nisin concentration dependent (strain LJ-B3). (C) Colocalization analysis of fluorescently labeled nisin and DynA-dendra2. DynA-Dendra2 were expressed with xylose induction (strain LJ-B10). The merge of the far-red and green channel is corrected in Z-position. (D) Colocalization analysis of fluorescently labeled nisin and DynA-dendra2. DynA-Dendra2 were expressed under control of the native promoter (strain LJ-B11).

3 Negative-stain EM of DynA

Negative staining is a common technique for the structural study of biological macromolecules by using electron microscopy. It is often used for single-particle analysis. The embedding of a specimen in a layer of dried heavy ions (in the stain), which strongly interact with (or scatter) the electron beam and thereby produce strong phase contrast on the micrographs so that molecules can be visualized clearly in the detector. The 3D reconstructions in this manner are usually limited to a resolution around 15-20 Å.

3.1 Sample preparation and image acquisition for electron microscopy

DynA was isolated by Ni-NTA agarose and further gel filtrated on the increase superose 6 column in T5 buffer. As **Figure 9B**, Purified DynA eluted around 15 ml in the gel-filtration

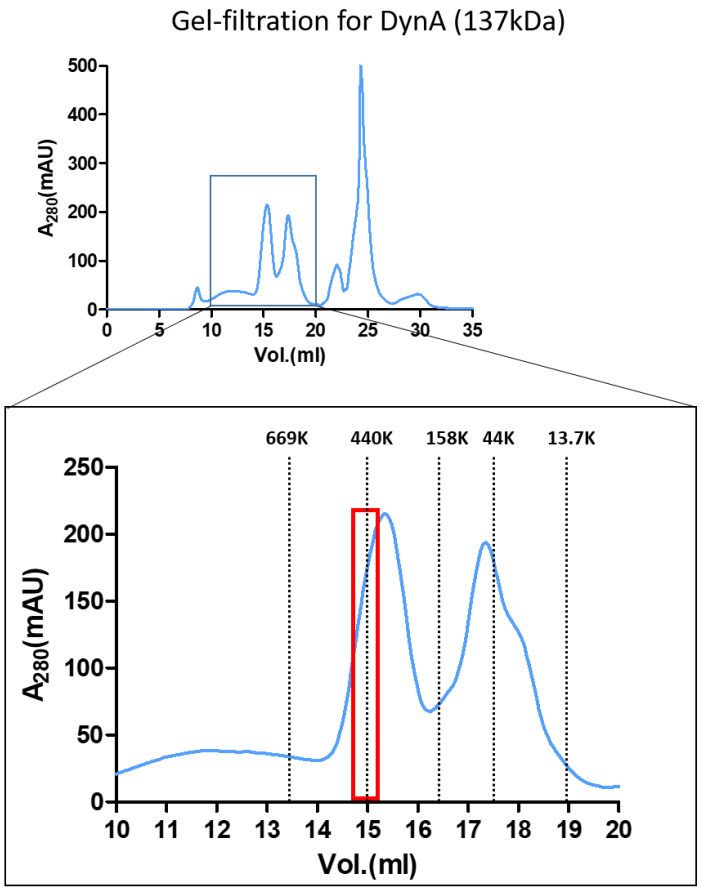

Figure 30. Purification of DynA by gel-filtration size-exclusion chromatography for electron microscopy. The fraction of the DynA peak (red frame) was selected to be the sample in electron microscopy. By referring to the instruction manual of the Superose 6 increase column, the approximate position of the proteins of different sizes (669, 440, 158, 44, 13.7 kDa) were in the outline, and our sample is near the position of 440 kDa protein.

chromatography. The first fraction from the elution pick was used for further analysis (**Figure 30**). Comparison with the elution profile of standard proteins, the approximate molecule size of the selected sample was around 440 kDa. The molecular mass of DynA is 137 kDa, indicating that most polymers of DynA in the sample may be trimers or tetramers.

Freshly purified DynA was placed on the grid covered with carbon and negatively stained with Uranyl acetate. Negatively stained proteins were imaged with a JOEL JEM 2100F microscope. We generated 226 raw micrographs, and these micrographs were recorded at -2 μm defocus. The pixel size of micrographs was 3.67 angstrom per pixel. A representative of 4k pixels is

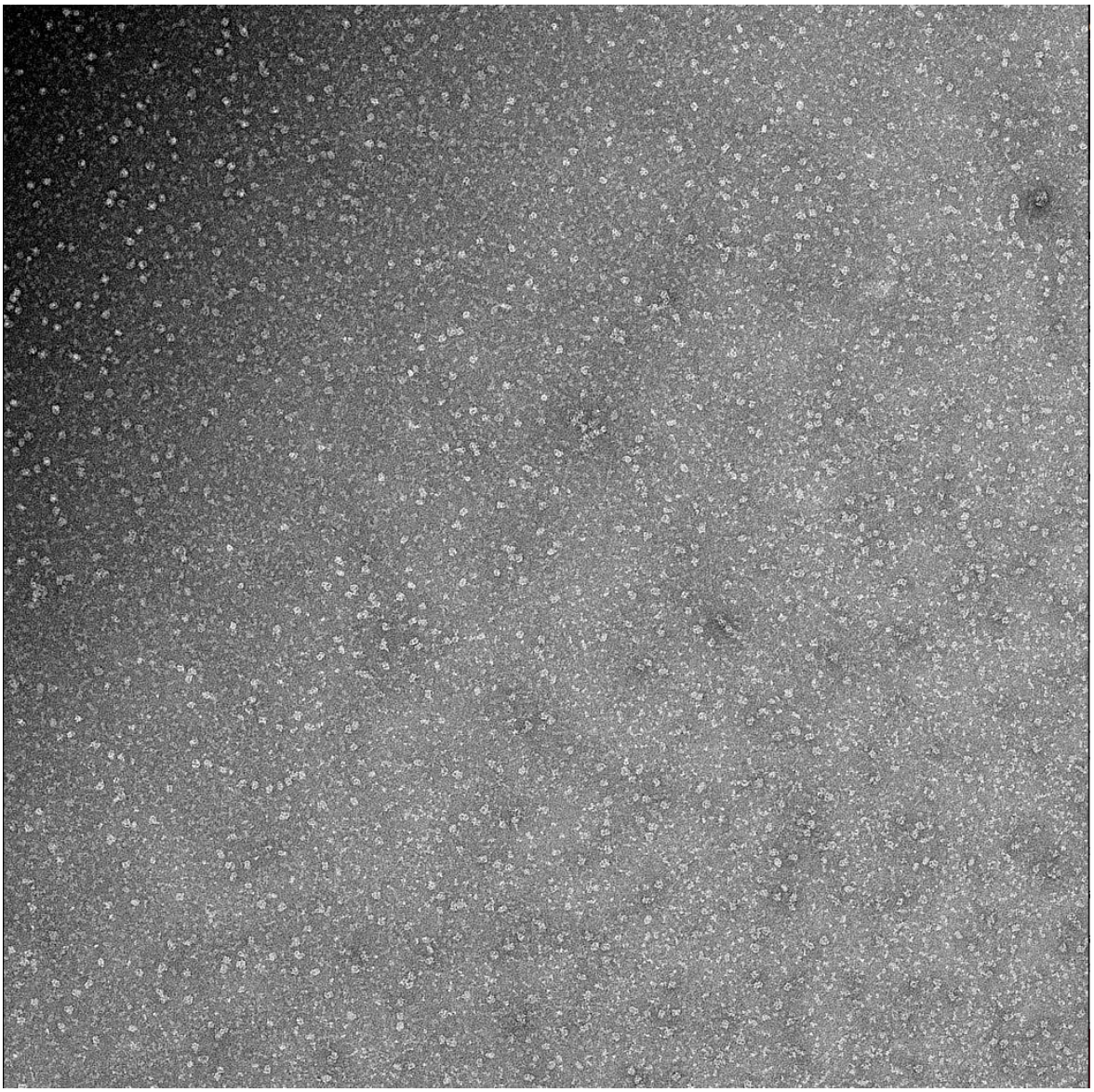

Figure 31. Negative staining EM micrographs of DynA. It shows single particles randomly dispersed on the carbon and covered with stain. A few aggregated proteins could be seen.

shown (**Figure 31**). Most of the DynA particles were found to be mono-dispersed and randomly orientated on the carbon film.

3.2 CTF estimation

There is distortion in the image formation depending upon the physical parameters of the electron microscope, such as accelerating voltage, lens aberrations, and, crucially, the displacement of the focal plane (defocus) at the time of imaging. But it can be described by the modulation of a contrast transfer function (CTF), which is the Fourier transform of the optical system point spread function. The signal in electron micrographs is modulated by an oscillating non-linear contrast transfer function of the form: $\mathrm{CTF}(f) = E(f)\sin\left(\pi\ Cs\ \lambda^3\ f^4/2 - \pi\ \lambda\ d\ f^2\right)$ where Cs is a spherical aberration of the electromagnetic lens; λ is the electron wavelength; f is the spatial frequency, d is the applied defocus (negative for under focus), and E(f) is an envelope function describing high-resolution information degradation. By fitting a theoretical CTF curve to the experimentally observed 2D Thon rings of a micrograph, the applied defocus d can be estimated. The effect of the CTF on the signal can be partially reversed.

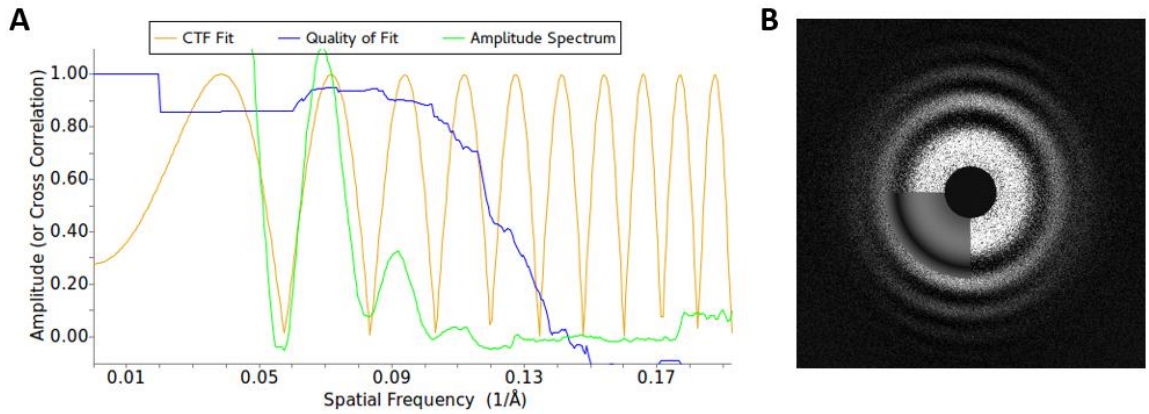

Figure 32. The outputs from the ctffind4 of a negative stained micrograph. (A) Output diagnostic plots describing the experimental amplitudes (blue), the fit CTF (yellow) and goodness of fit (blue) for micrograph of. For this micrograph, the final estimates were DF1 = 11267 Å, DF2 = 10667 Å and Astig = 15.59 °. The highest resolution at which Thon rings were deemed to be modeled correctly was 8.39 Å. (B) Diagnostic 2D CTF image from by CTFFIND4.

Since the data was collected under defocus at -2 μm, we estimated the CTF parameters for each corrected micrograph by running the processing of Relion CTFFIND 4.1 (written by Alexs Rohou and Nikolaus Grigorieff in University of Massachusetts Medical School). Once the processing job is finished, output files for each micrograph contain the computed power spectrum and the fitted CTF model. Among them, the defocus value for our micrographs from

CTF estimation was in the range from 8,138 to 24,481 Å (**Figure 32**). The resolution range of CTF correction was set to 15 - 40 Å. The Thon rings in the experimental images coincided with the simulated mathematical model (CTF fit curve in the 1D CTF plot). The estimation of the highest resolution for a good fit can be used as a measure of the quality of the fit as a function of spatial frequency and suggest this can be used to define the highest resolution at which CTF oscillations were successfully modeled.

3.3 Manual picking and 2D classificaiton of apo-DynA particles

In the single-particle analysis, two-dimensional image classification has two essential functions: first, the image classification can sum and average the original particle pictures with the same orientation parameters, improve the signal-to-noise ratio and contrast of the image, which is beneficial to the following step that more accurate solution of orientation parameters. Second, biological macromolecular complexes often have multiple conformations. The particles picked by automation are often doped with "wrong" and "damaged" particles. A useful classification of the original image data set can identify these bad particles, and they can be eliminated from the analysis. And the conformation of a variety of complex particles can be separated and analyzed, which is crucial for the next step to obtain high-resolution 3D reconstruction. Here, 10513 particles were manually picked with a pick diameter of 210 angstroms. These manually picked particles were classified into 16 averages, of which 14 averages were selected as templates for automatic picking in the next step. 247,250 particles were auto-picked. The picking threshold is 0.1. The minimum inter-particle distance is 140 angstroms, the maximum standard deviation noise is 1.1 particles per micrograph on average is 1070. Particles were extracted in the boxes with the diameter of 100 pixels (**Figure 33**). Relion also has functionalities to quickly sort particles based on the difference between each particle and their aligned, CTF-corrected reference and throw away bad particles using reference-free 2D class averaging. After particle sorting and averaging, we had 120 types of particles, and these types might not intuitively have a uniform single molecular structure. In other words, there might be multiple types of polymerization of DynA.

Among them, the most interesting types of particles were shown in **Figure 34**. The left one was a hexagon, and the right one was a quadrangle. They were respectively composed of six and four corners on the outside. Both D1 and D2 subunits of DynA have substantial structural similarity with BDLP (Burmann *et al.*, 2011), and BDLP appears as a folded corner when GDP is combined. From this, we assumed that the particles in **Figure 34** were likely to be a top view of the trimer and dimer of DynA (every two corners might be a DynA monomer).

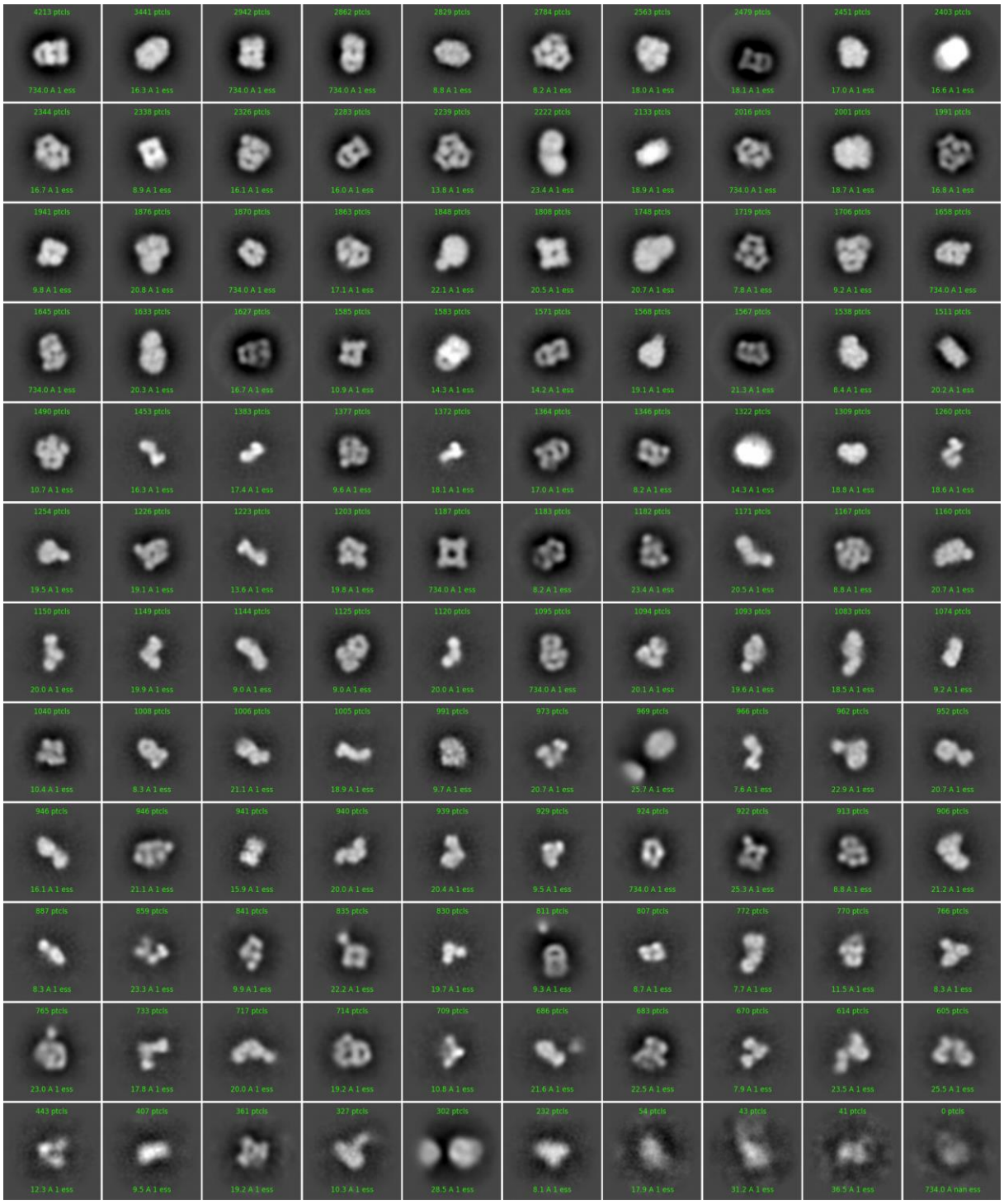

Figure 33. 2D classificaiton of apo-DynA particles after auto-picking via Relion software. All the particles are classified into 120 types. The box diameter is 100 pixels.

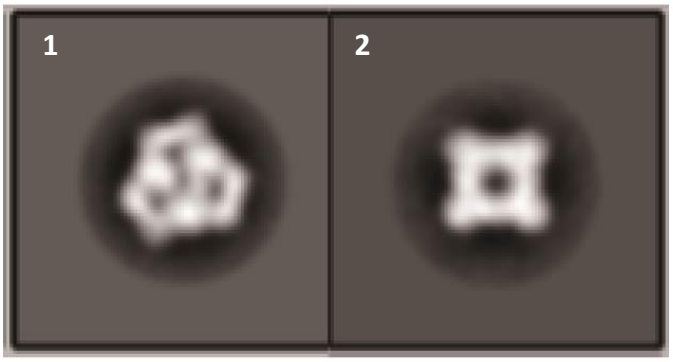

Figure 34. Representative patterns in 2D classification of apo-DynA particles after auto-picking via Relion software.

3.4 3D model generation of apo-DynA particles

Relion uses a Stochastic Gradient Descent (SGD) algorithm to generate a 3D initial model de novo from the 2D particles. This algorithm iteratively optimizes an objective function by computing approximate gradients and taking steps in the parameter space according to those gradients. It is used to quickly identify several low-resolution 3D structures consistent with the set of observed images. To obtain a more even angular distribution of particles in the low-resolution initial model, the max number of selected particles per class was set to 200. This randomly selected 200 particles from each class that was selected. For the subsequent SGD calculations, it is typically enough to use several to ten thousand particles. Using more might sometimes lead to worse results. Probably the essential thing to consider when selecting particles for SGD calculations is to include as many different views as possible. We set 16 different 2D classes for one 3D generation job, resulting in 16*200 = 3200 particles (**Figure 35**).

After selecting the 2D classes for the initial model, 153,713 good particles were used for the 3D classification, then four 3D classes were generated, and the refinement was done individually. To avoid the overfitting problem, a so-called gold-standard approach for refinement is implemented. It splits the data randomly into two halves and refines independent reconstructions against each half of the data set at every iteration to prevent the iterative build-up of noise. A resolution is estimated from the Fourier shell correlation (FSC) between the two independent half maps. The refined 3D map revealed novel structural details that were not observed in the starting model. In the case of model 1, class size was 50%, and the particle

number was 77,459; in the case of model 2, the class size was 12.8%, and the particle number was 19,778; in the case of model 3, the class size was 16.2%, and the particle number was 26,691; in the case of model 4, the class size was 21%, and the particle number was 29,785 (**Figure 36 – 39**). We can set the viewing angle for a Three-view density map plot in terms of azimuth and elevation, which indicates the distribution in the top, side, and bottom directions.

A

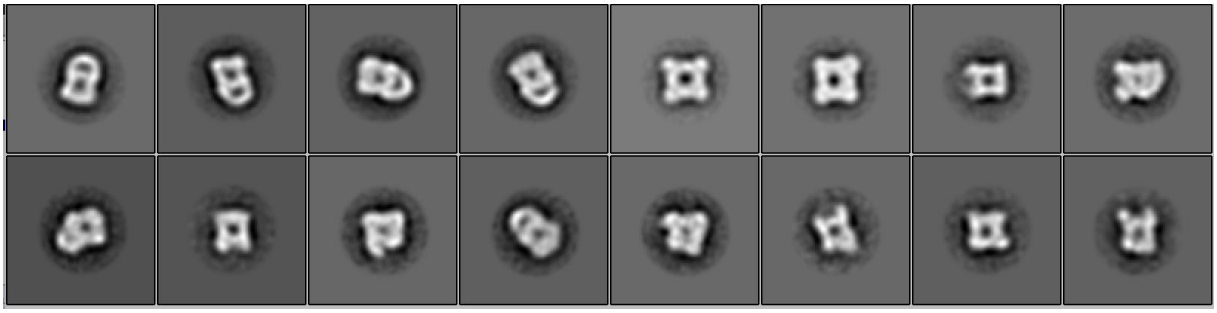

B

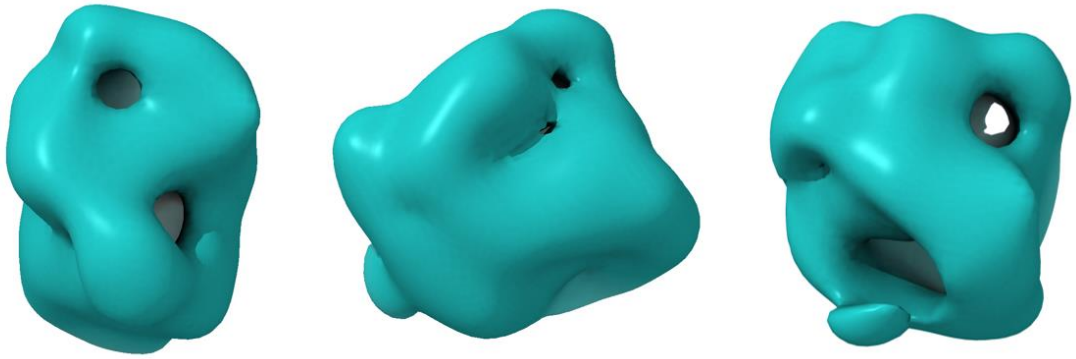

Figure 35. The 2D class averages (A) and the reconstructed initial model (B) which is reconstructed from 3200 particles in Relion 2.0.

Model 1:

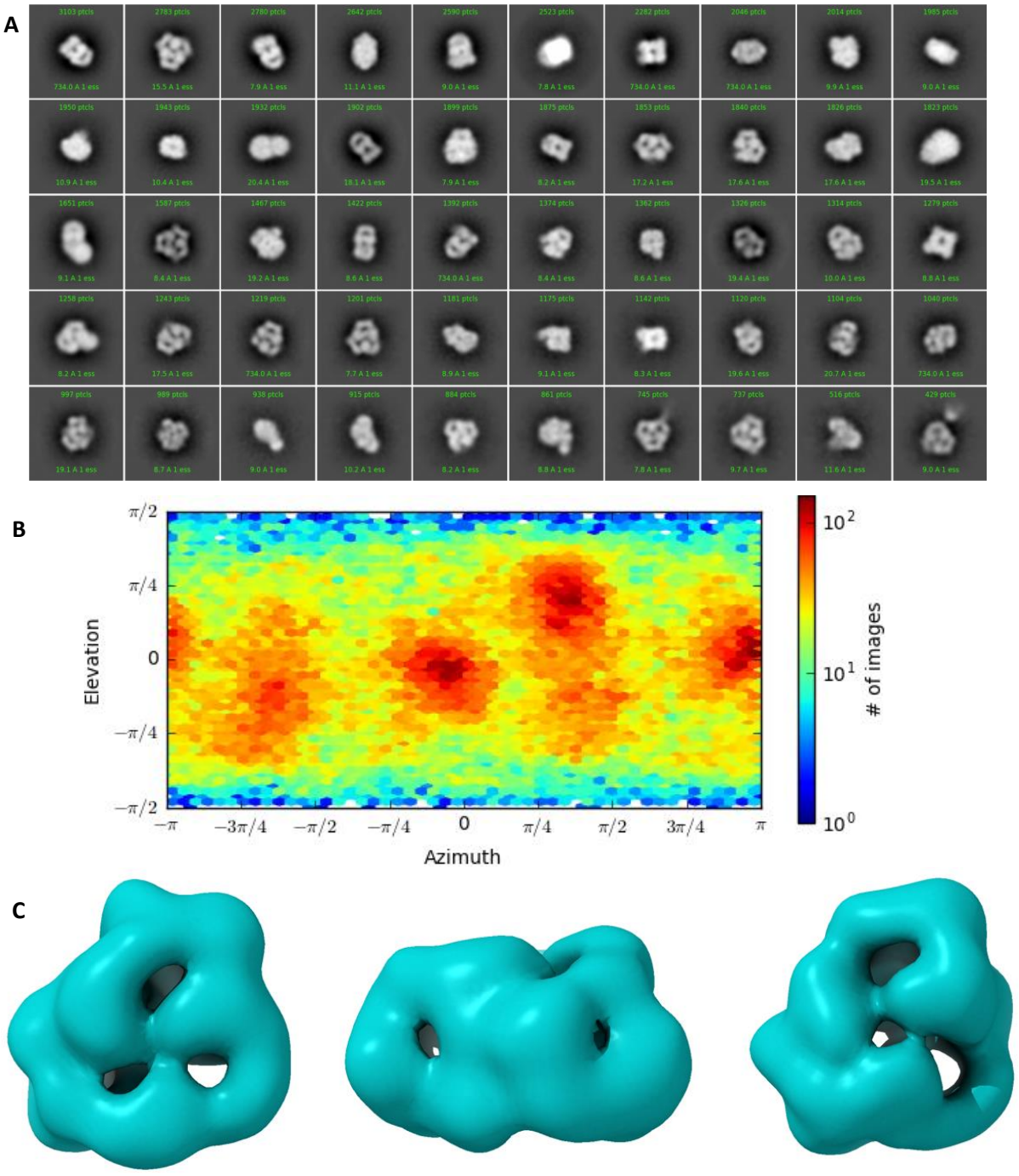

Figure 36. Structural characterization of Model 1. (A) 2D classes in model 1 that were automatically selected, similarly to the representative pattern 1 in Figure 34. (B) Three-dimensional density map of model 1 in terms of azimuth and elevation. (C) Three-view density map of model 1.

Model 2:

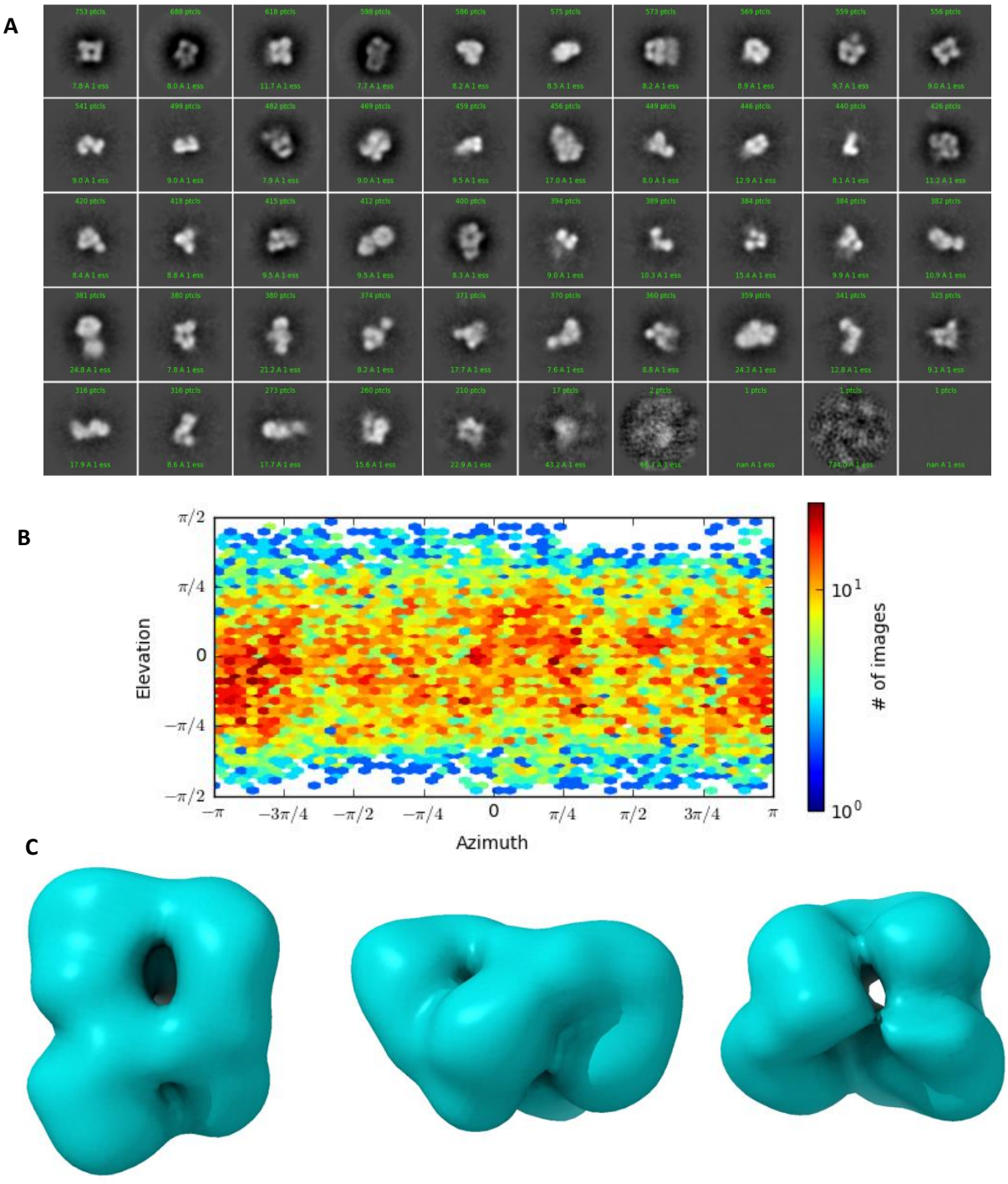

Figure 37. Structural characterization of Model 2. (A) 2D classes in model 2 that were automatically selected, similarly to the representative pattern 2 in Figure 34. (B) Three-dimensional density map of model 2 in terms of azimuth and elevation. (C) Three-view density map of model 2.

Model 3:

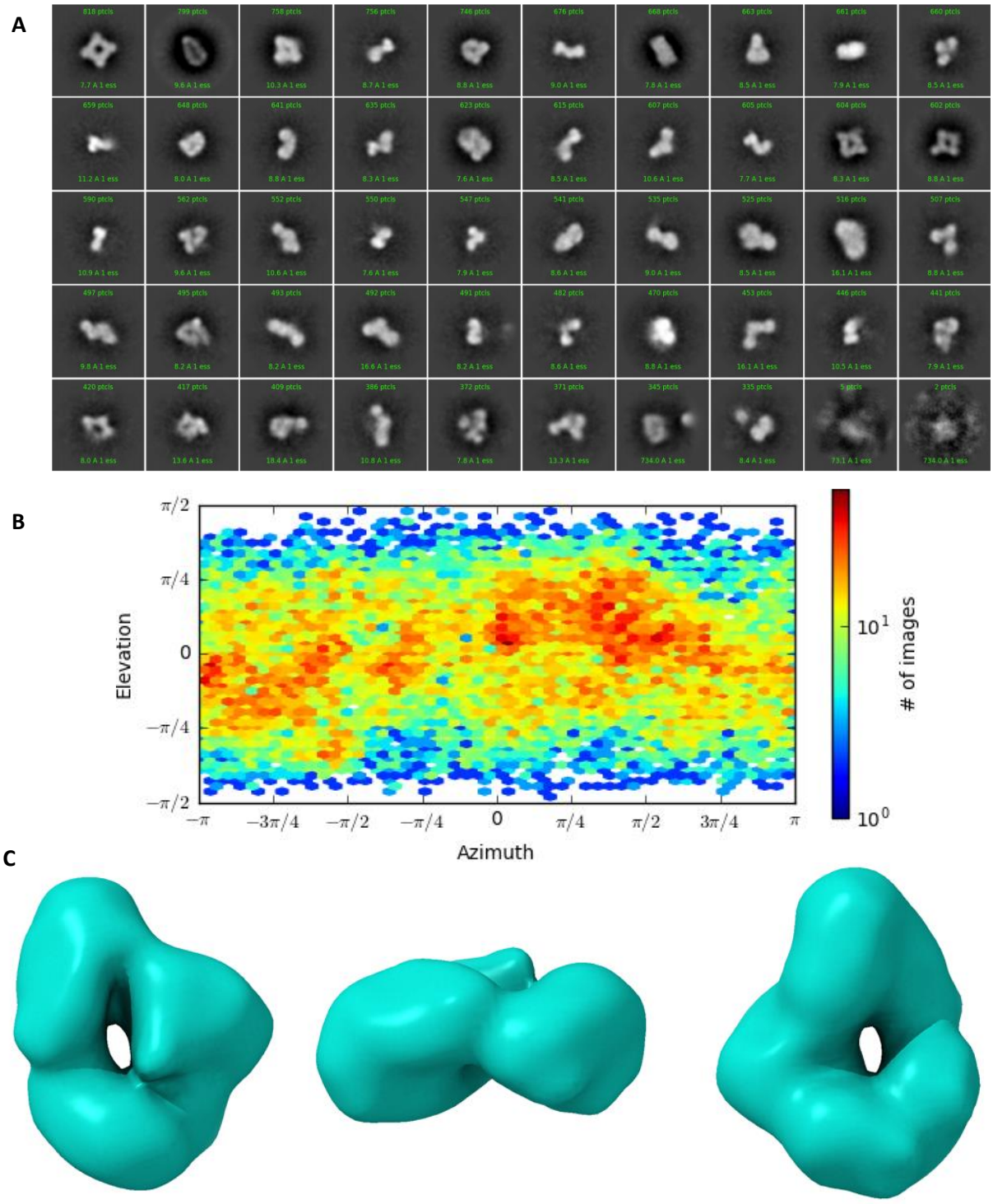

Figure 38. Structural characterization of Model 3. (A) 2D classes in model 3 that were automatically selected, similarly to the representative pattern 2 in Figure 34. (B) Three-dimensional density map of model 3 in terms of azimuth and elevation. (C) Three-view density map of model 3.

Model 4:

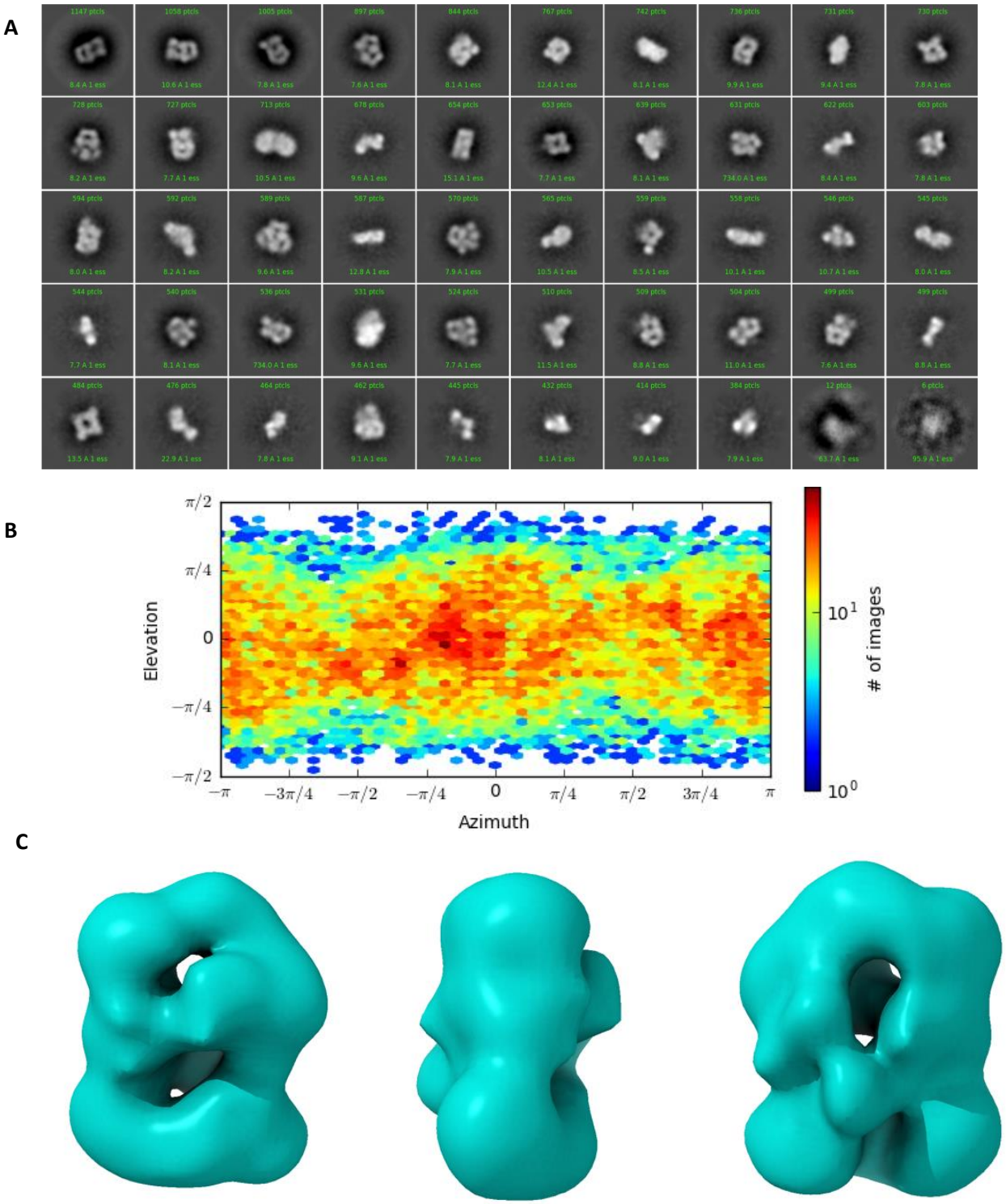

Figure 39. Structural characterization of Model 4. (A) 2D classes in model 4 that were automatically selected, similarly to the representative pattern 2 in Figure 34. (B) Three-dimensional density map of model 4 in terms of azimuth and elevation. (C) Three-view density map of model 4.

4 Bacteriophage resistance gene candidate screening

We aimed to use the *B. subtilis* gene knockout library ((Koo *et al.*, 2017) to screen for genes involved in phage resistance. Therefore, a growth curve assay was employed for screening. The addgene *B. subtilis 168* single-gene deletion library (kanamycin-resistant) (Koo *et al.*, 2017) was initially screened in the Tecan Infinite® 200pro Plate reader, and five knockout strains revealed a possible role in resisting phage infection. These strains were Δ*spo0A*, Δ*dagK*, Δ*ypmB*, Δ*aroB*, and Δ*clpC*. They were further tested with growth curve analysis with biological replicates in response to phage Φ29 (MOI = 1) and antibiotic nisin (30 µg/ml). All the strains had a sharper decrease (similar to Δ*dynA* strain) in response to nisin, compared to the WT strain (**Figure 40),** indicating that the presence of these genes could potentially be essential to rescue environmental stress-induced cells. In response to the phage infection, compared to WT, Δ*dagK*, Δ*ypmB*, and Δ*spo0A* had a steeper decrease in growth, as opposed to Δ*aroB* and Δ*clpC*. This indicated a possible role of DagK, YpmB, and Spo0A in phage resistance. Spo0A has been

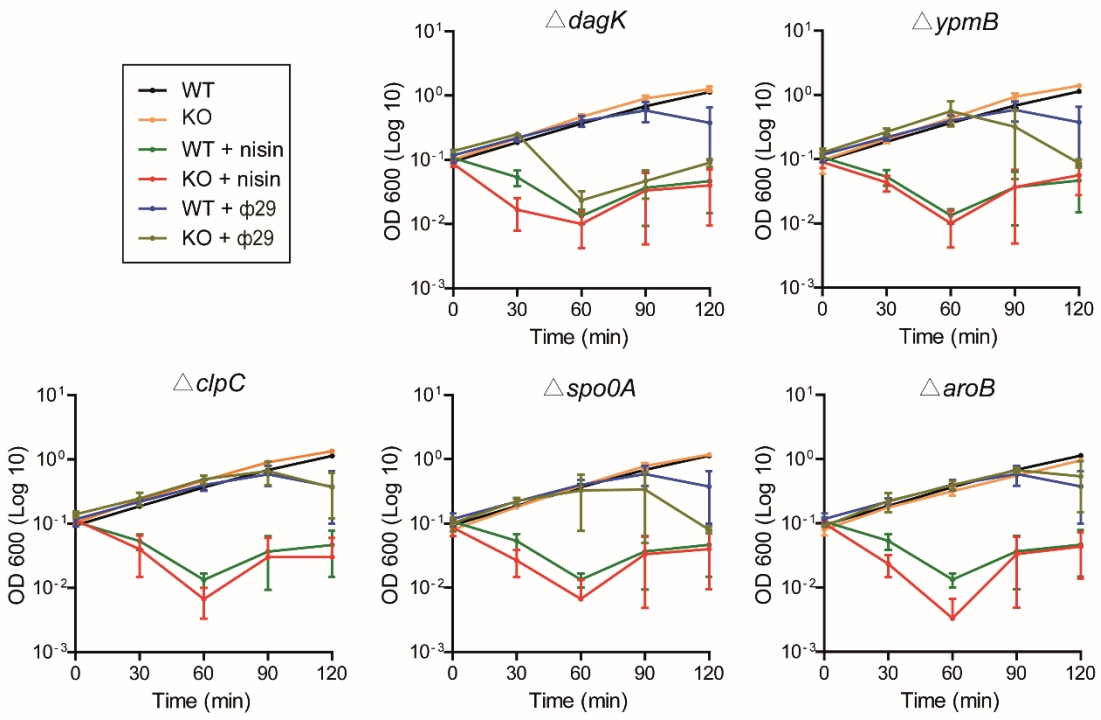

Figure 40. Growth curve analysis of the potential knock-out strains for Φ29 and nisin resistance. The analysis was done for Δ*dagK*, Δ*ypmB*, Δ*spo0A*, Δ*aroB*, and Δ*clpC*. Every knockout strain and the WT strain had an abrupt decrease in growth upon nisin exposure (red and green line) compared to that upon no exposure (yellow and black line), while every strain had a steeper decrease compared to WT upon phage exposure (brown and blue line). In the case of Δ*dagK*, the decline in growth upon phage stress was most pronounced, followed by Δ*ypmB* and Δ*spo0A* (brown line). Mean and standard error of the three replicates were shown.

previously reported to have a role in phage resistance. It blocks the transcription of genes from the early promoter of Φ29 and suppresses the lytic cycle and the development of the phage (Castilla-Llorente *et al.*, 2009a). The finding of Spo0A in this experiment demonstrated the reliability of the growth curve analysis experiment for screening. DagK and YpmB were further analyzed for their potential phage resistant functions.

4.1 Characteristics of DagK in phage resistance

DagK catalyzes the phosphorylation of diacylglycerol (DAG) into phosphatidic acid. It is a crucial enzyme involved in the production of lipoteichoic acid by reintroducing DAG formed from the breakdown of membrane phospholipids into the phosphatidylglycerol biosynthetic pathway (Jerga *et al.*, 2007). Quantitative plaque assays were performed with the wild-type *B. subtilis 168* and *dagK* gene knockout strains in response to phage Φ29 infection (**Figure 41A**). As compared to WT, the Δ*dagK* strain had more plaques, and they also appeared morphologically larger. To characterize the role of DagK in response to phage infection, several tests were performed. Firstly, the effect of Φ29 phage attachment was tested on *B. subtilis 168* WT and Δ*dagK* strain. After 10 minutes of mixing phages and bacteria, bacteria were isolated, and the phages attached to the bacteria were quantified on the plate of the *dynA*-knockout strain. Compared to WT with student *t*-test, there are twice as many phage particles attached to *ΔdagK* ($P = 0.007$) (**Figure 41B**). This indicated that DagK could have a role in protection from phage attachment. Next, a lysis test was performed to test the number of released phages from bacteria after one hour (**Figure 41C**). As compared to WT, more phage particles were released from Δ*dagK* cells to infect the surrounding bacterial population, which indicated that the phage lysed more Δ*dagK* cells within 1 hour ($P = 0.00018$ for WT 1h: Δ*dagK* 1h) (**Figure 41C**). The data at 0 h indicated that there were fewer external phages attach to the cells for the Δ*dagK* strain ($P = 0.003$ for WT 0 h: Δ*dagK* 0 h), suggesting that DagK had the effect of preventing phage attachment to cells. More cells of Δ*dagK* lysed after 1 hour, dramatically increasing the number of external phages ($P = 0.001$ for Δ*dagK* 0 h: Δ*dagK* 1 h; $P = 0.0005$ for WT 0 h: WT 1 h). This indicates that DagK delays or hinders the phage infection process, and ultimately manifests itself in the release of fewer phage particles. Besides, mitomycin assay was also performed with Δ*dagK* and WT strains to induce lysis of prophage SPβ to check whether more prophages could be induced into the lysis cycle in the bacteria without *dagK*. Indeed, after 2 hours of mitomycin C treatment, the Δ*dagK* strain was observed to have more plaques than WT (**Figure 41D**), indicating that DagK played a role in blocking the transformation of prophage to the lytic cycle. The qPCR assays were performed to quantify replicated phage DNA every 15 min, for up to 90

min after infection (**Figure 41E**). Compared with WT, the total amount of phage DNA was tripled in the case of Δ*dagK* at 90 min, suggesting that DagK might also affect phage replication or just more cells of Δ*dagK*. The external phage DNA amount in the case of Δ*dagK* was also approximately twice that of WT at 90 min after phage attachment. Inside of Δ*dagK* cells, phage DNA also showed a greater amount at 75 min. At 90 min, the internal phage DNA amount of Δ*dagK* converged and became similar to that of WT, suggesting that the phage DNA was released from the cell to the outside of the cell. All these results are evidence supporting a role of DagK in phage resistance.

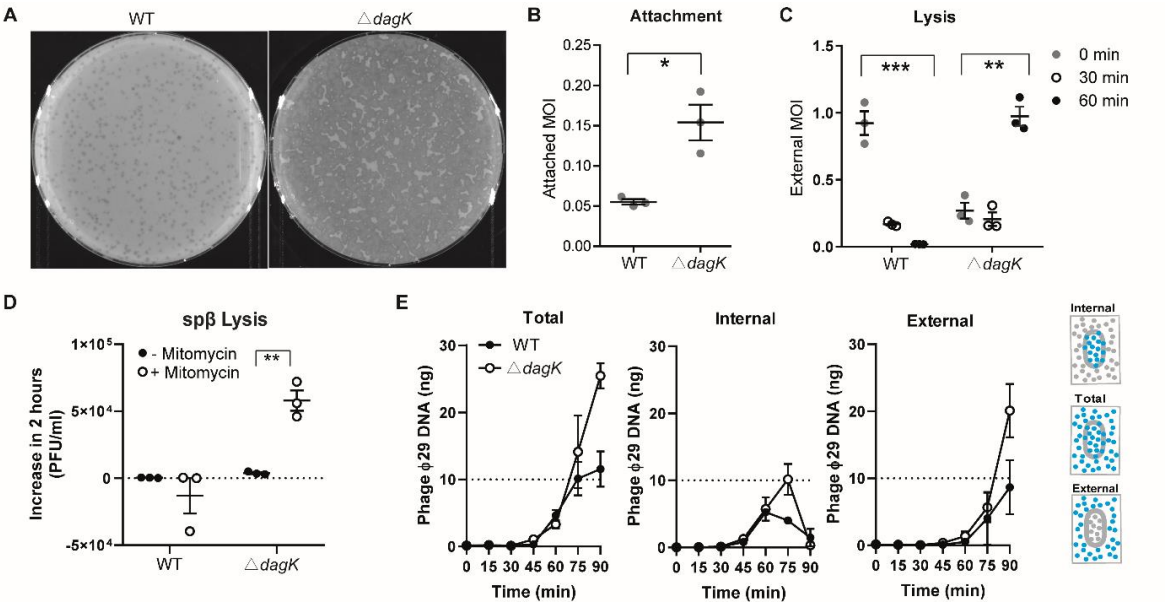

Figure 41. Characteristics of DagK in phage resistance. (A) Deletion of *dagK* produces larger plaques. There are equal numbers of bacteria and phage Φ29 on each LB plate. (B) Attachment test with phage Φ29. MOI of attached phages after 10 min-infection for WT and Δ*dagK* was plotted. Compared to WT, more phages were attached to the cells of Δ*dagK*. (C) Lysis Test with phage Φ29. MOI of external phages at 0 min- and 60 min- infection for WT and Δ*dagK* was plotted. Δ*dagK* strain releases more phages as compared to WT. (D) Mitomycin lysis test of prophage SPβ. Mitomycin was added in bacterial cultures for inducing lysis of the prophage SPβ. This was followed with quantitative spot assay to test the released phage titers in the supernatant. This revealed that Δ*dagK* had much higher number of plaques after mitomycin treatment than WT. (E) The qPCR analysis of the trend of phage Φ29 DNA. The total phage DNA includes the phage DNA in bacteria, on the cell surface, and outside the cell. The amount of internal phage DNA is the amount of phage DNA in bacteria and on the cell surface. The external phage DNA is the phage DNA resuspended outside the cell. External phage DNA and internal phage phage DNA was separated by centrifugation. Phage DNA are quantified every 15 min, for up to 90 min after infection for the trend of total, internal and external phage DNA. The phage DNA of Δ*dagK* strain replicates faster.

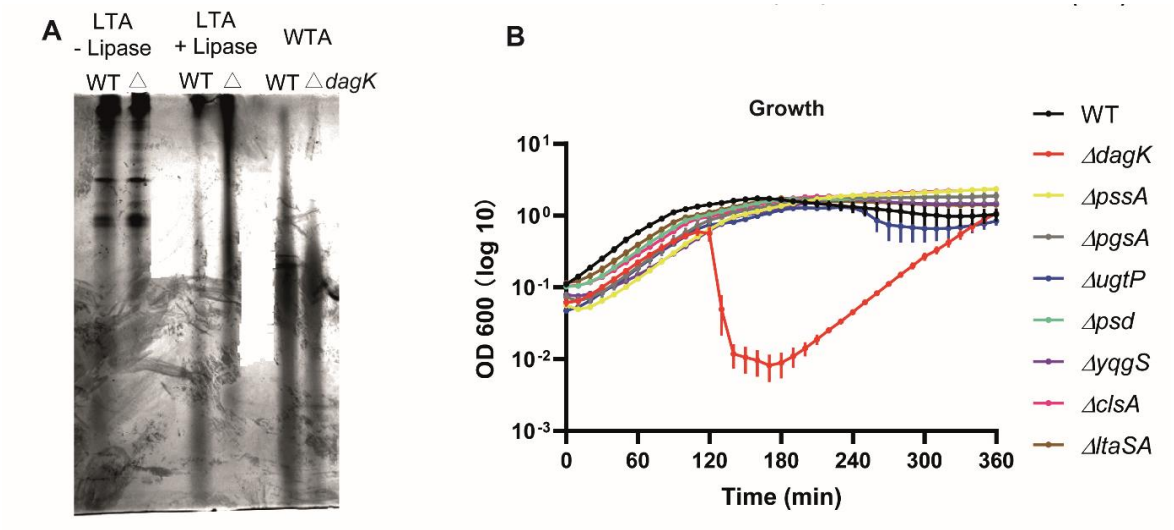

Figure 42. Teichoic acid profile of *B. subtilis 168* strains and growth curve analysis for genes in the lipoteichoic acid biosynthesis pathway. (A) Teichoic acid profile of *B. subtilis 168* WT and *⊿dagK* strains. For both the strains, wall teichoic acids (WTA), lipoteichoic acids (LTA) and LTA after lipase treatment are shown. (B) Growth curve analysis of different knockout strains for genes in the lipoteichoic acid biosynthesis pathway, in response to phage Φ29 infection. The growth was measured as the absorbance at 600 nm over 360 min. *⊿dagK* had a steeper decrease in growth than WT. Other gene knockouts tested were behaved similar to WT, except that *⊿ugtP* has a mild decrease. Mean and standard error of the three replicates are shown.

DagK plays a role in lipoteichoic acid biosynthesis. Therefore, we hypothesized that DagK helps cells resist phage infection stress by affecting lipoteichoic acid biosynthesis. Firstly, we checked the teichoic acid profiles of *B. subtilis 168* WT and Δ*dagK* strains. Teichoic acids are anionic polyphosphate polymers that are embedded in the cell wall (Wall teichoic acids, WTA) and cell membranes (Lipoteichoic acids, LTA) of Gram-positive bacteria. WTA is covalently linked to the peptidoglycan layer, and LTA is anchored to the cell membrane via a diacylglycerol moiety. To extract crude WTA of WT and Δ*dagK*, the peptidoglycan sacculus was first isolated, and WTA was then liberated by hydrolysis with sodium hydroxide. LTA of WT and Δ*dagK* was extracted with 1-butanol and treated with lipase to prevent aggregation. There was no significant difference between the WTA profiles of WT and Δ*dagK* (**Figure 42A**). The LTA profiles of the two strains before lipase treatment also showed no significant differences. After lipase treatment, the abundance of low molecular weight LTA in WT was higher, while the abundance of high molecular weight LTA in Δ*dagK* strain became higher than WT. To further test a possible role of LTA in phage resistance, we studied other genes involved

in LTA synthesis for possible effects on phage infection. All gene knockout strains (Δ*pssA*, Δ*pgsA*, Δ*ugtP*, Δ*psd*, Δ*yqgS*, Δ*clsA*, and Δ*ltaSA*) were taken from *B. subtilis* single-gene knockout library (Hashimoto *et al.*, 2013). Bacteriophages Φ29 (MOI = 1) were added to the bacterial cultures of each species (OD = 0.1) to monitor the effect of phage infection on these knockout strains (**Figure 42B**). The Δ*dagK* strain had an abrupter decrease in growth as compared to WT. In addition, recovery of Δ*dagK* was much slower as compared to WT. In contrast, all other knockout strains react similarly to phage infection as WT. The Δ*ugtP* strain had a mild decrease in growth, but not as much as the Δ*dagK* strain. Compared with *dagK*, other genes tested in the lipoprotein acid biosynthetic pathway may not be involved in phage resistance, which also means that DagK-induced phage resistance may not be generated through the pathway.

4.2 Characteristics of YpmB in phage resistance

A auantitative plaque assay was performed with the wild-type *B. subtilis 168* and *ypmB* gene knockout strains in response to phage Φ29 infection (**Figure 43A**). As compared to WT, Δ*ypmB* had many more plaques, and they also appeared morphologically larger. To characterize the role of YpmB in response to phage infection, several tests were performed as the study for DagK. Firstly, the effect of Φ29 phage attachment was tested on *B. subtilis 168* WT and Δ*ypmB* strain. After 10 minutes of mixing phages and bacteria, bacteria were isolated, and the phages attached to the bacteria were quantified on the plate of the *dynA*-knockout strain. Compared to WT, there are fewer phage particles attached to Δ*ypmB* **(Figure 43B**). Next, a lysis test was performed to test the number of phages released from bacteria after one hour (**Figure 43C**). As compared to WT, fewer phage particles were released from Δ*ypmB* cells to infect the surrounding bacterial population. The data at 0 h indicated a similar number of external phages of Δ*ypmB* not immediately attached to the cells. After 1 hour of lysis, *ΔypmB* cells showed similar results as WT, making the number of external phages similar. Also, mitomycin assay was performed with Δ*ypmB* and WT strains to induce lysis of prophage SPβ to check whether more prophages could be induced into the lysis cycle in the bacteria without *ypmB*. In fact, the *ΔypmB* strain was not observed to have more plaques than WT after mitomycin treatment (**Figure 43D**). The qPCR assay was performed to quantify replicated phage DNA every 15 min, for up to 90 min after infection (**Figure 43E**). The total, internal, and external phage DNA of Δ*ypmB* were not more than WT from 45 min to 90 min. YpmB showed resistance to phage infection in the plague assay, but this resistance effect was not shown in the rest of the analysis. It is probably because YpmB does not affect the phage infection within 90 minutes (the

attachment, lysis, and qPCR tests need less than 90 min), but after 90 minutes (the plague assay need hours). In short, the effect of YpmB against phage infection needs further investigation.

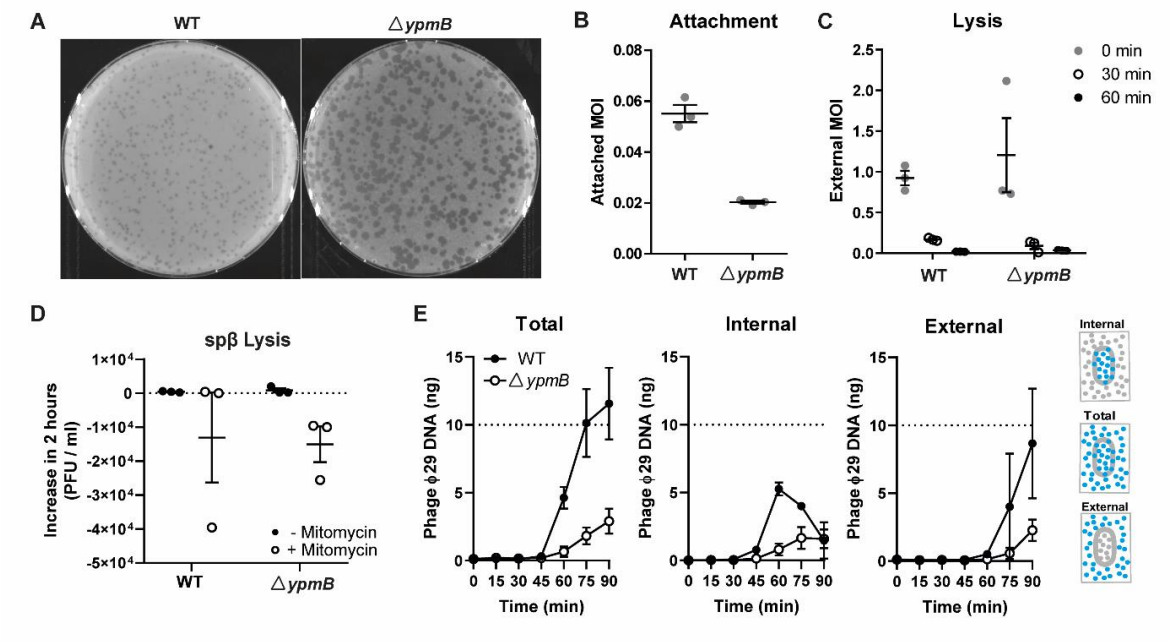

Figure 43. Characteristics of YpmB in phage resistance. (A) Deletion of *ypmB* produces larger plaques. There are equal numbers of bacteria and phage Φ29 on each LB plate, and the result is biologically repeated. (B) Attachment test with phage Φ29. MOI of attached phages after 10 min-infection for WT and Δ*ypmB* was plotted. Compared to WT, less phages were attached to the host of Δ*ypmB*. (C) Lysis Test with phage Φ29. MOI of external phages at 0 min- and 60 min- infection for WT and Δ*ypmB* was plotted. Δ*ypmB* strain releases similar phages as compared to WT. (D) Mitomycin lysis test of prophage SPβ. Mitomycin was added in bacterial liquid for inducing lysis of the prophage SPβ. This was followed with quantitative spot assay for the released phage titers in the supernatant, which showed that Δ*ypmB* had similar number of plaques after mitomycin treatment than WT. (E) The qPCR analysis of the trend of phage Φ29 DNA. The total phage DNA includes the phage DNA in bacteria, on the cell surface, and outside the cell. The amount of internal phage DNA is the amount of phage DNA in bacteria and on the cell surface. The external phage DNA is the phage DNA resuspended outside the cell. External phage DNA and internal phage phage DNA are separated by centrifugation. Phage DNA are quantified every 15 min, for up to 90 mins after infection for the trend of total, internal and external phage DNA. The phage DNA of Δ*ypmB* strain replicates slower than that of WT. Mean and standard error of the three replicates were shown.

Discussion

1 DynA mediates full membrane fusion

The *B. subtilis* DLP DynA is a head-to-tail fusion of two DLP subunits and was shown to dimerize *in vitro* (Burmann *et al.*, 2011). We have shown earlier with *in vitro* and *in vivo* experiments that DynA can bind and tether membranes in trans (Burmann *et al.*, 2011). Evidence was provided that DynA plays a protective role when cells were challenged with membrane pore-forming agents such as antibiotic nisin or phages (Sawant *et al.*, 2016). In the presence of nisin, DynA aggregated into punctate foci in the cell membrane *in vivo* where it is proposed to seal membrane pores. Based on these phenotypes, it was suggested that DynA might function as a fusogen in membrane maintenance and repair by achieving tethering and sealing. These cellular roles would require the fusion of both membrane leaflets, and hemifusion would not be sufficient to repair damaged membranes. Therefore, we set out to investigate the fusion activity of DynA in detail with a series of *in vitro* fusion assays. Using FRET-based fusion assays, we provide evidence here that DynA can promote the full fusion of membranes. However, membrane fusion is a slow process *in vitro*. Specifically, docking induced by DynA was achieved within 5 min and then kept stable, whereas the transition from docking to hemifusion required hours. After the vesicles in the cluster completed hemifusion, they gradually underwent full fusion. Subsequently, the fusion pores began to enlarge, followed by content exchange through the enlarged fusion pore, resulting in the appearance of large vesicles. Since the time for the content mixing to reach the maximum was more than two hours later than the lipid mixing at 37°C, we believe that the formation and expansion of the fusion pore is a slow process at least under the observed *in vitro* situation. This slow membrane fusion is somewhat difficult to combine with the role of DynA in membrane protection after pore formation. The membrane potential *in vivo* would collapse when membrane pores are not quickly and effectively sealed. Thus, we hypothesize that although DynA can independently achieve membrane fusion *in vitro*, it may require partner proteins to accelerate it *in vivo*. We reasoned that a protein encoded next to the *dynA* gene (*ypbS*) might involve the fusion process. Therefore, we purified YpbS and added it to lipid mixing assays but did not observe any effect. The emerging possibility of partners of DynA in membrane fusion is reminiscent of soluble N-ethyl maleimide sensitive factor attachment protein receptors (SNAREs) (Wu *et al.*, 2017). In SNARE-mediated membrane fusion, several proteins are involved at various steps of membrane fusion (Wu *et al.*, 2017). SNARE-mediated vacuole membrane fusion is coupled to nucleotide hydrolysis in the Sec17 and Sec18 proteins. Interestingly, Sec17 and Sec18 act

nucleotide hydrolysis independent in membrane fusion (Song *et al.*, 2017) but requires ATP hydrolysis to disassemble the SNARE complex (Ungermann *et al.*, 1998). Sec17 becomes essential for fusion when conditions such as membrane composition or SNARE complex assembly are not ideal (Harner & Wickner, 2018). However, an important difference is that SNARE-mediated membrane fusion requires transmembrane segments, while DynA is the only membrane associated.

Many bacteria encode at least two DLPs, and there is increasing evidence that bacterial DLPs act as heterodimers. DynA is an unusual DLP that it arose from a gene fusion and, hence, the protein is a two-headed DLP, indicating that intimate contacts in bacterial DLP heterodimers are likely necessary for correct function. The D1 part of DynA shows a higher affinity for membranes than D2, which is identical to the assumption that DynA is supposed to insert with a paddle domain (as NosDLP) in the D1 part of the protein for membrane binding. Comparison of the activity of D1 with full-length DynA, it becomes obvious that even though the degrees of membrane fusion are similar in the beginning 1 hour, but the stability of the D1-tethered vesicles decreases rapidly over time, resulting in differences in membrane fusion efficiency between DynA and D1 subunit. We, therefore, propose the role of D2 in stabilizing DynA tethered vesicles (**Figure 44**). Further support for the idea stems from bacterial two-hybrid data in which D2 self-interaction is stronger than D1 self-interaction and D1/D2 interaction (Burmann *et al.*, 2011). The optimal activity for membrane full fusion is only achieved with the full-length protein. DynA might therefore exhibit similar characteristics compared to the *C. jejuni* DLP1/DLP2 heterodimer (Liu *et al.*, 2018).

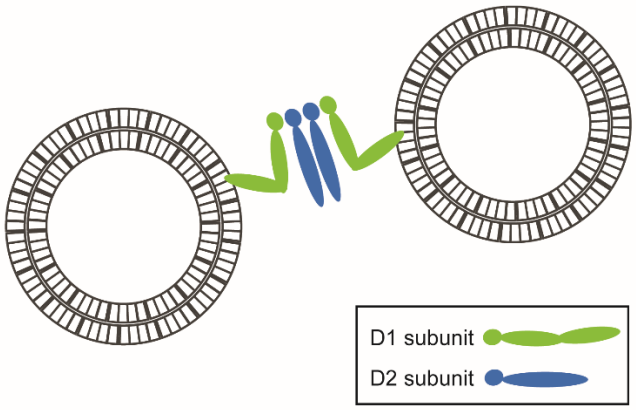

Figure 44. A cartoon of the proposed model of DynA-mediated liposome tethering. D1 subunit of DynA shows higher affinity for membranes and D2 subunit shows stronger self-interaction for stabilizing tethered membrane.

It is suggested that the first step of fusion-through-hemifusion is fusion pore opening, and this step is limited by a larger free energy barrier than the induction of hemifusion (Risselada *et al.*, 2014, Kweon *et al.*, 2017, Chernomordik & Kozlov, 2005). This may hint to the role of GTP hydrolysis in providing the energy to catalyze the process from hemifusion to full fusion. Our combination analysis of lipid dequenching and content FRET indicates that the addition of GTP does not result in differences in content mixing to lipid mixing. Still, we cannot rule out that the *in vitro* system lacks essential cellular components. In eukaryotes, dynamins and DLPs engage in nucleotide-dependent membrane remodeling activities. However, DynA is independent of nucleotide hydrolysis in membrane binding, provoking the question of why these enzymes have a measurable GTP hydrolysis activity. In lipid and content mixing assays, the addition of nucleotides does not accelerate DynA-induced membrane fusion. This is in line with observed antiviral effects of Mx proteins, which act GTP-independent on hepatitis and HIV viruses (Yu *et al.*, 2008). Additionally, under lower temperature, GTP binding or GTP hydrolysis delayed DynA-induced membrane fusion, indicating a regulatory role for GTP binding and hydrolysis.

Interestingly, we observed that removal of DynA via proteinase K treatment leads to a rapid increase in content mixing compared to lipid mixing. We assume that DynA assembly on opposing membranes leads to an energetically unfavorable membrane deformation and removal of membrane-bound DynA would allow efficient membrane fusion.

Further, we observed that DynA binds best to membranes composed of a mixture of PG and PE in ratios similar to the phospholipid composition in the *B. subtilis* membranes. The essentiality of PG for DynA membrane binding hints to electrostatic interactions requiring positively charged amino acid side chains in DynA. However, despite extensive mutagenesis, we were not able to identify these putative residues, yet. The cone-shaped lipid PE has also been suggested essentially for mitochondrial fusion (Daste *et al.*, 2018) since it is enriched at mitochondrial contact sites (Ardail *et al.*, 1990). We also found that cardiolipin increased fusion efficiency, but only at high concentrations between 30 - 40%. CL concentration *in vivo* within the cell membrane is lower. However, we cannot rule out that CL may enrich in deformed membrane areas and that this local increase may positively affect membrane fusion. In general, lipids with smaller head-groups seem to have a positive effect on DLP mediated membrane fusion. Physiological membrane composition has also been shown to be important for the functional reconstitution of SNARE-mediated membrane fusion (Fukuda *et al.*, 2000, Mima *et al.*, 2008). Similar results are obtained for SNAREs that higher ambient temperature can promote membrane fusion (Jackson & Chapman, 2008, Bowen *et al.*, 2004). Likely, the increased

dynamics of the phospholipids render the membrane at 37°C more fluid than at 24°C and thus may allow faster membrane fusion to occur.

In summary, we have shown that the *B. subtilis* DLP DynA mediates full membrane fusion and that specific lipids such as PG are required to exert its function effectively. While our data are in line with the role of DynA in membrane surveillance and protection against pore-forming agents, the observed time scales for full fusion suggest that additional factors are associated with DynA-mediated membrane fusion *in vivo*.

2 Characteristics of DynA resistance to membrane rupture

The dynamin superfamily includes classic dynamins and dynamin-like proteins (DLPs) involved in membrane remodeling. Classical dynamins play a role in vesicle trafficking by catalyzing membrane fission in eukaryotes. In contrast, DLPs may catalyze membrane fusion or membrane fission and are involved in cell processes such as cell division, organelle homeostasis, membrane surveillance, and repair. Bacteria resist various environmental stresses in their natural habitats, such as temperature, osmolality, antibiotic, nutritional restriction, and phage infection, so they need to constantly reshape their cell membranes to act as physical barriers to protect themselves from adverse environmental effects. Some bacterial DLPs are associated with resistance to membrane rupture. The *E. coli* LeoABC DLPs play a role in potentiating virulence through membrane vesicle associated toxin secretion (Michie *et al.*, 2014). The *Mycobacterium tuberculosis* DLP IniA confers drug tolerance to both isoniazid and ethambutol (Colangeli *et al.*, 2005). The *B. subtilis* DLP DynA can achieve membrane full fusion and is involved in bacterial resistance against biotic and abiotic membrane stress. Under the pressure of antibiotic nisin that forms the membrane pores, the hyperdynamic DynA can quickly assemble into static and large clusters on the cell membrane *in vivo*, thereby interfering with cell death and promoting rapid recovery of the bacterial population. It was proposed that DynA oligomerizes at the site of membrane damage in static foci, tether the membrane, and catalyze fusion to close the pores. Additionally, it was also observed that the absence of DynA increased cell sensitivity to phage infections by the lytic phage ϕ29 and the lysogenic phage SPβ that and the number of plaques of knock-out strains was significantly more than wild-type strains.

Here, we analyzed the effect of DynA on phage injection in detail. The absence of DynA increased not only in number but also in the area of the plaque. A growth curve analysis was performed to observe the growth of bacteria with different expression levels of DynA after lytic

phage infection. Strains with lower DynA expression are more sensitive to cell lysis, indicating that DynA acts on the cell's resistance to phage infection and is proportional. After that, we employed fluorescent microscopy observing the cellular localization of DynA after cells were treated with bacteriophage. Co-localization analysis of DynA with phages was performed to answer if DynA prevents phage infection by repairing phage-induced membrane damage during DNA injection. In our study, the fluorescent DynA-GFP protein clusters did not strictly correspond to the fluorescently labeled phages. The fluorescently labeled phages did not strictly correspond to the DynA protein clusters. We observed some non-colocalized phages and DynA clusters. These results indicated that DynA might achieve phage resistance in other ways. Besides, we employed phage attachment and lysis test. We knew that the expression level of DynA did not significantly affect the phage attachment, but it has a significant effect on the amount of phage that lysed the cells in the late stage of infection, and DynA mainly prevented the assembled progeny phage from being released from the cell. This result was also verified by real-time quantitative PCR. The increased expression of DynA caused a higher proportion of phage DNA to be trapped in the cells in the late stage of infection. Lysogenic SPβ lysis test showed the quantity of prophages induced into lytic cycle. In this experiment, DynA did not have the opportunity to act on the steps of phage attachment and phage replication. The result was that DynA prevented SPβ-induced cell lysis. In our subsequent fluorescence microscopy and single-molecule tracking experiments, DynA was observed to play a role in the late stage of phage infection and hinder cell lysis at the single-cell level. At 30 min to 1 h after phage infection. The phage attachment and DNA injection completed, and the highly dynamic DynA were employed to cluster on the membrane and became stable, likely maintaining the integrity of the cell membrane. The response of DynA to phage injection is similar to its response to the antibiotic nisin. Except that the response to nisin is quick, while the response to phage is lagging. This is likely because nisin damages cell membrane integrity more timely, and the large-scale destruction of the cell membrane by phage occurs in the last step of the phage infection cycle. The conclusion is that DynA can aggregate and remain stable to prevent progeny phages from lysing the host cell membrane.

Based on the results, we proposed a resistance model of DynA against ϕ29 **(Figure 45)**. When the phage is attached to the bacteria, DynA is evenly distributed on the cell membrane. Then, the phage DNA is injected into the bacteria, and the replication of the phage DNA is followed. In the process of phage DNA transcription, translation, and phage assembly, the dynamics of DynA did not change until that phage assembly is completed, and the progeny phages begin to lyse the cell membrane. At this time, DynA aggregate into clusters, hindering the rupture of the

cell membrane, and this process is accompanied by the separation of the parent phage and the contraction of the bacteria. This process delays cell lysis and interferes with efficient phage dispersal.

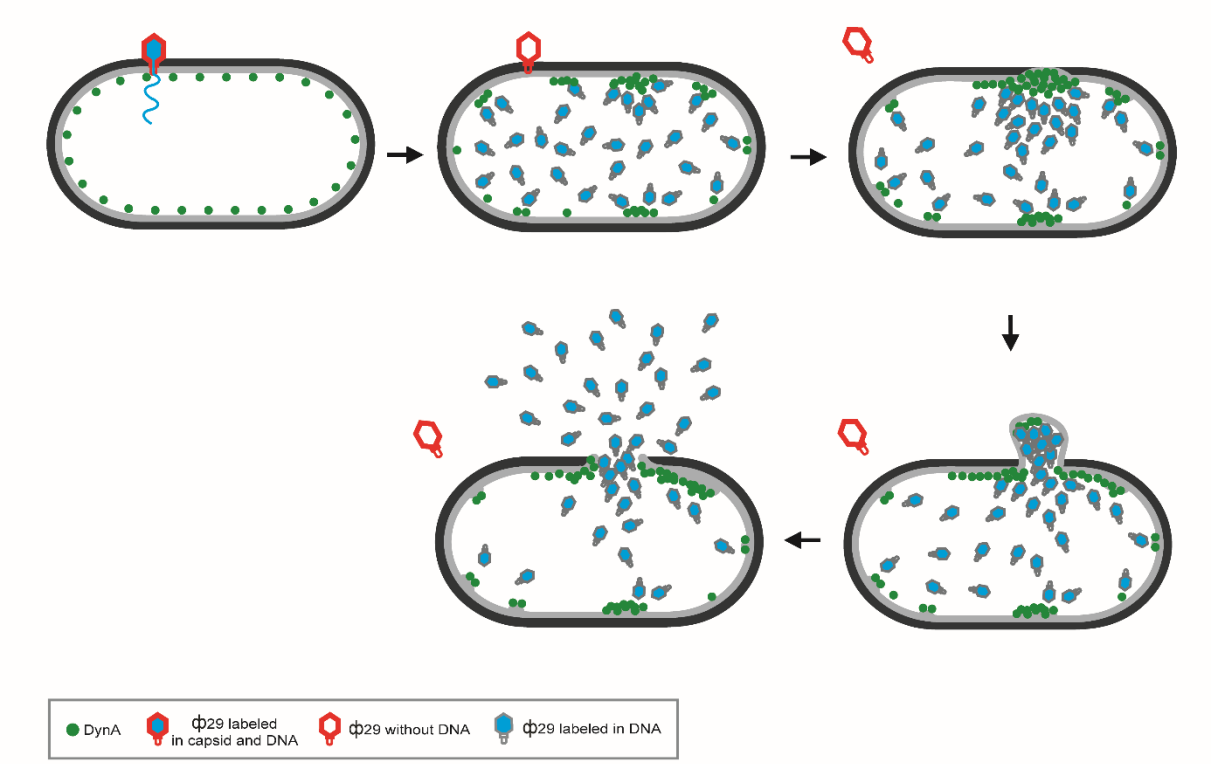

Figure 45. A cartoon of the proposed model of DynA blocking phage infection.

We also employed fluorescent microscopy observing the cellular localization of DynA after cells were treated with antibiotic nisin. When antibiotic nisin was fluorescently labeled, and DynA-GFP was overexpressed with xylose induction, we observed where the nisin fluorescent signal was highly concentrated, the higher the degree of clustering of DynA-GFP, and where the nisin fluorescent signal was not dense, DynA-GFP could be more uniformly distributed. When the concentration of nisin was changed, the number of DynA clusters per cell also changed. Specifically, the higher the nisin concentration, the more DynA clusters. However, the more basic localization relationship between nisin and DynA clusters is uncertain. In this regard, we hypothesize that when more nisin is attached to the cell, the membrane pressure of the cell is greater, and corresponding DynA clusters will be generated at the nisin attachment site to resist the membrane lysis caused by nisin. In simple terms, DynA is hypothesized to prevent nisin-induced cleavage. To verify this hypothesis, we performed a co-localization analysis of the nisin and DynA clusters. The over-expressed DynA-Dendra2 clusters did not strictly

correspond to the fluorescently labeled nisin, and the fluorescently labeled nisin did not strictly correspond to the DynA-Dendra2 clusters. There are some independent nisin particles and DynA clusters. Nisin displays a unique pore-forming activity against bacteria which is known to be enhanced in the presence of lipid II. In addition to generation of pores, nisin is known to inhibit cell wall biosynthesis by interrupting the peptidoglycan production. An alternative mechanism of bactericidal action of nisin involves the segregation and loss of lipid II. It is also reported that lipid II independent antimicrobial of mechanism of nisin depends on its crowding and degree of oligomerization (Prince *et al.*, 2016). Therefore, whether each nisin cluster can cause membrane pores is uncertain. This may be the reason why DynA and nisin clusters are not strictly co-localized.

3 Towards a DynA structure

In *B. subtilis*, the gene DynA encodes a two-headed DLP, D1 subunit, and D2 subunit. D1 subunit of *B. subtilis* DynA shows strong membrane binding *in vivo* and *in vitro*, whereas the D2 subunit does not. The combination of two heterogeneous DLPs of *B. subtilis* DynA is reminiscent of mammalian OPA1L/OPA1S (Alavi & Fuhrmann, 2013) and Mfn1/ Mfn2 (Ishihara *et al.*, 2004), *Streptomyces* DynA/DynB (Schlimpert *et al.*, 2017), and *Campylobacter jejuni* DLP1/DLP2 (Liu *et al.*, 2018), which perform membrane-related cellular activities through paired heterologous DLPs. D1 subunit of DynA is similar to the long isoform of OPA1 (OPA1L), Mfn1, DynB, and Cj-DLP1 that the DLPs in pairs show a dominant role in membrane binding and tethering. The DLPs alone is enough for achieving membrane fusion. However, the another DLPs in pairs show much lower (Ishihara *et al.*, 2004, Tondera *et al.*, 2009, Schlimpert *et al.*, 2017). In addition, the tendency of heterodimerization *in vitro* is even stronger than that of homodimerization for Mfn1/Mfn2 and DynA/DynB pairs (Li *et al.*, 2019, Schlimpert *et al.*, 2017). The recently solved crystal structure of *C. jejuni* DLP1/DLP2 provides a direct mechanism for the tethering of the opposing membrane by a BDLP pair (Liu *et al.*, 2018). The *C. jejuni* DLP1/DLP2 pair assembles in a stoichiometry of 2:2, with the DLP2 protein forming a central dimer and DLP1 positioned on either side (Bramkamp, 2018). The oligomerization surface of DLP1 and DLP2 is located in their GTPase domain. The minimal functional unit of DLP1/DLP2 is a tetramer, supporting earlier observations that the *B. subtilis* DynA is dimeric (Burmann *et al.*, 2011) and thus also consists of four DLP-like subunits. Therefore, the structure of the *C. jejuni* DLP1/DLP2 pair is a suitable reference to predict the structural characteristics of DynA.

In the purification of DynA, the protein was concentrated in the vicinity of 440 kDa by size exclusion chromatography. The molecular weight of DynA is 137 kDa, so most of the polymers in the sample were trimers, and the rest might be dimers or tetramers. After this, the sample was analyzed in the left peak and observed under the electron microscope with negative staining. The particles in the obtained micrographs were mainly based on the representative pattern 1 (**Figure 34**), similar to the 3D model 1. There were also many particles based on the representative pattern 2, which was similar to the 3D model 2/3/4. The first pattern was a hexagonal structure, which was presumed to be composed of six DLPs, while the pattern 2 was a quadrilateral structure, which was presumed to be composed of four DLPs. Therefore, we speculated that the pattern 1 was a trimer of DynA and the second pattern was a dimer of DynA. By comparing the second pattern with the Dj-DLP1/DLP-2 tetramer structure, the latter's GTPase domains were located at the center, and the stalks extend outward. In the pattern 2, GTPases were likely external, while stalks connected inward. The number of high-quality micrographs in this study was insufficient, the defocus degree of the pictures was high, and there were multiple polymers in the samples, which interfered with the data analysis. The follow-up experiments, fitting the predicted DynA structure based on the Cj-DLP1/DLP2 or NosDLP structure to the 3D model surfaces will help us understand more about the samples. Still, the key is how to improve the protocol to get more reliable and single polymer-contained samples. Further experiments should be addressed: 1. SEC-MALS test the polymerization of the samples, select the sample that contains a relatively single polymer-contained sample; 2. Replace a gel-filtration column so that the samples located around 440 kDa can be separated in a larger range, to obtain the sharper peak; 3. Purified protein can be mixed with liposome to observe the structure of protein-lipid tubing. The liposome tube induced by BDLP has been observed by electron microscopy (Low & Lowe, 2006), suggesting that observation of DLP-induced liposome tube by electron microscopy can be achieved. This method can effectively arrange DynA in an orderly manner. There will be no structural data processing problems in single-particle electron microscopy caused by unstable protein polymerization types.

4 Screening for novel phage resistance genes

To discover more genes related to phage resistance, we observed the response of the strains in after phage Φ29 infection on a 96-well plate through a plate reader. Therefore, we screened a single gene knockout library of *B. subtilis 168* (Koo *et al.*, 2017). Of the 960 strains screened, most of the knockout strains had growth curves similar to those of the wild type, and a few strains had growth curves similar to Δ*dynA* in response to phage infection. Δ*dagK*, Δ*ypmB*,

Δ*spo0A*, Δ*clpC,* and Δ*aroB* were selected as strains for further growth analysis to confirm the results obtained in the preliminary screening. Compared with the wild-type strain, the observed cell lysis rate of Δ*dagK*, Δ*ypmB,* and Δ*spo0A* in response to phage infection was higher based on the strong effect of phage infection on the bacterial growth curves. Therefore, Δ*dagK*, Δ*ypmB,* and Δ*spo0A* were used for further analysis. Previous studies showed that the lytic cycle of Φ29 is suppressed when cells are infected during the early stages of sporulation and the infecting genome becomes trapped into the spore. A major element of this adaptive strategy is a very sensitive response to the host-encoded Spo0A protein, the key regulator for sporulation activation, which is directly responsible for suppressing phi29 development (Castilla-Llorente *et al.*, 2009a, Castilla-Llorente *et al.*, 2009b). The emergence of Δ*spo0A* in our screening reflected the reliability of the growth curve analysis to screen phage resistance genes.

DagK encodes a diacylglycerol kinase, which is one of the key enzymes in lipid metabolism because they reintroduce diacylglycerol (DAG) formed from the hydrolysis of phospholipids into phospholipid biosynthetic pathway as well as the Lipoteichoic acid (LTA) synthesis pathway (Jerga *et al.*, 2007, Matsuoka *et al.*, 2011b, Hashimoto *et al.*, 2013). Previous studies have outlined phospholipid biosynthetic pathway and lipoteichoic acid synthesis in *B. subtilis* (**Figure 46**) and have paved the way for an understanding of their physiological roles (Salzberg & Helmann, 2008, Hashimoto *et al.*, 2013). The conversion of phosphatidic acids (PA) to DAG is catalyzed by lipid phosphate phosphohydrolases, and the reverse reaction is catalyzed by the enzyme diacylglycerol kinase (DagK). PA is also a precursor for CDP-diacylglycerol (CDP-DAG), and the conversion is mediated by phosphatidate cytidylyltransferase (CdsA). CDP-DAG is a precursor for PG, PE, and phosphatidylserine (PS). PgsA, PssA, PsD, and ClsA have been reported to be related to the synthesis of PG, PS, PE, and CL from CDP-DAG, respectively (Hashimoto *et al.*, 2013). LTA is the major cell envelope component of Gram-positive bacteria (Kiriukhin *et al.*, 2001, Neuhaus & Baddiley, 2003, Grundling & Schneewind, 2007). LTA are polymers of glycerol-1-phosphate attached to a glycosylated DAG (glycolipid anchor), diglucosyldiacylglycerol, by which it is anchored on the membrane. LTA synthesis begins with the assembly of the glycolipid anchor, and the enzyme UgtP attaches both glucose residues to DAG to form the anchor (Salzberg & Helmann, 2008). The formed glycolipid anchor moves to the outside of the membrane, likely by LtaA. The LtaS enzyme (LtaSA and YqgS) produces the polyglycerolphosphate chain by the repeated addition of glycerolphosphate residues to the tip of the growing chain using the lipid PG as substrate (Hashimoto *et al.*, 2013). The concomitantly formed DAG is recycled in the cytoplasm

to PG in reactions sequentially catalyzed by DagK, CdsA, PgsA (Kobayashi *et al.*, 2003), and as of yet unknown enzyme(s) with phosphatidylglycerol phosphate phosphatase activity.

Conditional inactivation of *dagK* led to the accumulation of diacylglycerol and the cessation of

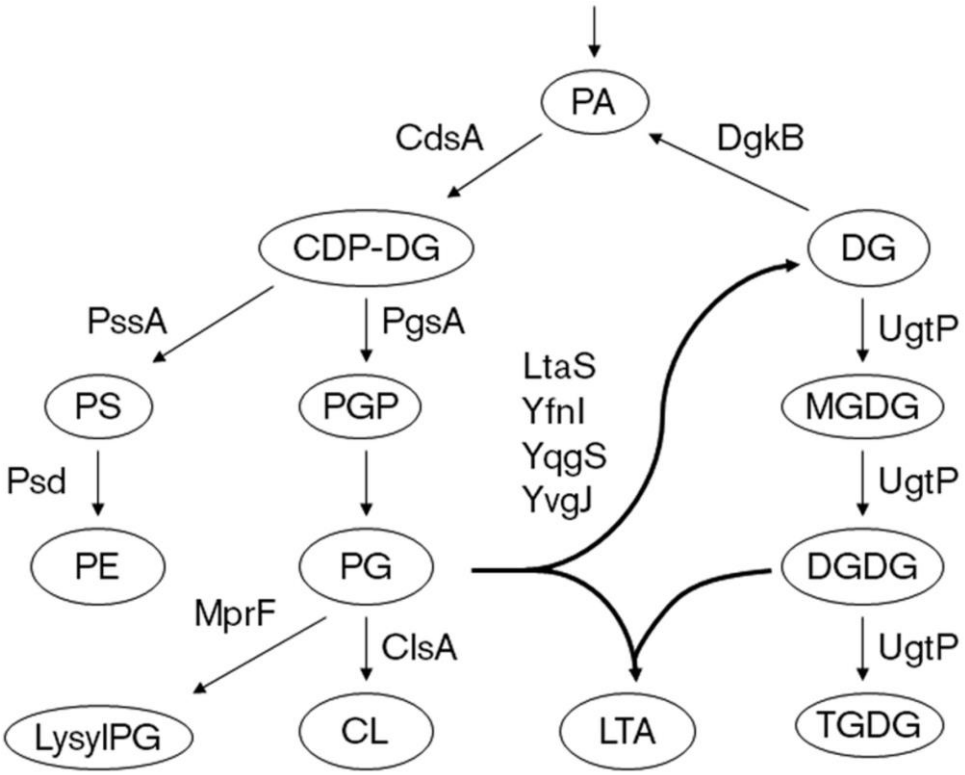

Figure 46. Biosynthetic pathways for phospholipids, glucolipids and LTA in *B. subtilis* (Hashimoto *et al.*, 2013).

lipoteichoic acid formation in *B. subtilis* (Jerga *et al.*, 2007). The difference in teichoic acid composition could lead to altered phage absorption, as the majority of phages that adsorb to Gram-Positive bacteria are via teichoic acids (Bertozzi Silva *et al.*, 2016). Additionally, modification of the LTA backbone structure can provide protection against cationic antimicrobial peptides (Percy & Grundling, 2014). Our growth curve analysis found that one of the genes with a potential role in phage resistance was *dagK*. Taking these into consideration, a series of experimental methods were used to study further the characteristics of DagK's resistance to phage infection and whether DagK helps cells resist phage infection by affecting LTA biosynthesis. In the plaque assay, Δ*dagK* had a significantly larger plaque size relative to WT, indicating that the loss of DagK eventually led to the release of more progeny phages. In the phage adsorption experiment, the average number of phages attached to each Δ*dagK* cell was three times that of WT, indicating that phages were more likely to attach to cells lacking

DagK. In the phage lysis experiment, Δ*dagK* had a higher number of plaques, which meant that phage lysed more cells after infection than WT. This indicated that the deletion of *dagK* could better lyse the host to release the phage in the first round of the phage infection cycle. In the qPCR analysis, Δ*dagK* had a higher amount of phage DNA inside and outside the cell compared to WT. A high amount of total phage DNA suggested that the replication rate of phage DNA in Δ*dagK* was higher than that of WT. This indicated that the deletion of *dagK* might accelerate the replication of progeny phage DNA or the deletion of *dagK* accelerated the attachment of phage, thereby further affecting the replication of progeny phage. The higher amount of extracellular phage DNA meant that more progeny phages of Δ*dagK* were released. This result supports the results of the lysis test, but the lack of DagK accelerated any step in the first round of the phage infection process from phage attachment to host cell lysis will lead to such results. In the prophage mitomycin C assay experiment, after the lysogenic bacteriophage SPβ was induced to lyse the cells from inside, Δ*dagK* had more plaques than WT, indicating that DagK also played a role in prophage resistance. All the above data indicate that DagK plays a role in phage resistance by hindering phage attachment, replication, and release. To further elucidate the function of DagK in phage resistance, combined with the previously reported role of DagK in lipoteichoic acid synthesis, it led to the hypothesis that DagK may play a role in phage resistance by affecting lipoteichoic acid synthesis. Based on this assumption, we first extracted the LTA and WTA of the WT and Δ*dagK* strains for comparison. We found that the LTA and WTA spectra of these two strains were not significantly different, except that after treatment with lipase, Δ*dagK* contained higher molecular weight LTA. Based on these preliminary experiments, it is difficult to draw definitive conclusions, and advanced technologies such as nuclear magnetic resonance and electrospray ionization mass spectrometry analysis may provide more insights into the differences in the LTA spectra of WT and Δ*dagK* strains. Besides, we conducted a growth curve analysis of all genes involved in the lipoteichoic acid biosynthesis pathway under phage pressure to check whether there are any other genes (*pssA, pgsA, ugtP, psD, yqgS, clsA,* and *ltaSA*) in the pathway that might affect phage resistance for the clues about the relationship between this pathway and phage resistance. However, all gene knockout strains showed normal growth curves, except that the Δ*ugtP* strain was slightly susceptible. UgtP has functioned not only in the synthesis of glucolipids and anchoring of lipoteichoic acid but also in inhibition of FtsZ assembly (Chien *et al.*, 2012, Matsuoka *et al.*, 2011a). How UgtP acts against bacteriophage need further study. In general, the absence of Dagk increased the degree of phage attachment, replication, and host cell lysis. Still, there was no evidence that DagK worked on phage resistance by affecting LTA synthesis.

The second gene found from growth curve analysis to act in phage resistance was *ypmB*, YpmB mutant has been shown to suppress the tetracycline sensitivity of an *ezrA* mutation. The transmembrane protein YpmB contains an extracytoplasmic peptidase domain, and a GFP fusion shows that the protein is enriched at cell division sites. A *ypmB* deletion causes a shorter cell length phenotype, indicating that YpmB plays a role in cell division (Gamba *et al.*, 2015). In addition, the lack of YpmB induces cell resistance to moenomycin (Zhao *et al.*, 2018). However, the physiological function of YpmB remains unknown. Here, Δ*ypmB* strains also showed a much sharper decrease in growth than WT in the growth curve analysis. It led to the idea that YpmB could have a role in phage resistance. In the plaque assay, Δ*ypmB* had a significantly larger plaque relative to WT, indicating that the loss of YpmB eventually led to the release of more progeny phages. In the phage adsorption experiment. The average number of phages attached to each Δ*ypmB* cell was less than that of WT, indicating that the absence of YpmB did not cause the cells to be more easily attached by phage. Δ*ypmB* showed no more plaques in our phage lysis experiment, which meant that phage lysed no more cells after infection than WT within 60 min. However, the lack of YpmB caused lager plagues in the plague assay. This indicates that YpmB might have no effect on the lysis of host cells in the first round of the phage infection cycle and that YpmB mediated resistance to phage infection might require longer cultivation. In the qPCR analysis, Δ*ypmB* had no higher amount of phage DNA inside and outside the cell compared to WT. This indicated that the deletion of YpmB might not affect the replication of progeny phage DNA within a 90-min infection. In the prophage mitomycin C assay, after the lysogenic bacteriophage SPβ was induced to lyse the cells inside, YpmB did not act against prophage lysis. All these data complicate the understanding of the role of YpmB in phage resistance. All the above experiments cannot help determine the role of YpmB in phage resistance in the first infection cycle. Perhaps, Ypmb acts to hinder the division of infected cells or trigger the phage resistance mechanism of surrounding cells, so the resistance of YpmB to phage infection needs a longer period of culture to show. Further analysis is needed to conclude the role of YpmB in causing resistance to phage.

References

Accola, M.A., Huang, B., Al Masri, A., and McNiven, M.A. (2002) The antiviral dynamin family member, MxA, tubulates lipids and localizes to the smooth endoplasmic reticulum. *The Journal of biological chemistry* **277**: 21829-21835.

Achtman, M., Kennedy, N., and Skurray, R. (1977) Cell--cell interactions in conjugating *Escherichia coli*: role of *traT* protein in surface exclusion. *Proceedings of the National Academy of Sciences of the United States of America* **74**: 5104-5108.

Alavi, M.V., and Fuhrmann, N. (2013) Dominant optic atrophy, OPA1, and mitochondrial quality control: understanding mitochondrial network dynamics. *Molecular neurodegeneration* **8**: 32.

Anba, J., Bidnenko, E., Hillier, A., Ehrlich, D., and Chopin, M.C. (1995) Characterization of the lactococcal *abiD1* gene coding for phage abortive infection. *Journal of bacteriology* **177**: 3818-3823.

Anderson, S.L., Carton, J.M., Lou, J., Xing, L., and Rubin, B.Y. (1999) Interferon-induced guanylate binding protein-1 (GBP-1) mediates an antiviral effect against vesicular stomatitis virus and encephalomyocarditis virus. *Virology* **256**: 8-14.

Anton, F., Dittmar, G., Langer, T., and Escobar-Henriques, M. (2013) Two deubiquitylases act on mitofusin and regulate mitochondrial fusion along independent pathways. *Molecular cell* **49**: 487-498.

Antonny, B., Burd, C., De Camilli, P., Chen, E., Daumke, O., Faelber, K., Ford, M., Frolov, V.A., Frost, A., Hinshaw, J.E., Kirchhausen, T., Kozlov, M.M., Lenz, M., Low, H.H., McMahon, H., Merrifield, C., Pollard, T.D., Robinson, P.J., Roux, A., and Schmid, S. (2016) Membrane fission by dynamin: what we know and what we need to know. *The EMBO journal* **35**: 2270-2284.

Ardail, D., Privat, J.P., Egret-Charlier, M., Levrat, C., Lerme, F., and Louisot, P. (1990) Mitochondrial contact sites. Lipid composition and dynamics. *J Biol Chem* **265**: 18797-18802.

Bair, C.L., and Black, L.W. (2007) A type IV modification dependent restriction nuclease that targets glucosylated hydroxymethyl cytosine modified DNAs. *Journal of Molecular Biology* **366**: 768-778.

Ballesteros-Plaza, D., Holguera, I., Scheffers, D.J., Salas, M., and Munoz-Espin, D. (2013) Phage 29 phi protein p1 promotes replication by associating with the FtsZ ring of the divisome in *Bacillus subtilis*. *Proceedings of the National Academy of Sciences of the United States of America* **110**: 12313-12318.

Ban, T., Heymann, J.A., Song, Z., Hinshaw, J.E., and Chan, D.C. (2010) OPA1 disease alleles causing dominant optic atrophy have defects in cardiolipin-stimulated GTP hydrolysis and membrane tubulation. *Human molecular genetics* **19**: 2113-2122.

Barrangou, R., Fremaux, C., Deveau, H., Richards, M., Boyaval, P., Moineau, S., Romero, D.A., and Horvath, P. (2007) CRISPR provides acquired resistance against viruses in prokaryotes. *Science* **315**: 1709-1712.

Bertozzi Silva, J., Storms, Z., and Sauvageau, D. (2016) Host receptors for bacteriophage adsorption. *FEMS microbiology letters* **363**.

Bhaya, D., Davison, M., and Barrangou, R. (2011) CRISPR-Cas systems in bacteria and archaea: versatile small RNAs for adaptive defense and regulation. *Annual review of genetics* **45**: 273-297.

Bidnenko, E., Ehrlich, D., and Chopin, M.C. (1995) Phage operon involved in sensitivity to the *Lactococcus lactis* abortive infection mechanism AbiD1. *Journal of bacteriology* **177**: 3824-3829.

Bidnenko, E., Ehrlich, S.D., and Chopin, M.C. (1998) *Lactococcus lactis* phage operon coding for an endonuclease homologous to RuvC. *Molecular microbiology* **28**: 823-834.

Blower, T.R., Evans, T.J., Przybilski, R., Fineran, P.C., and Salmond, G.P. (2012) Viral evasion of a bacterial suicide system by RNA-based molecular mimicry enables infectious altruism. *PLoS genetics* **8**: e1003023.

Blower, T.R., Fineran, P.C., Johnson, M.J., Toth, I.K., Humphreys, D.P., and Salmond, G.P. (2009) Mutagenesis and functional characterization of the RNA and protein components of the *toxIN* abortive infection and toxin-antitoxin locus of *Erwinia*. *Journal of bacteriology* **191**: 6029-6039.

Blower, T.R., Pei, X.Y., Short, F.L., Fineran, P.C., Humphreys, D.P., Luisi, B.F., and Salmond, G.P. (2011) A processed noncoding RNA regulates an altruistic bacterial antiviral system. *Nature structural & molecular biology* **18**: 185-190.

Bohuszewicz, O., Liu, J.W., and Low, H.H. (2016) Membrane remodelling in bacteria. *Journal of Structural Biology* **196**: 3-14.

Bondy-Denomy, J. (2018) Protein Inhibitors of CRISPR-Cas9. *ACS chemical biology* **13**: 417-423.

Bondy-Denomy, J., Pawluk, A., Maxwell, K.L., and Davidson, A.R. (2013) Bacteriophage genes that inactivate the CRISPR/Cas bacterial immune system. *Nature* **493**: 429-432.

Bowen, M.E., Weninger, K., Brunger, A.T., and Chu, S. (2004) Single molecule observation of liposome-bilayer fusion thermally induced by soluble N-ethyl maleimide sensitive-factor attachment protein receptors (SNAREs). *Biophysical Journal* **87**: 3569-3584.

Bramkamp, M. (2012) Structure and function of bacterial dynamin-like proteins. *Biological chemistry* **393**: 1203-1214.

Bramkamp, M. (2018) Bacterial dynamin-like proteins reveal mechanism for membrane fusion. *Nature communications* **9**: 3993.

Burmann, F., Ebert, N., van Baarle, S., and Bramkamp, M. (2011) A bacterial dynamin-like protein mediating nucleotide-independent membrane fusion. *Molecular microbiology* **79**: 1294-1304.

Byrnes, L.J., Singh, A., Szeto, K., Benvin, N.M., O'Donnell, J.P., Zipfel, W.R., and Sondermann, H. (2013) Structural basis for conformational switching and GTP loading of the large G protein atlastin. *The EMBO journal* **32**: 369-384.

Byrnes, L.J., and Sondermann, H. (2011) Structural basis for the nucleotide-dependent dimerization of the large G protein atlastin-1/SPG3A. *Proceedings of the National Academy of Sciences of the United States of America* **108**: 2216-2221.

Canchaya, C., Proux, C., Fournous, G., Bruttin, A., and Brussow, H. (2003) Prophage genomics. *Microbiology and molecular biology reviews : MMBR* **67**: 238-276, table of contents.

Castilla-Llorente, V., Meijer, W.J., and Salas, M. (2009a) Differential Spo0A-mediated effects on transcription and replication of the related *Bacillus subtilis* phages Nf and phi29 explain their different behaviours in vivo. *Nucleic acids research* **37**: 4955-4964.

Castilla-Llorente, V., Salas, M., and Meijer, W.J. (2009b) Different responses to Spo0A-mediated suppression of the related *Bacillus subtilis* phages Nf and phi29. *Environmental microbiology* **11**: 1137-1149.

Cerveny, K.L., McCaffery, J.M., and Jensen, R.E. (2001) Division of mitochondria requires a novel DNM1-interacting protein, Net2p. *Molecular biology of the cell* **12**: 309-321.

Chaturongakul, S., and Ounjai, P. (2014) Phage-host interplay: examples from tailed phages and Gram-negative bacterial pathogens. *Frontiers in microbiology* **5**: 442.

Chen, H., Detmer, S.A., Ewald, A.J., Griffin, E.E., Fraser, S.E., and Chan, D.C. (2003) Mitofusins Mfn1 and Mfn2 coordinately regulate mitochondrial fusion and are essential for embryonic development. *The Journal of cell biology* **160**: 189-200.

Chen, Y.J., Zhang, P., Egelman, E.H., and Hinshaw, J.E. (2004) The stalk region of dynamin drives the constriction of dynamin tubes. *Nature structural & molecular biology* **11**: 574-575.

Cheng, Y.S., Colonno, R.J., and Yin, F.H. (1983) Interferon induction of fibroblast proteins with guanylate binding activity. *The Journal of biological chemistry* **258**: 7746-7750.

Chernomordik, L.V., and Kozlov, M.M. (2003) Protein-lipid interplay in fusion and fission of biological membranes. *Annual review of biochemistry* **72**: 175-207.

Chernomordik, L.V., and Kozlov, M.M. (2005) Membrane hemifusion: crossing a chasm in two leaps. *Cell* **123**: 375-382.

Chi, R.J., Liu, J., West, M., Wang, J., Odorizzi, G., and Burd, C.G. (2014) Fission of SNX-BAR-coated endosomal retrograde transport carriers is promoted by the dynamin-related protein Vps1. *The Journal of cell biology* **204**: 793-806.

Chien, A.C., Zareh, S.K., Wang, Y.M., and Levin, P.A. (2012) Changes in the oligomerization potential of the division inhibitor UgtP co-ordinate *Bacillus subtilis* cell size with nutrient availability. *Molecular microbiology* **86**: 594-610.

Chopin, M.C., Chopin, A., and Bidnenko, E. (2005) Phage abortive infection in lactococci: variations on a theme. *Curr Opin Microbiol* **8**: 473-479.

Cipolat, S., Martins de Brito, O., Dal Zilio, B., and Scorrano, L. (2004) OPA1 requires mitofusin 1 to promote mitochondrial fusion. *Proceedings of the National Academy of Sciences of the United States of America* **101**: 15927-15932.

Colangeli, R., Helb, D., Sridharan, S., Sun, J., Varma-Basil, M., Hazbon, M.H., Harbacheuski, R., Megjugorac, N.J., Jacobs, W.R., Jr., Holzenburg, A., Sacchettini, J.C., and Alland, D. (2005) The Mycobacterium tuberculosis iniA gene is essential for activity of an efflux pump that confers drug tolerance to both isoniazid and ethambutol. *Molecular microbiology* **55**: 1829-1840.

Daste, F., Sauvanet, C., Bavdek, A., Baye, J., Pierre, F., Le Borgne, R., David, C., Rojo, M., Fuchs, P., and Tareste, D. (2018) The heptad repeat domain 1 of Mitofusin has membrane destabilization function in mitochondrial fusion. *EMBO Rep* **19**.

De Vecchis, D., Cavellini, L., Baaden, M., Henin, J., Cohen, M.M., and Taly, A. (2017) A membrane-inserted structural model of the yeast mitofusin Fzo1. *Scientific reports* **7**: 10217.

Destoumieux-Garzon, D., Duquesne, S., Peduzzi, J., Goulard, C., Desmadril, M., Letellier, L., Rebuffat, S., and Boulanger, P. (2005) The iron-siderophore transporter FhuA is the receptor for the antimicrobial peptide microcin J25: role of the microcin Val(11)-Pro(16) beta-hairpin region in the recognition mechanism. *Biochem J* **389**: 869-876.

Dy, R.L., Richter, C., Salmond, G.P., and Fineran, P.C. (2014) Remarkable Mechanisms in Microbes to Resist Phage Infections. *Annual review of virology* **1**: 307-331.

Earp, L.J., Delos, S.E., Park, H.E., and White, J.M. (2005) The many mechanisms of viral membrane fusion proteins. *Current topics in microbiology and immunology* **285**: 25-66.

Faelber, K., Posor, Y., Gao, S., Held, M., Roske, Y., Schulze, D., Haucke, V., Noe, F., and Daumke, O. (2011) Crystal structure of nucleotide-free dynamin. *Nature* **477**: 556-560.

Fineran, P.C., Blower, T.R., Foulds, I.J., Humphreys, D.P., Lilley, K.S., and Salmond, G.P. (2009) The phage abortive infection system, ToxIN, functions as a protein-RNA toxin-antitoxin pair. *Proceedings of the National Academy of Sciences of the United States of America* **106**: 894-899.

Folimonova, S.Y. (2012) Superinfection Exclusion Is an Active Virus-Controlled Function That Requires a Specific Viral Protein. *Journal of Virology* **86**: 5554-5561.

Ford, M.G., Jenni, S., and Nunnari, J. (2011) The crystal structure of dynamin. *Nature* **477**: 561-566.

Forde, A., and Fitzgerald, G.F. (2003) Molecular organization of exopolysaccharide (EPS) encoding genes on the lactococcal bacteriophage adsorption blocking plasmid, *pCI658*. *Plasmid* **49**: 130-142.

Fritz, S., Rapaport, D., Klanner, E., Neupert, W., and Westermann, B. (2001) Connection of the mitochondrial outer and inner membranes by Fzo1 is critical for organellar fusion. *The Journal of cell biology* **152**: 683-692.

Fukuda, R., McNew, J.A., Weber, T., Parlati, F., Engel, T., Nickel, W., Rothman, J.E., and Sollner, T.H. (2000) Functional architecture of an intracellular membrane t-SNARE. *Nature* **407**: 198-202.

Gamba, P., Rietkotter, E., Daniel, R.A., and Hamoen, L.W. (2015) Tetracycline hypersensitivity of an *ezrA* mutant links GalE and TseB (YpmB) to cell division. *Frontiers in microbiology* **6**: 346.

Gandre-Babbe, S., and van der Bliek, A.M. (2008) The novel tail-anchored membrane protein Mff controls mitochondrial and peroxisomal fission in mammalian cells. *Molecular biology of the cell* **19**: 2402-2412.

Gao, H., Kadirjan-Kalbach, D., Froehlich, J.E., and Osteryoung, K.W. (2003) ARC5, a cytosolic dynamin-like protein from plants, is part of the chloroplast division machinery. *Proceedings of the National Academy of Sciences of the United States of America* **100**: 4328-4333.

Goldfarb, T., Sberro, H., Weinstock, E., Cohen, O., Doron, S., Charpak-Amikam, Y., Afik, S., Ofir, G., and Sorek, R. (2015) BREX is a novel phage resistance system widespread in microbial genomes. *The EMBO journal* **34**: 169-183.

Gorsich, S.W., and Shaw, J.M. (2004) Importance of mitochondrial dynamics during meiosis and sporulation. *Molecular biology of the cell* **15**: 4369-4381.

Griffin, E.E., and Chan, D.C. (2006) Domain interactions within Fzo1 oligomers are essential for mitochondrial fusion. *The Journal of biological chemistry* **281**: 16599-16606.

Grundling, A., and Schneewind, O. (2007) Synthesis of glycerol phosphate lipoteichoic acid in *Staphylococcus aureus*. *Proceedings of the National Academy of Sciences of the United States of America* **104**: 8478-8483.

Guo, L., Xu, K., Liu, Z., Zhang, C., Xin, Y., and Zhang, Z. (2015) Assembling the *Streptococcus thermophilus* clustered regularly interspaced short palindromic repeats (CRISPR) array for multiplex DNA targeting. *Analytical biochemistry* **478**: 131-133.

Hales, K.G., and Fuller, M.T. (1997) Developmentally regulated mitochondrial fusion mediated by a conserved, novel, predicted GTPase. *Cell* **90**: 121-129.

Harner, M., and Wickner, W. (2018) Assembly of intermediates for rapid membrane fusion. *J Biol Chem* **293**: 1346-1352.

Hashimoto, M., Seki, T., Matsuoka, S., Hara, H., Asai, K., Sadaie, Y., and Matsumoto, K. (2013) Induction of extracytoplasmic function sigma factors in *Bacillus subtilis* cells with defects in lipoteichoic acid synthesis. *Microbiology* **159**: 23-35.

Hemphill, H.E., and Whiteley, H.R. (1975) Bacteriophages of *Bacillus subtilis*. *Bacteriological reviews* **39**: 257-315.

Hermann, G.J., Thatcher, J.W., Mills, J.P., Hales, K.G., Fuller, M.T., Nunnari, J., and Shaw, J.M. (1998) Mitochondrial fusion in yeast requires the transmembrane GTPase Fzo1p. *The Journal of cell biology* **143**: 359-373.

Hu, J., Shibata, Y., Zhu, P.P., Voss, C., Rismanchi, N., Prinz, W.A., Rapoport, T.A., and Blackstone, C. (2009) A class of dynamin-like GTPases involved in the generation of the tubular ER network. *Cell* **138**: 549-561.

Ishihara, N., Eura, Y., and Mihara, K. (2004) Mitofusin 1 and 2 play distinct roles in mitochondrial fusion reactions via GTPase activity. *Journal of cell science* **117**: 6535-6546.

Ishihara, N., Fujita, Y., Oka, T., and Mihara, K. (2006) Regulation of mitochondrial morphology through proteolytic cleavage of OPA1. *The EMBO journal* **25**: 2966-2977.

Ishihara, N., Nomura, M., Jofuku, A., Kato, H., Suzuki, S.O., Masuda, K., Otera, H., Nakanishi, Y., Nonaka, I., Goto, Y., Taguchi, N., Morinaga, H., Maeda, M., Takayanagi, R., Yokota, S., and Mihara, K. (2009) Mitochondrial fission factor Drp1 is essential for embryonic development and synapse formation in mice. *Nature cell biology* **11**: 958-966.

Jackson, M.B., and Chapman, E.R. (2008) The fusion pores of Ca2+-triggered exocytosis. *Nature Structural & Molecular Biology* **15**: 684-689.

Jahn, R., Lang, T., and Sudhof, T.C. (2003) Membrane fusion. *Cell* **112**: 519-533.

Janzen, C., Kochs, G., and Haller, O. (2000) A monomeric GTPase-negative MxA mutant with antiviral activity. *Journal of virology* **74**: 8202-8206.

Jerga, A., Lu, Y.J., Schujman, G.E., de Mendoza, D., and Rock, C.O. (2007) Identification of a soluble diacylglycerol kinase required for lipoteichoic acid production in *Bacillus subtilis*. *The Journal of biological chemistry* **282**: 21738-21745.

Jilly, R., Khan, N.Z., Aronsson, H., and Schneider, D. (2018) Dynamin-Like Proteins Are Potentially Involved in Membrane Dynamics within Chloroplasts and Cyanobacteria. *Frontiers in Plant Science* **9**.

Jinek, M., Chylinski, K., Fonfara, I., Hauer, M., Doudna, J.A., and Charpentier, E. (2012) A programmable dual-RNA-guided DNA endonuclease in adaptive bacterial immunity. *Science* **337**: 816-821.

Jones, B.A., and Fangman, W.L. (1992) Mitochondrial DNA maintenance in yeast requires a protein containing a region related to the GTP-binding domain of dynamin. *Genes & development* **6**: 380-389.

Kho, K., and Meredith, T.C. (2018) Salt-Induced Stress Stimulates a Lipoteichoic Acid-Specific Three-Component Glycosylation System in *Staphylococcus aureus*. *Journal of bacteriology* **200**.

Kiriukhin, M.Y., Debabov, D.V., Shinabarger, D.L., and Neuhaus, F.C. (2001) Biosynthesis of the glycolipid anchor in lipoteichoic acid of *Staphylococcus aureus* RN4220: role of YpfP, the diglucosyldiacylglycerol synthase. *Journal of bacteriology* **183**: 3506-3514.

Kobayashi, K., Ehrlich, S.D., Albertini, A., Amati, G., Andersen, K.K., Arnaud, M., Asai, K., Ashikaga, S., Aymerich, S., Bessieres, P., Boland, F., Brignell, S.C., Bron, S., Bunai, K., Chapuis, J., Christiansen, L.C., Danchin, A., Debarbouille, M., Dervyn, E., Deuerling, E., Devine, K., Devine, S.K., Dreesen, O., Errington, J., Fillinger, S., Foster, S.J., Fujita, Y., Galizzi, A., Gardan, R., Eschevins, C., Fukushima, T., Haga, K., Harwood, C.R., Hecker, M., Hosoya, D., Hullo, M.F., Kakeshita, H., Karamata, D., Kasahara, Y., Kawamura, F., Koga, K., Koski, P., Kuwana, R., Imamura, D., Ishimaru, M., Ishikawa, S., Ishio, I., Le Coq, D., Masson, A., Mauel, C., Meima, R., Mellado, R.P., Moir, A., Moriya, S., Nagakawa, E., Nanamiya, H., Nakai, S., Nygaard, P., Ogura, M., Ohanan, T., O'Reilly, M., O'Rourke, M., Pragai, Z., Pooley, H.M., Rapoport, G., Rawlins, J.P., Rivas, L.A., Rivolta, C., Sadaie, A., Sadaie, Y., Sarvas, M., Sato, T., Saxild, H.H., Scanlan, E., Schumann, W., Seegers, J.F., Sekiguchi, J., Sekowska, A., Seror, S.J., Simon, M., Stragier, P., Studer, R., Takamatsu, H., Tanaka, T., Takeuchi, M., Thomaides, H.B., Vagner, V., van Dijl, J.M., Watabe, K., Wipat, A., Yamamoto, H., Yamamoto, M., Yamamoto, Y., Yamane, K., Yata, K., Yoshida, K., Yoshikawa, H., Zuber, U., and Ogasawara, N. (2003) Essential *Bacillus subtilis* genes. *Proceedings of the National Academy of Sciences of the United States of America* **100**: 4678-4683.

Kochs, G., Haener, M., Aebi, U., and Haller, O. (2002) Self-assembly of human MxA GTPase into highly ordered dynamin-like oligomers. *The Journal of biological chemistry* **277**: 14172-14176.

Koebnik, R. (1999) Structural and functional roles of the surface-exposed loops of the beta-barrel membrane protein OmpA from *Escherichia coli*. *Journal of bacteriology* **181**: 3688-3694.

Koirala, S., Guo, Q., Kalia, R., Bui, H.T., Eckert, D.M., Frost, A., and Shaw, J.M. (2013) Interchangeable adaptors regulate mitochondrial dynamin assembly for membrane scission. *Proceedings of the National Academy of Sciences of the United States of America* **110**: E1342-1351.

Koo, B.M., Kritikos, G., Farelli, J.D., Todor, H., Tong, K., Kimsey, H., Wapinski, I., Galardini, M., Cabal, A., Peters, J.M., Hachmann, A.B., Rudner, D.Z., Allen, K.N., Typas, A., and Gross, C.A. (2017) Construction and analysis of two genome-scale deletion libraries for *Bacillus subtilis*. *Cell systems* **4**: 291-305 e297.

Koshiba, T., Detmer, S.A., Kaiser, J.T., Chen, H., McCaffery, J.M., and Chan, D.C. (2004) Structural basis of mitochondrial tethering by mitofusin complexes. *Science* **305**: 858-862.

Kuzmin, P.I., Zimmerberg, J., Chizmadzhev, Y.A., and Cohen, F.S. (2001) A quantitative model for membrane fusion based on low-energy intermediates. *Proceedings of the National Academy of Sciences of the United States of America* **98**: 7235-7240.

Kweon, D.H., Kong, B., and Shin, Y.K. (2017) Hemifusion in Synaptic Vesicle Cycle. *Front Mol Neurosci* **10**: 65.

Labrie, S.J., Samson, J.E., and Moineau, S. (2010) Bacteriophage resistance mechanisms. *Nature reviews. Microbiology* **8**: 317-327.

Lemmon, M.A. (2008) Membrane recognition by phospholipid-binding domains. *Nature Reviews Molecular Cell Biology* **9**: 99-111.

Li, Y.J., Cao, Y.L., Feng, J.X., Qi, Y., Meng, S., Yang, J.F., Zhong, Y.T., Kang, S., Chen, X., Lan, L., Luo, L., Yu, B., Chen, S., Chan, D.C., Hu, J., and Gao, S. (2019) Structural insights of human mitofusin-2 into mitochondrial fusion and CMT2A onset. *Nature communications* **10**: 4914.

Liu, J.W., Noel, J.K., and Low, H.H. (2018) Structural basis for membrane tethering by a bacterial dynamin-like pair. *Nature Communications* **9**.

Liu, M.S., Deora, R., Doulatov, S.R., Gingery, M., Eiserling, F.A., Preston, A., Maskell, D.J., Simons, R.W., Cotter, P.A., Parkhill, J., and Miller, J.F. (2002) Reverse transcriptase-mediated tropism switching in Bordetella bacteriophage. *Science* **295**: 2091-2094.

Low, H.H., and Lowe, J. (2006) A bacterial dynamin-like protein. *Nature* **444**: 766-769.

Low, H.H., Sachse, C., Amos, L.A., and Lowe, J. (2009) Structure of a bacterial dynamin-like protein lipid tube provides a mechanism for assembly and membrane curving. *Cell* **139**: 1342-1352.

Lu, M.J., and Henning, U. (1994) Superinfection exclusion by T-even-type coliphages. *Trends in microbiology* **2**: 137-139.

Mahony, J., McGrath, S., Fitzgerald, G.F., and van Sinderen, D. (2008) Identification and characterization of lactococcal-prophage-carried superinfection exclusion genes. *Appl Environ Microb* **74**: 6206-6215.

Marrink, S.J., and Mark, A.E. (2004) Molecular view of hexagonal phase formation in phospholipid membranes. *Biophysical journal* **87**: 3894-3900.

Matsuoka, S., Chiba, M., Tanimura, Y., Hashimoto, M., Hara, H., and Matsumoto, K. (2011a) Abnormal morphology of *Bacillus subtilis ugtP* mutant cells lacking glucolipids. *Genes & genetic systems* **86**: 295-304.

Matsuoka, S., Hashimoto, M., Kamiya, Y., Miyazawa, T., Ishikawa, K., Hara, H., and Matsumoto, K. (2011b) The *Bacillus subtilis* essential gene *dgkB* is dispensable in mutants with defective lipoteichoic acid synthesis. *Genes & genetic systems* **86**: 365-376.

Mears, J.A., Lackner, L.L., Fang, S., Ingerman, E., Nunnari, J., and Hinshaw, J.E. (2011) Conformational changes in Dnm1 support a contractile mechanism for mitochondrial fission. *Nature structural & molecular biology* **18**: 20-26.

Mears, J.A., Ray, P., and Hinshaw, J.E. (2007) A corkscrew model for dynamin constriction. *Structure* **15**: 1190-1202.

Melen, K., Ronni, T., Broni, B., Krug, R.M., von Bonsdorff, C.H., and Julkunen, I. (1992) Interferon-induced Mx proteins form oligomers and contain a putative leucine zipper. *The Journal of biological chemistry* **267**: 25898-25907.

Menouni, R., Hutinet, G., Petit, M.A., and Ansaldi, M. (2015) Bacterial genome remodeling through bacteriophage recombination. *FEMS microbiology letters* **362**: 1-10.

Meyer, J.R., Dobias, D.T., Weitz, J.S., Barrick, J.E., Quick, R.T., and Lenski, R.E. (2012) Repeatability and contingency in the evolution of a key innovation in phage lambda. *Science* **335**: 428-432.

Michie, K.A., Boysen, A., Low, H.H., Moller-Jensen, J., and Lowe, J. (2014) LeoA, B and C from enterotoxigenic *Escherichia coli* (ETEC) are bacterial dynamins. *PloS one* **9**: e107211.

Mima, J., Hickey, C.M., Xu, H., Jun, Y., and Wickner, W. (2008) Reconstituted membrane fusion requires regulatory lipids, SNAREs and synergistic SNARE chaperones. *EMBO J* **27**: 2031-2042.

Miyagishima, S.Y., Nishida, K., Mori, T., Matsuzaki, M., Higashiyama, T., Kuroiwa, H., and Kuroiwa, T. (2003) A plant-specific dynamin-related protein forms a ring at the chloroplast division site. *The Plant cell* **15**: 655-665.

Molineux, I.J. (1991) Host-Parasite Interactions - Recent Developments in the Genetics of Abortive Phage Infections. *New Biol* **3**: 230-236.

Mozdy, A.D., McCaffery, J.M., and Shaw, J.M. (2000) Dnm1p GTPase-mediated mitochondrial fission is a multi-step process requiring the novel integral membrane component Fis1p. *The Journal of cell biology* **151**: 367-380.

Namekawa, M., Muriel, M.P., Janer, A., Latouche, M., Dauphin, A., Debeir, T., Martin, E., Duyckaerts, C., Prigent, A., Depienne, C., Sittler, A., Brice, A., and Ruberg, M. (2007) Mutations in the SPG3A gene encoding the GTPase atlastin interfere with vesicle trafficking in the ER/Golgi interface and Golgi morphogenesis. *Molecular and cellular neurosciences* **35**: 1-13.

Neuhaus, F.C., and Baddiley, J. (2003) A continuum of anionic charge: structures and functions of D-alanyl-teichoic acids in gram-positive bacteria. *Microbiology and molecular biology reviews : MMBR* **67**: 686-723.

Ngo, C.C., and Man, S.M. (2017) Mechanisms and functions of guanylate-binding proteins and related interferon-inducible GTPases: Roles in intracellular lysis of pathogens. *Cellular microbiology* **19**.

Nordstrom, K., and Forsgren, A. (1974) Effect of protein A on adsorption of bacteriophages to Staphylococcus aureus. *J Virol* **14**: 198-202.

O'Sullivan, D., Twomey, D.P., Coffey, A., Hill, C., Fitzgerald, G.F., and Ross, R.P. (2000) Novel type I restriction specificities through domain shuffling of HsdS subunits in *Lactococcus lactis*. *Molecular microbiology* **36**: 866-875.

Olichon, A., Emorine, L.J., Descoins, E., Pelloquin, L., Brichese, L., Gas, N., Guillou, E., Delettre, C., Valette, A., Hamel, C.P., Ducommun, B., Lenaers, G., and Belenguer, P. (2002) The human dynamin-related protein OPA1 is anchored to the mitochondrial inner membrane facing the inter-membrane space. *FEBS letters* **523**: 171-176.

Olovnikov, I., Chan, K., Sachidanandam, R., Newman, D.K., and Aravin, A.A. (2013) Bacterial argonaute samples the transcriptome to identify foreign DNA. *Molecular cell* **51**: 594-605.

Opdenkamp, J.A., Redai, I., and Vandeene.Ll (1969) Phospholipid composition of *Bacillus subtilis*. *Journal of Bacteriology* **99**: 298-303.

Orso, G., Pendin, D., Liu, S., Tosetto, J., Moss, T.J., Faust, J.E., Micaroni, M., Egorova, A., Martinuzzi, A., McNew, J.A., and Daga, A. (2009) Homotypic fusion of ER membranes requires the dynamin-like GTPase atlastin. *Nature* **460**: 978-983.

Otera, H., Wang, C., Cleland, M.M., Setoguchi, K., Yokota, S., Youle, R.J., and Mihara, K. (2010) Mff is an essential factor for mitochondrial recruitment of Drp1 during mitochondrial fission in mammalian cells. *The Journal of cell biology* **191**: 1141-1158.

Palmer, C.S., Osellame, L.D., Laine, D., Koutsopoulos, O.S., Frazier, A.E., and Ryan, M.T. (2011) MiD49 and MiD51, new components of the mitochondrial fission machinery. *EMBO reports* **12**: 565-573.

Parone, P.A., Da Cruz, S., Tondera, D., Mattenberger, Y., James, D.I., Maechler, P., Barja, F., and Martinou, J.C. (2008) Preventing mitochondrial fission impairs mitochondrial function and leads to loss of mitochondrial DNA. *PloS one* **3**: e3257.

Percy, M.G., and Grundling, A. (2014) Lipoteichoic acid synthesis and function in gram-positive bacteria. *Annual review of microbiology* **68**: 81-100.

Praefcke, G.J., and McMahon, H.T. (2004) The dynamin superfamily: universal membrane tubulation and fission molecules? *Nature reviews. Molecular cell biology* **5**: 133-147.

Prakash, B., Praefcke, G.J., Renault, L., Wittinghofer, A., and Herrmann, C. (2000a) Structure of human guanylate-binding protein 1 representing a unique class of GTP-binding proteins. *Nature* **403**: 567-571.

Prakash, B., Renault, L., Praefcke, G.J., Herrmann, C., and Wittinghofer, A. (2000b) Triphosphate structure of guanylate-binding protein 1 and implications for nucleotide binding and GTPase mechanism. *The EMBO journal* **19**: 4555-4564.

Prince, A., Sandhu, P., Ror, P., Dash, E., Sharma, S., Arakha, M., Jha, S., Akhter, Y., and Saleem, M. (2016) Lipid-II Independent Antimicrobial Mechanism of Nisin Depends On Its Crowding And Degree Of Oligomerization. *Scientific reports* **6**: 37908.

Ram, G., Chen, J., Kumar, K., Ross, H.F., Ubeda, C., Damle, P.K., Lane, K.D., Penades, J.R., Christie, G.E., and Novick, R.P. (2012) Staphylococcal pathogenicity island interference with helper phage reproduction is a paradigm of molecular parasitism. *Proceedings of the National Academy of Sciences of the United States of America* **109**: 16300-16305.

Rambold, A.S., Kostelecky, B., Elia, N., and Lippincott-Schwartz, J. (2011) Tubular network formation protects mitochondria from autophagosomal degradation during nutrient starvation. *Proceedings of the National Academy of Sciences of the United States of America* **108**: 10190-10195.

Rapaport, D., Brunner, M., Neupert, W., and Westermann, B. (1998) Fzo1p is a mitochondrial outer membrane protein essential for the biogenesis of functional mitochondria in *Saccharomyces cerevisiae*. *The Journal of biological chemistry* **273**: 20150-20155.

Raven, P.H., (2011) *Biology,* 1279, 1297 p. McGraw-Hill, Dubuque, IA.

Reubold, T.F., Faelber, K., Plattner, N., Posor, Y., Ketel, K., Curth, U., Schlegel, J., Anand, R., Manstein, D.J., Noe, F., Haucke, V., Daumke, O., and Eschenburg, S. (2015) Crystal structure of the dynamin tetramer. *Nature* **525**: 404-408.

Richter, C., Chang, J.T., and Fineran, P.C. (2012) Function and regulation of clustered regularly interspaced short palindromic repeats (CRISPR) / CRISPR associated (Cas) systems. *Viruses* **4**: 2291-2311.

Riede, I., and Eschbach, M.L. (1986) Evidence That Trat Interacts with Ompa of Escherichia-Coli. *Febs Lett* **205**: 241-245.

Rismanchi, N., Soderblom, C., Stadler, J., Zhu, P.P., and Blackstone, C. (2008) Atlastin GTPases are required for Golgi apparatus and ER morphogenesis. *Human molecular genetics* **17**: 1591-1604.

Risselada, H.J., Bubnis, G., and Grubmuller, H. (2014) Expansion of the fusion stalk and its implication for biological membrane fusion. *Proceedings of the National Academy of Sciences of the United States of America* **111**: 11043-11048.

Rosch, T.C., Oviedo-Bocanegra, L.M., Fritz, G., and Graumann, P.L. (2018) SMTracker: a tool for quantitative analysis, exploration and visualization of single-molecule tracking data reveals highly dynamic binding of B-subtilis global repressor AbrB throughout the genome. *Sci Rep-Uk* **8**.

Rothman, J.H., Raymond, C.K., Gilbert, T., O'Hara, P.J., and Stevens, T.H. (1990) A putative GTP binding protein homologous to interferon-inducible Mx proteins performs an essential function in yeast protein sorting. *Cell* **61**: 1063-1074.

Südhof, T.C., and Rothman, J.E. (2009) Membrane fusion: grappling with SNARE and SM proteins. *Science (New York, N.Y.)* **323**: 474-477.

Salzberg, L.I., and Helmann, J.D. (2008) Phenotypic and transcriptomic characterization of *Bacillus subtilis* mutants with grossly altered membrane composition. *Journal of bacteriology* **190**: 7797-7807.

Samson, J.E., Magadan, A.H., Sabri, M., and Moineau, S. (2013) Revenge of the phages: defeating bacterial defences. *Nature Reviews Microbiology* **11**: 675-687.

Sandre, O., Moreaux, L., and Brochard-Wyart, F. (1999) Dynamics of transient pores in stretched vesicles. *Proceedings of the National Academy of Sciences of the United States of America* **96**: 10591-10596.

Santel, A., Frank, S., Gaume, B., Herrler, M., Youle, R.J., and Fuller, M.T. (2003) Mitofusin-1 protein is a generally expressed mediator of mitochondrial fusion in mammalian cells. *Journal of cell science* **116**: 2763-2774.

Santel, A., and Fuller, M.T. (2001) Control of mitochondrial morphology by a human mitofusin. *Journal of cell science* **114**: 867-874.

Sapranauskas, R., Gasiunas, G., Fremaux, C., Barrangou, R., Horvath, P., and Siksnys, V. (2011) The Streptococcus thermophilus CRISPR/Cas system provides immunity in Escherichia coli. *Nucleic acids research* **39**: 9275-9282.

Satoh, M., Hamamoto, T., Seo, N., Kagawa, Y., and Endo, H. (2003) Differential sublocalization of the dynamin-related protein OPA1 isoforms in mitochondria. *Biochemical and biophysical research communications* **300**: 482-493.

Sawant, P., (2015) Functional characterisation and Mutational analysis of a bacterial dynamin-like protein, DynA. In: Faculty of Biology. Ludwig-Maximilians Universität München. Elektronische Dissertation, DOI: 10.5282/edoc.18394.

Sawant, P., Eissenberger, K., Karier, L., Mascher, T., and Bramkamp, M. (2016) A dynamin-like protein involved in bacterial cell membrane surveillance under environmental stress. *Environmental microbiology* **18**: 2705-2720.

Schlimpert, S., Wasserstrom, S., Chandra, G., Bibb, M.J., Findlay, K.C., Flardh, K., and Buttner, M.J. (2017) Two dynamin-like proteins stabilize FtsZ rings during Streptomyces sporulation. *Proceedings of the National Academy of Sciences of the United States of America* **114**: E6176-E6183.

Schrepfer, E., and Scorrano, L. (2016) Mitofusins, from Mitochondria to Metabolism. *Molecular cell* **61**: 683-694.

Schuster, C.F., and Bertram, R. (2013) Toxin-antitoxin systems are ubiquitous and versatile modulators of prokaryotic cell fate. *FEMS microbiology letters* **340**: 73-85.

Schwemmle, M., and Staeheli, P. (1994) The interferon-induced 67-kDa guanylate-binding protein (hGBP1) is a GTPase that converts GTP to GMP. *The Journal of biological chemistry* **269**: 11299-11305.

Scorrano, L. (2013) Keeping mitochondria in shape: a matter of life and death. *European journal of clinical investigation* **43**: 886-893.

Seed, K.D. (2015) Battling Phages: How Bacteria Defend against Viral Attack. *PLoS pathogens* **11**: e1004847.

Shepard, K.A., and Yaffe, M.P. (1999) The yeast dynamin-like protein, Mgm1p, functions on the mitochondrial outer membrane to mediate mitochondrial inheritance. *The Journal of cell biology* **144**: 711-720.

Shpetner, H.S., and Vallee, R.B. (1989) Identification of dynamin, a novel mechanochemical enzyme that mediates interactions between microtubules. *Cell* **59**: 421-432.

Smirnova, E., Shurland, D.L., Ryazantsev, S.N., and van der Bliek, A.M. (1998) A human dynamin-related protein controls the distribution of mitochondria. *The Journal of cell biology* **143**: 351-358.

Song, H., Orr, A., Duan, M., Merz, A.J., and Wickner, W. (2017) Sec17/Sec18 act twice, enhancing membrane fusion and then disassembling cis-SNARE complexes. *Elife* **6**.

Song, Z., Chen, H., Fiket, M., Alexander, C., and Chan, D.C. (2007) OPA1 processing controls mitochondrial fusion and is regulated by mRNA splicing, membrane potential, and Yme1L. *The Journal of cell biology* **178**: 749-755.

Sorek, R., Kunin, V., and Hugenholtz, P. (2008) CRISPR - a widespread system that provides acquired resistance against phages in bacteria and archaea. *Nature Reviews Microbiology* **6**: 181-186.

Staeheli, P., Haller, O., Boll, W., Lindenmann, J., and Weissmann, C. (1986) Mx protein: constitutive expression in 3T3 cells transformed with cloned Mx cDNA confers selective resistance to influenza virus. *Cell* **44**: 147-158.

Stibitz, S., Aaronson, W., Monack, D., and Falkow, S. (1989) Phase variation in *Bordetella pertussis* by frameshift mutation in a gene for a novel two-component system. *Nature* **338**: 266-269.

Sutherland, I.W. (1995) Polysaccharide Lyases. *Fems Microbiol Rev* **16**: 323-347.

Sutherland, I.W., Hughes, K.A., Skillman, L.C., and Tait, K. (2004) The interaction of phage and biofilms. *Fems Microbiol Lett* **232**: 1-6.

Taguchi, N., Ishihara, N., Jofuku, A., Oka, T., and Mihara, K. (2007) Mitotic phosphorylation of dynamin-related GTPase Drp1 participates in mitochondrial fission. *The Journal of biological chemistry* **282**: 11521-11529.

Tieu, Q., and Nunnari, J. (2000) Mdv1p is a WD repeat protein that interacts with the dynamin-related GTPase, Dnm1p, to trigger mitochondrial division. *The Journal of cell biology* **151**: 353-366.

Tock, M.R., and Dryden, D.T. (2005a) The biology of restriction and anti-restriction. *Current opinion in microbiology* **8**: 466-472.

Tock, M.R., and Dryden, D.T.F. (2005b) The biology of restriction and anti-restriction. *Curr Opin Microbiol* **8**: 466-472.

Tondera, D., Grandemange, S., Jourdain, A., Karbowski, M., Mattenberger, Y., Herzig, S., Da Cruz, S., Clerc, P., Raschke, I., Merkwirth, C., Ehses, S., Krause, F., Chan, D.C., Alexander, C., Bauer, C., Youle, R., Langer, T., and Martinou, J.C. (2009) SLP-2 is required for stress-induced mitochondrial hyperfusion. *The EMBO journal* **28**: 1589-1600.

Uhl, M.A., and Miller, J.F. (1996) Integration of multiple domains in a two-component sensor protein: the Bordetella pertussis BvgAS phosphorelay. *EMBO J* **15**: 1028-1036.

Ungermann, C., Nichols, B.J., Pelham, H.R., and Wickner, W. (1998) A vacuolar v-t-SNARE complex, the predominant form in vivo and on isolated vacuoles, is disassembled and activated for docking and fusion. *J Cell Biol* **140**: 61-69.

Verhelst, J., Hulpiau, P., and Saelens, X. (2013) Mx proteins: antiviral gatekeepers that restrain the uninvited. *Microbiology and molecular biology reviews : MMBR* **77**: 551-566.

Wakabayashi, J., Zhang, Z., Wakabayashi, N., Tamura, Y., Fukaya, M., Kensler, T.W., Iijima, M., and Sesaki, H. (2009) The dynamin-related GTPase Drp1 is required for embryonic and brain development in mice. *The Journal of cell biology* **186**: 805-816.

Wang, M., Guo, X., Yang, X., Zhang, B., Ren, J., Liu, A., Ran, Y., Yan, B., Chen, F., Guddat, L.W., Hu, J., Li, J., and Rao, Z. (2019) Mycobacterial dynamin-like protein IniA mediates membrane fission. *Nature communications* **10**: 3906.

Warner, F.D., Kitos, G.A., Romano, M.P., and Hemphill, H.E. (1977) Characterization of SPβ: a temperate bacteriophage from *Bacillus subtilis 168M*. *Canadian Journal of Microbiology* **23**: 45-51.

Weber, T., Zemelman, B.V., McNew, J.A., Westermann, B., Gmachl, M., Parlati, F., Sollner, T.H., and Rothman, J.E. (1998) SNAREpins: minimal machinery for membrane fusion. *Cell* **92**: 759-772.

Westra, E.R., Swarts, D.C., Staals, R.H., Jore, M.M., Brouns, S.J., and van der Oost, J. (2012) The CRISPRs, they are a-changin': how prokaryotes generate adaptive immunity. *Annual review of genetics* **46**: 311-339.

Wiedenheft, B., Sternberg, S.H., and Doudna, J.A. (2012) RNA-guided genetic silencing systems in bacteria and archaea. *Nature* **482**: 331-338.

Willey, J.M., Sherwood, L., Woolverton, C.J., and Prescott, L.M., (2008) *Prescott, Harley, and Klein's microbiology,* 1088, 1107 p. McGraw-Hill Higher Education, New York.

Wilsbach, K., and Payne, G.S. (1993) Vps1p, a member of the dynamin GTPase family, is necessary for Golgi membrane protein retention in *Saccharomyces cerevisiae*. *The EMBO journal* **12**: 3049-3059.

Wong, E.D., Wagner, J.A., Scott, S.V., Okreglak, V., Holewinske, T.J., Cassidy-Stone, A., and Nunnari, J. (2003) The intramitochondrial dynamin-related GTPase, Mgm1p, is a component of a protein complex that mediates mitochondrial fusion. *The Journal of cell biology* **160**: 303-311.

Wu, Z., Thiyagarajan, S., O'Shaughnessy, B., and Karatekin, E. (2017) Regulation of Exocytotic Fusion Pores by SNARE Protein Transmembrane Domains. *Front Mol Neurosci* **10**: 315.

Xiang, Y., Morais, M.C., Battisti, A.J., Grimes, S., Jardine, P.J., Anderson, D.L., and Rossmann, M.G. (2006) Structural changes of bacteriophage phi29 upon DNA packaging and release. *The EMBO journal* **25**: 5229-5239.

Xu, K., Ren, C., Liu, Z., Zhang, T., Zhang, T., Li, D., Wang, L., Yan, Q., Guo, L., Shen, J., and Zhang, Z. (2015) Efficient genome engineering in eukaryotes using Cas9 from *Streptococcus thermophilus*. *Cellular and molecular life sciences : CMLS* **72**: 383-399.

Yu, J.J.Q., Wu, T.L., Liszewski, M.K., Dai, J.H., Swiggard, W.J., Baytop, C., Frank, I., Levine, B.L., Yang, W., Theodosopoulos, T., and O'Doherty, U. (2008) A more precise HIV integration assay designed to detect small differences finds lower levels of integrated DNA in HAART treated patients. *Virology* **379**: 78-86.

Zahler, S.A., Korman, R.Z., Rosenthal, R., and Hemphill, H.E. (1977) *Bacillus subtilis* bacteriophage SPbeta: localization of the prophage attachment site, and specialized transduction. *Journal of bacteriology* **129**: 556-558.

Zhang, P., and Hinshaw, J.E. (2001) Three-dimensional reconstruction of dynamin in the constricted state. *Nature cell biology* **3**: 922-926.

Zhao, H., Roistacher, D.M., and Helmann, J.D. (2018) Aspartate deficiency limits peptidoglycan synthesis and sensitizes cells to antibiotics targeting cell wall synthesis in *Bacillus subtilis*. *Molecular microbiology* **109**: 826-844.

Zhao, J., Liu, T., Jin, S., Wang, X., Qu, M., Uhlen, P., Tomilin, N., Shupliakov, O., Lendahl, U., and Nister, M. (2011) Human MIEF1 recruits Drp1 to mitochondrial outer membranes and promotes mitochondrial fusion rather than fission. *The EMBO journal* **30**: 2762-2778.

Zhao, X., Alvarado, D., Rainier, S., Lemons, R., Hedera, P., Weber, C.H., Tukel, T., Apak, M., Heiman-Patterson, T., Ming, L., Bui, M., and Fink, J.K. (2001) Mutations in a newly identified GTPase gene cause autosomal dominant hereditary spastic paraplegia. *Nature genetics* **29**: 326-331.

Zheng, L., Baumann, U., and Reymond, J.L. (2004) An efficient one-step site-directed and site-saturation mutagenesis protocol. *Nucleic acids research* **32**: e115.

Zhu, P.P., Patterson, A., Lavoie, B., Stadler, J., Shoeb, M., Patel, R., and Blackstone, C. (2003) Cellular localization, oligomerization, and membrane association of the hereditary spastic paraplegia 3A (SPG3A) protein atlastin. *The Journal of biological chemistry* **278**: 49063-49071.

Zick, M., and Wickner, W.T. (2014) A distinct tethering step is vital for vacuole membrane fusion. *eLife* **3**: e03251.

Zucchi, P.C., and Zick, M. (2011) Membrane fusion catalyzed by a Rab, SNAREs, and SNARE chaperones is accompanied by enhanced permeability to small molecules and by lysis. *Molecular Biology of the Cell* **22**: 4635-4646.

Abbreviations

Abi	Abortive infection systems
ARC5	Accumulation and replication of chloroplasts protein 5
BCA	Bicinchoninic acid
BCIP	5-Bromo-4-chloro-3- indolyl phosphate
BDLP	Bacterial dynamin-like protein
BDLPs	Bacterial DLPs
BSE	Bundle signaling element
CAA	Casamino acids
Cas	CRISPR associated proteins
CDP-DAG	CDP-diacylglycerol
CdsA	Cytidylyltransferase
CRISPR	Clustered Regularly Interspaced Short Palindromic Repeats
crRNAs	CRISPR RNAs
CL	Cardiolipin
CTF	Contrast transfer function
Cy5	Cyanine 5
DAG	Diacylglycerol
DLP	Dynamin-like protein
DNA	Deoxyribonucleic acid
CRISPR	Clustered regularly interspaced short palindromic repeats
DRP1	Dynamin-related protein 1
DynA++	DynA-overexpressed
DagK	Diacylglycerol kinase
EPSs	Exopolysaccharides

FRET	Fluorescence resonance energy transfer
Fis1	Fission protein 1
FtsZ	Filament temperature-sensitive protein Z
Fzo1	Fuzzy onions 1
gDNA	Genomic DNA
GED	GTPase effector domain
GBP1	Guanylate-binding protein 1
GBPs	Guanylate-binding proteins
GDP	Guanosine diphosphate
gRNA	Guiding RNA
GTP	Guanosine triphosphate
HEPES	4-(2-hydroxyethyl)-1-piperazineethanesulfonic acid
HPLC	High-performance liquid chromatography
IniA	Isoniazid-induced protein A
LTA	Lipoteichoic acid
MB	Marina Blue
MccJ25	Microcin J25
Mdv1	Mitochondrial division protein 1
Mff	Mitochondrial fission factor
Mfn1	Mitofusin 1
Mfn2	Mitofusin 2
Mgm1	Mitochondrial genome maintenance protein 1
MiD49	Mitochondrial dynamics proteins 49
MiD51	Mitochondrial dynamics proteins 51
MTases	Methyltransferases

NBD	7-Nitrobenz-2-Oxa-1,3-Diazol-4-yl
NBT	Nitro blue tetrazolium
NosDLP	*Nostoc punctiforme* dynamin-like protein
OPA1	Optic atrophy protein 1
PA	Phosphatidic acids
PALM	Photo-activated localization microscopy
PCR	Polymerase chain reaction
PE	Phosphatidylethanolamine
PG	Phosphatidylglycerol
PH	Pleckstrin homology
PRD	Proline/arginine rich domain
PS	Phosphatidylserine
RNA	Ribonucleic acid
R-phycoE	R-phycoerythrin
RM	Restriction-Modification
REases	Restriction endonucleases
Sa-Cy5	Streptavidin-Cy5
SaPIs	Staphylococcal pathogenicity islands
SDM	Site-directed mutagenesis
SDS-PAGE	Polyacrylamide gel electrophoresis
SGD	Stochastic Gradient Descent
SNAREs	Soluble N-ethyl maleimide sensitive factor attachment protein receptors
TA	Toxin–antitoxin
TEM	Transmission electron microscope
Tris	Tris(hydroxymethyl)aminomethane

UAc	Uranyl acetate
Vps1	Vacuolar protein sorting-associated protein 1
wt/vol	weight/volume% (g/ml%)
wt/wt	weight/weight
WTA	Wall teichoic acids

Acknowledgements

I am very grateful to Prof. Dr. Marc Bramkamp, who not only gave me support and guidance in my doctoral research work, but also gave me spiritual encouragement, trust, and tolerance. I also sincerely thank the China Scholarship Council for sponsoring my living expenses to research with peace of mind. I am grateful for the help of my colleague Giacomo Giacomelli and Helge Feddersen for fluorescence microscopy and usage of ImageJ, and Dr. Karin Schubert for HPLC. I would also like to thank Prof. Dr. Peter Graumann and Laura Sattler at Philipps University of Marburg for their work on DynA dynamics and publishing a paper with us on the mechanism of DynA resistance to phage. Besides, I am grateful for the help of Prof. Dr. Christine Ziegler, Dr. Gregor Madej, and Lifei Fu at University of Regensburg for the electron microscopy of apo-DynA particles. I also supervised two promising students, Gabriela Stumberger and Nupur Sharma, with them to research membrane fusion analysis of YpbS and screening of other phage-resistant proteins of *B. subtilis*.

I have a lot of precious memories with my colleagues (Dr. Kati Böhm, Dr. Gustavo Benevides, Dr. Karin Schubert, Helge Feddersen, Giacomo Giacomelli, Abigail Savietto, Fabian Meyer, and Nadine Albrecht), hiking in the forest and lakeside, cooking together, learning winemaking, drinking at Christmas markets, Oktoberfest, our kitchen and restaurants, which creates a lot of joy and releases a lot of stress. Of course, they gave a lot of help and suggestions during the research process. I am honored to be part of this group.

Finally, I would also like to thank my family and friends, especially Yizhao Jia, for giving me the courage to face difficulties when I encounter bottlenecks in my life and research.

This time as a Ph.D. student is crucial in my life. I will always appreciate and remember this time and those who have supported me.